Fall 1997

Electrocatalytic control of exhaust soot

Victor L. Callahan
New Jersey Institute of Technology

ABSTRACT

ELECTROCATALYTIC CONTROL OF EXHAUST SOOT

by
Victor L. Callahan

The feasibility of combining electrostatic precipitation and use of a catalytic wall in a straight tube reactor as a means of destroying soot particles was investigated. Enhanced particle diffusion to the wall by an applied electric field provided the means of particle capture for subsequent catalytic oxidation at the active surface in a small length tube.

Soot particles flowing in a gas stream are influenced by the following transport mechanisms: convective flux as a result of bulk flow, diffusion flux as a result of particle concentration or number density gradient, and an electrostatic flux from the coulombic attraction as charged particles move to an electrically grounded wall. When an external electric field is applied, the resulting electrostatic flux dominates the particle transport mechanism. Soot capture on a catalyst wall is by adsorption onto a catalytically active site. With sufficient oxygen present and surface temperatures near 400 °C, catalytic oxidation of soot is evident by heat released due to exothermic reactions, and increased CO and CO_2 (CO_x) concentrations.

The experimental results indicated increased catalytic activity under light sooting conditions by raising the applied voltage in stepwise increments. A voltage of -2.5 kV was found to yield the maximum CO_x levels and highest catalytic surface temperatures (30-60 °C). Increased oxygen concentration (> 0.40 mole fraction) was the most important factor in promoting soot oxidation. Heavy sooting conditions, or a high voltage quickly applied caused rapid accumulation of particle deposition on the surface resulting in

fouling the catalyst and decreasing the catalytic activity. The particle size fraction of soot flowing into the catalytic reactor from the combustor indicated a bimodal distribution. The largest peak occurred at 1.4 μm, while a smaller peak was found at 3.0 μm.

A mathematical model to simulate electrostatic precipitation was developed to incorporate the use of a distribution of particle size fractions. The predicted penetration from modeling was compared with experimental results of reactor outlet soot loadings for increased voltage. Under light sooting conditions, model predictions agreed well with the trends exhibited by the experimental data for a particle satuation charge level of 35%. Additionally, the mathematical model was able to predict particle penetration along the axial tube length. The modeling was found to be in good agreement with the experimental results.

ELECTROCATALYTIC CONTROL OF EXHAUST SOOT

by
Victor L. Callahan

A Dissertation
Submitted to the Faculty of
New Jersey Institute of Technology
in Partial Fulfillment of the Requirements for the Degree of
Doctor of Philosophy

Department of Mechanical Engineering

October 1997

APPROVAL PAGE

ELECTROCATALYTIC CONTROL OF EXHAUST SOOT

Victor L. Callahan

Dr. Robert B. Barat, Dissertation Advisor — Date
Associate Professor of Chemical Engineering, NJIT

Associate Professor of Mechanical Engineering, NJIT — Date

Dr. Bernard Koplik, Committee Member — Date
Professor of Mechanical Engineering, NJIT

Dr. John Droughton, Committee Member — Date
Professor of Mechanical Engineering, NJIT

Dr. John Stevens, Committee Member — Date
Professor of Mathematics, Montclair State University

BIOGRAPHICAL SKETCH

Author: Victor L. Callahan

Degree: Doctor of Philosophy in Mechanical Engineering

Date: October 1997

Undergraduate and Graduate Education:

- Doctor of Philosophy in Mechanical Engineering
  New Jersey Institute of Technology, Newark, NJ, 1997
- Master of Science in Chemical Engineering
  New Jersey Institute of Technology, Newark, NJ, 1996
- Master of Science in Mechanical Engineering
  Brigham Young University, Provo, UT, 1992
- Bachelor of Science in Industrial Engineering
  Cal Poly State University, San Luis Obsispo, CA, 1981

Major: Mechanical Engineering

Presentations and Publications

Priedeman, D., Callahan, V., and Webb, B., "Enhancement of Liquid Jet Impingement Heat Transfer with Surface Modifications." *Journal of Heat Transfer*, Transactions ASME, Vol. 116, No. 2 (1994): 486-489.

This dissertation is dedicated to my loving wife Wendy
whose longstanding support made this all possible.
Included in this dedication are my children,
Grant Edward, Aubrey Marie, and Jamie Ashlyn.

ACKNOWLEDGMENT

The author wishes to express his sincere gratitude and appreciation to his dissertation advisor, Professor Robert B. Barat for his outstanding guidance and support throughout this study. Dr. Barat's dedication and encouragement were most instrumental in the successful conclusion of this research.

The author is also grateful to Professor John Stevens whose enthusiasm and knowledge made possible the computer simulation models.

Special thanks to Professor Pasquale Florio for serving as committee chairman, and Professors Bernard Koplik and John Droughton for serving as members of the committee.

The author wishes to thank the staff at the Hazardous Substance Management Research Center for both financial and technical assistance.

Lastly, the author wishes to acknowledge the late Dr. Anthony Cerkanowicz as the originator and driving force for starting this research effort.

TABLE OF CONTENTS

TABLE OF CONTENTS
(Continued)

Chapter **Page**

TABLE OF CONTENTS
(Continued)

Chapter **Page**

LIST OF TABLES

LIST OF FIGURES

LIST OF FIGURES
(Continued)

Figure **Page**

LIST OF FIGURES
(Continued)

Figure **Page**

LIST OF FIGURES
(Continued)

Figure **Page**

CHAPTER 1

INTRODUCTION

1.1 Background

Much of the recent research in exhaust particulate control by industry has focused on the development of soot filtration devices and oxidation catalysts with an emphasis on reducing diesel exhaust soot emissions. In many industrial applications, electrostatic precipitation is the preferred method for particulate control. Soot particle control is important both environmentally and for health reasons. Soot is a suspected carcinogenic hazard due to particle absorption in lung tissue of inhaled particles (NIOSH 1988).

The current industrial approach for controlling diesel exhaust soot is use of filtration traps containing small passage monolith catalysts (Khalil and Levendis 1992; Shinozaki et al. 1990; Barris 1990). Small channels are needed to enhance particle diffusion to the catalytic surface. Due to varying operating conditions of diesel engines (e.g., idle to full load), particles accumulate and tend to clog the passages. The resulting back pressure reduces both the effectiveness of the filter and diesel engine performance. Methods of increasing exhaust temperature in order to enhance catalytic oxidation of the soot have resulted with some success in reducing particle buildup, at the expense of complicating the monolith design.

A catalyst is a material that increases the chemical reaction rate (molecules converted per unit time), at a given temperature without being consumed. Conversely,

reaction rates are increased with the desired conversion occurring at a lower temperature. The catalyst provides a chemical shortcut in which reactants are converted more rapidly than if no catalyst were present (Heck and Farrauto, 1995).

Recent studies have focused on the liquid fractions of diesel soot. These liquids, called soluble organic fractions (SOF), consist of unburned hydrocarbons from the diesel fuel and lubricating oils that leak into the pistons (Heck and Farrauto, 1995). SOF is present in both the gas phase and on the soot particles themselves. These studies, using small passage flow through monolith catalysts, have found that the SOF condenses in the catalyst pores at low temperatures. There it vaporizes upon heating and is catalytically oxidized. The suggested importance of SOF is that heat generated by catalytic oxidation of the SOF inside the pores may sufficiently increase local surface temperatures in order to enhance the oxidation of carbon soot particles deposited on or near the catalytic wall.

The solid carbon component of particles in soot are more difficult to oxidize than SOF because the particle is much larger than the catalyst pores. It tends to attach itself to the flat surface of the catalyst where there are fewer active sites. Thus, the carbon particles do not diffuse into the pores where most of the catalytic active sites are present (see Figure 1.1). An active site is a point on the catalyst surface that forms relatively strong chemical bonds with an adsorbed atom, molecule, or particle. The active component of catalysts typically used in this application are elemental platinum (Pt), palladium (Pd), rhodium (Rh), or vanadium pentoxide (V_2O_5) which are dispersed over a high surface area support material. This support material is usually a ceramic such as alumina (Al_2O_3) or titania (TiO_2). The alumina is a porous material that is deposited on a

ceramic or metallic monolith as a washcoat. The majority of the catalytic active sites are deposited in the pores of the support, because that is where the largest fraction of surface is present. Typically, pore diameters range from 2-10 nm.

The individual soot particles are small, solid, irregularly shaped particles approaching spheres composed of carbon and SOF with mean diameters of less than 1 μm. Non-catalytic, rapid oxidation temperature of diesel particles is approximately 600 °C (Dettling and Skomoroski, 1985; Kennedy et al., 1991). The presence of a catalyst reduces the temperature necessary to oxidize the particles assuming there is sufficient oxygen. Temperatures of approximately 400 °C for diesel soot oxidation have been experienced with catalysts containing platinum, palladium, and rhodium (Wyatt, et al., 1993).

Traditional methods of particulate control using electrostatic precipitators have been widely used (Flagan and Seinfeld, 1988). A particle laden gas flows into a region where an external electric field charges the particles, causing them to migrate to an oppositely charged electrode. Typically, circular tubes and rectangular ducts are used with a discharge electrode running down the tube or duct centerline. The collecting electrode is the wall around the charging electrode. The charged particles are entrained on the wall by electrical attraction. As the layer of charged particles grows, the charges on the most recently collected particles must be conducted throughout the layer of previously collected particles. The particles closest to the collecting electrode eventually lose most of their charge and the electrical attraction between the two becomes weakened. Newly charged particles building up the outer layer retain their full charge and serve to hold the

entire layer against the electrode. This occurs because the layer serves to insulate the newly arrived particles from the electrode, so these particles retain their charge longer (Flagan and Seinfeld, 1988). The collecting layer is removed by mechanically rapping the wall.

Electrostatic precipitation is very effective for particle entrainment. However, the particles (i.e. soot) are only collected, not destroyed in the precipitator. Catalytic filters destroy soot, but they tend to easily clog. Thus, a technology which incorporates large diameter, flow through channels to avoid clogging, and a mechanism to drive the soot particles to a catalyst surface should be considered. Hence, the idea of combining electrostatic precipitation with a catalytically reactive wall as a means of destroying soot particles was undertaken in this research.

1.2 Objectives

The main goal of this research is to examine the use of electrostatic precipitation to enhance diffusion of soot particles in a flow-through channel with a catalyst-lined wall. The information from this research will guide future designs of possible compact devices for reduction of diesel engine soot emissions. Specific objectives of this dissertation have been to:

(1). Design, build, test, and operate an experimental apparatus for producing a soot stream for flow through a catalyst-lined reactor tube; and to conduct gas and soot particle sampling and analysis at the tube inlet and exit.

(2). Determine the effectiveness of the electrocatalytic reactor as a soot oxidizer as a function of two key operating parameters not affecting reactor residence time: applied precipitator voltage and SOF concentration.

(3). Develop, solve and test appropriate mathematical models to predict axial penetration along the reactor tube length as a function of applied field strength. Predicted penetration will be compared with the relative change in measured loadings in the outlet of the reactor tube.

(4). Propose design guidelines for an electrocatalytically enhanced catalytic reactor for exhaust soot reduction.

1.3 Research Approach

A bench scale swirl combustor and a catalyst lined reactor tube were designed and built in order to produce a stable soot stream and to perform the experimentation for this research (see Figures 1.2 and 1.3). Electrostatic precipitation was used to enhance particle transport to the catalytic surface. The catalytic lining, in the form of a stainless steel monolith thin sheet with a bonded Al_2O_3 washcoat, was rolled and inserted into 1" i.d. reactor tube. A filter paper and gas sampling system was designed and built to perform the analysis and determine the effectiveness of the reactor tube as a catalytic oxidizer of soot.

Before discussing the experimental conditions, a brief explanation of commonly used terms is presented.

The feed rates of fuel and air for combustion are characterized by the fuel equivalence ratio (ϕ). The equivalence ratio is defined as:

$$\phi = \frac{(Fuel\ /\ Air)_{actual}}{(Fuel\ /\ Air)_{stoich.}} \qquad \text{(E1.1)}$$

where fuel and air stand for volumetric or molar flow rates of fuel and air in the feed mixture. For a fuel-lean (oxygen-rich) feed, $\phi < 1.0$; whereas, for a fuel-rich (oxygen-lean) feed, $\phi > 1.0$. At stoichiometric conditions, $\phi = 1.0$.

An equivalence ratio of between 1.3-1.4 was chosen and maintained in the range for the entire experimental runs. This condition was based on the performance of the swirled combustor to produce a light to moderate soot stream for electrocatalytic oxidation. A moderate soot loading flowing through the reactor allowed for:

(1). variation in applied voltage using the DC power supply without reaching the maximum current of the device due to soot-induced electrical short circuiting.

(2). the amount of soot collected on the filter paper to be dark enough so that changes would be detectable as voltage was increased.

(3). Changes in CO and CO_2 concentration detectable during voltage variation.

Another parameter held constant was the gas stream temperature entering the catalyst-lined reactor tube. The soot laden gas stream temperature exiting the combustor was well over 1000 °C. Thermal limitations of the catalytic lining and electrical insulating material in the reactor section precluded temperatures above 550 °C. The catalytic reactor section was maintained in the range of 400-450 °C. A means of cooling the gas

stream temperature in a short distance without complicating the experimental design was needed. A practical alternative was the use of pressurized liquid nitrogen. The liquid N_2 flow was sprayed into the combustion exhaust gas stream in order to reduce the gas temperature entering the reactor tube to approximately 370 °C.

With the parameters ϕ and reactor tube inlet temperature held constant, the volumetric gas flow rate (ν) through the catalyst lined reactor tube was maintained in a fairly narrow range. It was especially important to maintain a constant reactor residence time (τ) for the soot-laden gas. The residence time is given by:

τ = reactor tube volume (V)/volumetric flow rate at reactor outlet conditions (ν)

The gas volumetric flow rate is a function of molar flow rate, pressure, and temperature and is expressed in the following equation:

$$\nu = \nu_o \left(\frac{F_T}{F_{To}}\right)\left(\frac{P_o}{P}\right)\left(\frac{T}{T_o}\right) \qquad \text{(E1.2)}$$

where ν_o = gas volumetric flow rate at the tube inlet, F_T = gas molar flow rate at the reactor tube outlet, F_{To} = molar flow rate at reactor tube inlet, P_o = inlet pressure, P = outlet pressure, T_o = inlet temperature, and T = outlet temperature. Therefore, by maintaining a constant ϕ and constant temperature, a fairly consistent volumetric flow rate, as well as a stable residence time, were achieved.

On the other hand, two parameters that were varied independent of reactor residence time were:

(1). the use of adding vaporized toluene into the soot stream as a way of coating the carbon particles with an oxidizable hydrocarbon in order to simulate SOF.

(2). the voltage potential applied to a central wire running down the axial length of the reactor tube.

The flow rate of vaporized toluene (SOF) using air as a carrier gas was held at either 360 or 600 cm^3/min. The purpose of this parameter variation was to determine if the use of toluene would enhance catalytic oxidation of trapped carbon particles on the porous surface.

The objective of electrostatic precipitation is to find a voltage range in which the catalyst can oxidize a rate of particle accumulation to the surface. The experiments will show whether the combined effects of voltage and SOF variation enhance the catalytic oxidation of soot.

With the experimental conditions defined, a series of experiments following a logical sequence were performed. Soot loadings in the gas stream at the reactor inlet and outlet were determined by filter paper sampling. Gas analyses were done by gas chromatography. A particle counter was used to estimate the soot particle size distribution. The matrix of experiments were as follows:

(1). Soot stream flowing through a blank (non-catalytic) tube without added SOF and no external electric field. Filter paper samples were used to show that inlet and outlet reactor soot concentrations were the same. The blank tube was also used to visually inspect (as best as possible) for a uniform soot coating on the inside wall. No gas chromatography was performed.

(2). Soot stream flowing through the blank (non-catalytic) tube with an external electric field applied. Filter paper samples and use of the particle counter were

used to show how soot concentration changes with variation in electric field strength. Visual inspection of the blank tube gave some idea how the soot was being entrained on the blank tube inner surface. No gas chromatography measurements were performed.

(3). Soot stream flowing through the catalytic reactor tube. No external electric field was used. Filter paper sampling and gas chromatography were performed to determine if diffusion of soot particles, unaided by electrostatic forces, results in catalytic oxidation. Addition of SOF was introduced to determine any enhancement of catalytic oxidation.

(4). Soot stream flowing through the catalytic reactor tube and an applied external electric field. Filter paper sampling and gas chromatography, as well as particle counting were performed to determine changes in particle concentration and amount of catalytic oxidation of soot.

(5). Soot stream flowing through the catalytic reactor tube and an applied external electric field. Experimental runs included variation of electric field. Addition of SOF was performed in order to determine if SOF enhanced the catalytic oxidation process. This fifth set of experiments then determined the path for the preferred operating conditions to obtain the premier data set upon which final conclusions are made.

This sequence of experiments was designed to work out design defects and find the right operating conditions to build a set of premier data. The set of experiments for use in the

data base was designed to be small, but with sufficient results to satisfy the goals of this research.

The set of experiments for the data set are:

(1). Full-up system using a catalyst lining, center wire, low flow soot laden gas stream (< 4.0 m/sec or 0.068 m^3/min) through the reactor tube, and oxygen addition to the soot stream. Voltage variation on the central wire (0 volts to some maximum potential without arcing or short circuiting) were performed in all cases. Gas chromatography, soot filter paper sampling, and particles counts analysis were used in the analysis in all cases. These runs are further subdivided into:

(a). Data collection (for voltage variation) for constant catalyst surface temperature and oxygen addition (with and without SOF).

(b). Data collection with raised catalyst surface temperature at same oxygen flow rate.

(c). Data collection with lower catalyst surface temperature as in (a). with increased oxygen flow rate.

(d). Data collection for variation with higher catalyst surface temperature and increased oxygen flow rate.

Observations and learnings from the previous sequence of experiments were used in setting up and supporting the data base matrix.

Mathematical models were used to predict the penetration of each particle size as well as total penetration of all fractions along the axial distance, with and without an external electric field. The modeling effort began by deriving the governing equations for

flow using a single particle size and charge with no applied field, as defined by Chen (1978). His model was enhanced by including multiple fractions in order to approximate the actual size distribution. A different solution technique was used and tested with a single fraction so that it reproduced Chen's results. The mathematical model was run using an existing algorithm called Chebyshev Polynomial Software for Elliptic-Parabolic system of partial differential equations (PDECHEB) developed by Berzins and Dew (1991). PDECHEB uses Chebyshev polynomials to approximate a continuous solution of the PDE between each pair of spatial breakpoints. The advantage in using this software is its ability to handle a system of partial differential equations (PDEs) which result from considering multiple size fractions. Each fraction has specific values for a_i (radius), q_i (charge), and D_i (diffusivity).

When the applied field (V_o) was added, PDECHEB began to develop instabilities as V_o was increased. This occurred because of changes in the flux contributions comprising the governing equations. A moving, radial, particle density gradient, beginning at the center wire radius and moving out to the tube radius as axial distance increased, caused instabilities because PDECHEB could not stably approximate the solution using a fixed radial grid. Therefore, a different mathematical model was developed to overcome these effects.

The model predicting axial penetration of individual fractions, as well as total particle number and volume penetration, in the presence of a varying applied field was developed mathematically and tested. The form of the governing equation was modified because particle flux contribution due to the electric field tended to dominate the change in

particle density along the axial direction. Model predictions agreed well with the trends exhibited by the experimental data. These data consisted of soot reduction as measured by analyzing reactor tube outlet filter paper.

CHAPTER 2

LITERATURE SURVEY

2.1 Electrostatic Precipitation

2.1.1 Control Device for Exhaust Soot

Electrostatic precipitation on diesel exhaust soot as an alternative to the catalytic filter and particulate trap designs described in Chapter 1 has been extensively studied (Masuda and Moon, 1983; Kittelson et al., 1986, 1991; Hamilton Maurer International, Inc., 1988; Thimsen et al., 1990; Farzaneh et al., 1994). All designs have collected or entrained diesel soot with and without the use of an external charging mechanism (e.g. corona). However, the emphasis has been on collection rather than a means for destroying soot.

Kittelson, et al. (1986) found that diesel particles have bipolar charges (particles with equal numbers of positive and negative charges) based on charging mechanisms by Moon (1984), and that the combustion process in a diesel engine produces enough particle charge without the need of an external charging mechanism (e.g. corona discharge). He mentioned that the voltage required for electrostatic precipitation was a "few kV", but it was likely to be 3-5 kV, as stated by the follow-on study by Thimsen, Kirby, Braumgard, Kotz, and Kittelson (1990). The conceptual drawing of his electrostatic trap was a large circular cylinder with a parallel array of concentric tubes each with an electrostatic device. Basing his calculations for a diesel engine operating near heavy load conditions, and with an assumed charging fraction of 80%, Kittelson claimed his design could conceivably

collect 60% of the dry carbon particles. This design was based on a device 3 ft long with laminar flow. He, therefore, considered his simple electrostatic precipitator design in the absence of a corona to be a great advantage as a diesel particulate control device because of economical power requirements.

Thimsen, et al. (1990) followed with an electrostatic agglomerator designed to increase particle size growth by collection and subsequent reentrainment for easier removal of particulates from diesel exhaust. An electrostatic agglomerator is a device that collects and reentrains diesel particles, but does not require any regeneration. Agglomeration by electrostatic forces resulted in shifting particle size distribution from the submicron range (< 1.0 μm) to particles greater than 1.0 μm under heavy engine load conditions. In an electrostatic agglomerator, reentrained soot particles could either be recycled to the engine for combustion or disposed of by other means.

These studies in the 1980s had a higher percentage of dry carbon (soot) particulates as compared to current diesel engines. For example, diesel truck particulate emissions in 1986 as measured in grams/brake horsepower hour (g/bhp-h) were 0.6. Diesel engine manufacturers have since made design changes to reduce the dry carbon particulates to 0.25 g/bhp-h or less. However, as a result, the percentage of SOF increased. A typical breakdown of diesel emissions from more recent engines shows that dry carbon is about 43%, while total (lube and fuel) SOF is 55% (Heck and Farrauto, 1995). The challenge with electrostatic precipitators is whether collection efficiency can be increased with more SOF present in diesel exhaust.

Kittelson, et al. (1986) found a relationship between the high volatile fractions and low charged particle fractions, inferring that the low charged particles with condensed SOF were less likely to be captured by electrostatic precipitation. Therefore, SOF was assumed to have a less pronounced effect on particle collection in these studies.

Kittelson et al. (1991) continued from the Thimsen design by conducting further studies on electrostatic collection and agglomeration. He measured particle size, charge, and concentration. The applied voltage used in electrostatic precipitation mostly ranged from 3 to 5 kV in cylindrical and square tube geometries with three different size high voltage rod radii. Kittelson found that collection efficiencies ranged from 17% to 40% using these geometries. His results showed that the cylindrical tube with the smallest high voltage rod radius had poorest collection efficiency. On the other hand, the square tube geometry with the highest high voltage rod radius had the highest collection efficiency. Kittelson also showed that agglomeration amounted to approximately 30-40% reduction in sub-micron mass.

Farzaneh et al. (1994) followed up from the studies of Kittelson and Thimsen with the addition of a corona to charge the diesel soot particles. He claimed that the charge on each particle as a result of combustion and friction was low, and that a large part of the diesel particles were not even charged. Therefore, an external charging means was necessary in order to have collection efficiencies of over 90 % within a short distance. He used a negative dc corona for charging particles because of its higher operating voltages and currents, which is consistent with earlier studies (White, 1951). The corona was not a separate device, but was part of the precipitator itself. Farzaneh simply increased the

applied voltage to the discharge electrode until he produced a highly visible glow near the central wire, indicating the presence of a corona. An electron avalanche is created, and the electrons quickly collide with gas molecules to produce negative ions. Soot particles flowing through this field are bombarded by these ions and are quickly charged.

Farzaneh used four hexagonal cells with an equivalent tubular diameter of 5.08 cm (2 in) and length of 20 cm. The discharge electrodes were rigid and electrically insulated using teflon. Farzaneh increased the applied voltage in his electrostatic precipitator until he produced a corona discharge which occurred above -18 kV. He showed collection efficiencies dramatically increased when the applied voltage was increased above -18 kV. The collection efficiency went from 0 to 18 % for voltages up to -10 kV, and was 22 % at -18 kV. At -19 kV the efficiency increased to 59 % and went up to 95 % at -26 kV. His studies were consistent with an earlier effort by Lin, et al. (1989) who also used corona charging as a more efficient way of removing diesel soot.

Previous to Farzaneh, et al.; Kittelson and Thimsen, et al.; Masuda and Moon (1983) devised a different concept for diesel soot removal by using a moving belt-type electrostatic precipitator. They found that diesel soot removal was difficult because of soot contamination on the wire electrode insulators. The other mentioned authors also found this to be a problem and had to devise ways of isolating the discharge electrodes. Masuda's design consisted of a precharger, or a negative dc corona, a precoagulator to agglomerate the carbon particles to a size of 1 μm mass-median diameter, and a moving belt type electrostatic precipitator to remove the agglomerated particles.

2.2 Catalytic Oxidation

2.2.1 Catalytic Oxidation for Particulate Control

Ongoing research into the use of noble metal and metal oxide-based catalysts have shown that oxidation of soot particles takes place at significantly lower temperatures than in the absence of a catalyst. Thermal oxidation of deposited soot requires relatively high temperatures for ignition and a long residence time. Much of this research has focused on diesel exhaust soot where particle ignition temperatures without the use of a catalyst occurs in the neighborhood of 550-600 °C (Dettling and Skomoroski, 1985).

Ciambelli et al. (1990, 1991, 1993) conducted studies using diesel exhaust soot, carbon black, and graphite oxidation on metal oxide-based catalysts. The catalysts were prepared by impregnating 50 μm mean diameter α-alumina and γ-alumina particles with aqueous solutions of metal salts containing Cu, Cr, K, Mn, Ni, and V, and then calcination at 700 °C. The studies using thermogravimetic analysis (TGA), and differential thermal analysis (DTA), indicated best results with the Cu/K/V catalyst. Catalytic oxidation of diesel particles occurred at approximately 330 °C. Their results also showed that catalytic oxidation was controlled by gaseous oxygen concentration and soot-to-catalyst weight ratio. Ciambelli et al. (1991) stated that, for soot conversions up to 50 %, the rate of catalytic combustion is linearly dependent on soot mass and oxygen partial pressure.

Other metal-based oxide catalysts such as V_2O_5 and oxides of Cu, Mn, and Cr, as well as Ag and Pt, were used by Ahlstroem and Odenbrand (1990) to catalytically oxidize diesel soot. The catalysts were prepared in a similar manner as Ciambelli, et al. had done. Their studies indicated that V_2O_5 was highly active in catalytic combustion of diesel soot

at temperatures above 623 K and that soot combustion took place mainly on the external surfaces of the catalyst. Catalytic combustion of hydrocarbons (SOF) desorbed from the soot took place in the internal surface area of the catalyst. This occurred because hydrocarbons were capable of diffusing into the pore structure of the catalyst. Alhstroem and Odenbrand found that Ag, Pt, and oxides of Cu, Cr, and Mn had high activities at temperature below 623 K for combusting hydrocarbons. In addition, Ahlstroem and Odenbrand found that the V_2O_5 catalyst had a high resistance to SO_2 poisoning. Gaseous SO_2 is released as the diesel soot is heated. Metal oxides such as Mn are very sensitive to SO_2 poisoning and are quickly deactivated.

Catalysts such as Pt and Pd, which have a high activity for oxidizing SOF, also have a high activity for SO_2 oxidation to form sulfate (Heck and Farrauto, 1995). The problem with SO_2 oxidation is that the sulfates produced quickly form sulfate particulates. Thus, the effect of reducing soot particles from diesel exhaust by increasing the percentage of SOF unexpectedly caused a corresponding increase in sulfate particulates when Pt and Pd catalysts were used.

Kraemer and Pfefferle (1990) flowed a fuel rich mixture of vaporized hexane and air through platinum and manganese coated reactor tubes. They found that major reaction product was CO_2, which was detected using the Pt catalyst as low as 523 K for $\phi = 4$, and 597 K for $\phi = 10$ to a temperature of 773 K. At higher temperatures, they discovered that the platinum catalysts promotes further gas phase decomposition of the hexane producing more ethane, ethene, butane, and butene. Carbon monoxide was not detected until temperatures reached 973 K. At temperatures > 973 K, the Pt catalyst promotes gas

phase oxidation of ethane, ethene, butane, and butene to CO and CO_2. On the other hand, conversion of hexane using the Mn-based catalyst began at 823 K for $\phi = 4$, an increase of 300 K over the Pt catalyst. Carbon dioxide was detected at 873 K for both $\phi = 4$ and $\phi = 10$. Kraemer and Pfefferle also observed that with the Mn catalyst, ethene and C4 hydrocarbons were detected at 873 K for $\phi = 10$, 923 K for $\phi = 4$. They believed that the presence of these hydrocarbons at higher temperatures was an indication that gas phase oxidation was not as efficient on the Mn-based catalyst as compared to the Pt catalyst.

2.2.2 Use of Flow-Through Oxidation Catalysts

A lot of research work has been in the design of flow-through oxidation catalysts for particle reduction in diesel exhaust soot (Horiuchi and Ichihara, 1990; Zelenka, et al., 1990; Beckmann, et al., 1992; Wyatt, et al., 1993). In this design, catalytically oxidized CO and hydrocarbons are at low exhaust gas temperatures, while the carbon particles are oxidized downstream at higher gas temperatures without oxidizing SO_2. Honeycombed ceramic monoliths with typical cell densities of 300-400 cells per inch providing flow-through capability were used. Wyatt, et al. (1993) found that the addition of vanadium to a platinum-based flow-through catalyst controlled SO_2 oxidation, while maintaining hydrocarbon (HC) and CO conversion. Beckmann, et al. (1992) also had similar results using a new generation of flow-through diesel oxidation catalyst. Zelenka et al. (1990) showed the effect on Pt loading for catalyst conversion of CO and HC. In general, the higher platinum loading results in higher conversion at all operating temperatures of a diesel engine for both fresh and aged catalysts. Platinum is especially significant as a

catalyst because of its low temperature activity to convert CO and HC. Kennedy, et al. (1991) also stated that higher Pt loading significantly increased the rate of combustion of peat smoke.

Voss et al. (1994) conducted diesel exhaust studies using platinum/palladium catalyst of various loadings with washcoats of different proprietary base metals, and evaluated the aging performance in HC, CO, total particulate matter (TPM), volatile organic fractions (VOF), and sulfate percent reductions. He used a flow-through honeycomb substrate with a catalyst coating containing 400 cells per square inch. Voss et al. found that a catalyst with either 0.5 g/ft^3 Pt or 50 g/ft^3 Pd in an alumina/proprietary base metal oxide gave the best overall performance after 1000 hours. These results were interesting because Voss et al. stated that these catalysts were highly selective against the production of sulfate.

2.2.3 Soluble Organic Fractions (SOF) and Catalytic Oxidation

Many of the studies in catalytic oxidation of diesel soot as described above have mentioned hydrocarbon (SOF) oxidation as part of the total oxidation process of diesel soot. The emphasis here is to describe a little more about SOF and its importance in catalytic oxidation.

The ability of a catalyst design is to adsorb and condense SOF into the porous support material at low temperatures (e.g. a diesel engine during start-up or idling). Once gas stream temperatures are increased (e.g. a diesel engine operating under a load or at high speed), the catalyst porous support material must be able to catalytically oxidize these

trapped fractions (Heck and Farrauto, 1995). The oxidation of SOF as described by Heck and Farrauto is shown by the following generic reaction:

$$SOF + O_2 \rightarrow CO_2 + H_2O \qquad (R2.1)$$

Wyatt, et al. (1993) provided laboratory oxidation activity results of Pt/alumina catalysts. He showed that CO conversion was nearly 100% at temperatures above 150 °C, and hydrocarbon conversion of 80% and better beginning at temperatures of 250 °C. The CO conversion at temperatures below 200 °C was consistent with Oh, et al. (1991) using methane oxidation over a Pt/alumina supported catalyst.

Arai (1993) conducted thermal analysis studies in evaluating SOF oxidation using Pt and Pd plus base metal catalysts. He performed his experiments using thermal analysis methods. Arai then determined the order of catalyst activation from the inflection points in the thermogravimetry (TG) curves, and DTA and differential scanning calorimetry (DSC) peak points. He extracted SOF from diesel soot using dichloromethane, and then evaporated the mixture so that concentrated SOF was left. Small pieces of a diesel catalyst monolith were soaked in the SOF solution for 24 hours and evaporated. The dry catalyst was then crushed in a mortar to obtain test samples. Arai showed that changes in temperature ramp rates did not change the shape of TG curves, but the position of the curves changed in the direction of the rate change. DTA peaks also changed in a similar proportional manner. Arai also used a lubricant as a substitute for SOF and found that thermal analysis results were different. He believed that the order of catalyst activation was different because SOF is composed of fuel and lubricant components. The oxidation of SOF occurred in the range of 200-500 °C for all catalysts.

2.3 Use of Electrostatic Precipitation and Catalytic Oxidation for Particulate Control of Soot

It appears that studies in combining electrostatic precipitation to enhance the diffusion of soot particles to a catalyst surface for catalytic oxidation in particulate control have not been published at this time. Hence, the current research has a high degree of novelty.

CHAPTER 3

EXPERIMENTAL METHODS

3.1 Schematic of Experimental Apparatus

The schematic of the experimental apparatus is shown in Figure 3.1. It consists of a swirled combustor and catalytic reactor tube fabricated from 316 stainless steel. Ancillary equipment and piping showing the pressurized air and fuel system for the combustor are also shown in Figure 3.1. A basic flow path for the sampling system using gas chromatography and soot filters is shown as well. Toluene, an aromatic compound, is used as the fuel because of its excellent sooting characteristics.

In the pressurized fuel system, liquid toluene is filled from a spout through a fill line into a 3.5 liter stainless steel flask. Two ball valves located on the top and bottom portion of the fill line are designed to isolate the line from the flask when it is pressurized and to prevent liquid toluene in the line between the bottom valve and spout from evaporating into the air. A second flask with a capacity of 2.2 liters is connected in a parallel arrangement and is placed in service as the first tank empties out. The stainless steel flasks are pressurized to 160-165 psig using nitrogen gas from a high pressure cylinder. The pressure blanket is required to provide a desired flow rate of toluene to the combustor through the pressure atomizing spray nozzle. The flasks are equipped with external sight gauges for tank level indication.

The pressurized fuel flows from the flask through a metering valve and 1/4 inch outside diameter (o.d) stainless steel tubing. A rotameter with a tube length of 65 mm and a stainless steel float installed just downstream of the metering valve provides measured flow.

Just downstream of the rotameter, a pressure gauge is installed to provide an indication of pressure needed to ensure atomization of fuel at the nozzle tip while adjusting flow. With pressure at 160-165 psig in the fuel tank and a flow metering valve to control pressure in the fuel line, a means to deliver a controlled liquid fuel flow rate is achieved.

The fuel then flows through a check valve and a 200 micron (μm) stainless steel filter for protection against a flashback flame. A ball valve is installed just after the filter and is used for turning on or quickly shutting off the fuel supply to the combustor. Lastly, the fuel flows through a high pressure atomizing nozzle to produce a fine spray mist. The nozzle, supplied by Hago Products, Inc, is a solid cone pattern with a spray angle of 30 degrees and nominal flow rate of 0.40 gallons per hour or 25.2 ml/min at 100 psig. The flow rate of the nozzle is completely determined by the pressure at the nozzle inlet. For flow rates other than the nominal flow rate, an expression is used to account for the different pressure at the nozzle inlet.

$$F_{Desired} = F_{Rated}\sqrt{\frac{P_{Desired}}{P_{Rated}}} \qquad \text{(E3.1)}$$

where $F_{Desired}$ = desired flow rate, F_{Rated} = nominal flow rate, $P_{Desired}$ = desired pressure (psig), and P_{Rated} = required pressure for nominal flow rate. It is difficult to know what the pressure at the nozzle inlet really is because of frictional losses due to valves, pipe

bends, expansions, and filters associated in a piping system. The pressure gauge located on the outlet of the rotameter is positioned such that the frictional losses described above are not detected. Hence, a desired pressure cannot accurately determine the actual flow rate of the nozzle. The nozzle flow rate is determined by capturing and measuring the atomized mist in a flask for one minute by maintaining a constant pressure using the pressure gauge on the outlet of the rotameter. By trial and error, a fuel flow rate of 22 m*l*/min with a pressure of 110 psig at the rotameter outlet was established as an acceptable flow rate while maintaining atomized mist quality.

An in-house compressor provides pressurized air at 100 psig for combusting the toluene. This air is metered by use of a Fisher and Porter (F & P) rotameter rated at 4.6 scfm (100% flow) at 14.7 psi (absolute) and 70 °F. A pressure gauge on the downstream side of the rotameter provides pressure indication. After the pressure gauge, the air line is split as shown in Figure 3.1. One line supplies swirled air and the other line supplies dilution air (described later) for the flame in the combustor. Both air lines are controlled by use of needle valves.

The air flow rate from the rotameter is corrected to incorporate the actual pressure and temperature of the compressed air. Therefore, the true flow rate is equal to a correction factor times the meter reading and is expressed in the following equation.

$$V_{Actual} = V_{Meter}\sqrt{\left(\frac{P_{Actual}+14.7}{P_{Calibrated}+14.7}\right)\left(\frac{T_{Calibrated}}{T_{Actual}}\right)} \qquad \text{(E3.2)}$$

where V_{actual} = corrected volumetric flow rate (scfm), V_{meter} = meter reading (scfm), P_{actual} = actual pressure as read on the outlet of rotameter (psig), $P_{calibrated}$ is calibrated pressure

(psig) as read on the meter face, T_{actual} = actual temperature of air (°R), and $T_{calibrated}$ = calibrated temperature (°R) as read on the meter face.

The objectives in the design of the combustor were to incorporate swirled and dilution air for combustion without significant complexity, while mounting the combustor, cooling and catalytic reactor sections, and associated equipment onto an available test bench measuring 72 inches in length by 21 inches in width by 72 inches in height. The combustor chosen is a dilute swirl design based on a bench scale model by Brum and Samuelson (1982).

A portion of the air flow for the flame is swirled by using a brass circular piece with a fixed worm gear groove fitted inside an inner annulus around the fuel line as shown in Figures 3.2 and 3.3. Metered air from the F & P rotameter flows into a single port of the fuel line and swirled air annulus assembly (see Figure 3.3) and is forced through the grooves to provide the swirled air. Since total air and dilution air are each metered (see next paragraph), the swirl air rate is determined by the difference.

An outer annulus is designed in the swirled burner assembly so that linear dilution air is used in conjunction with the swirled air to control flame length. The remainder of the air from the F & P rotameter is metered for use as dilution air. This air enters through two inlet ports located 180 degrees apart as shown in Figures 3.2 and 3.3 and flows through aligned air holes in the assembly. By experimentation with metered air and fuel flow rates, a flaw in the original design using a single inlet port resulting in incomplete combustion of the atomized fuel was discovered. Upon entry through the inlet, the air preferentially flowed through the air holes nearest to the port and substantially less

through the air holes furthest away. Therefore, a second inlet port located 180° from the first port was installed to equalize the dilution air through all air holes.

The fuel line and swirled air assembly is threaded so that it can be screwed into the burner assembly. This was done in order to facilitate dismantling and cleaning. The swirled burner assembly, with a total length of 5.625 inches, is bolted to the combustor section with flanges.

This combustor section is 10.5 inches long with an inside diameter of 3.25 inches. The inside surface of the combustor section is formed by a 3" o.d. by 2" i.d refractory alumina cylinder. The effective inside diameter of the combustor where the flame burns is 2.0 inches (see Figure 3.4).

A controlled hydrogen flame is used as an easily ignited pilot flame for the main combustor. A piezoelectric ignitor, commonly found in gas barbecues, provides a spark for igniting the hydrogen/air gas. The ignitor and pilot gas line is fitted together into an ignitor assembly (see Figure 3.4a) where it is threaded into the combustor section. A 90 micron filter is installed in the hydrogen flame line just prior to the needle valve for protection against a flashback flame. The pilot flame ignites the atomized mist of toluene fuel during start-up and is shut off after the flame stabilizes.

Two type R thermocouples, located 5.5" and 8.5" downstream of the spray nozzle, provide temperature indication in the flame region of the combustor. Nitrogen gas can be blown into the combustor tube to assist in extinguishing the flame in an emergency situation (Figure 3.4).

The hot soot-laden combustion gas stream then flows into a horizontal 12 in. by 1.8125 in. inside diameter (i.d.) stainless steel tube fitted with an annular water jacket. This cooling section is bolted to the combustor section with flanges. In-house chilled water flows counter to the gas and soot stream in order to cool the outer surface of this section. The gas temperature is monitored in this section using another R type thermocouple located just after the water jacket (see Figure 3.5). Based on experimentation, combustion gas stream temperatures are typically well above 1000 °C near the cooling section exit.

In order for the gas stream temperature entering into the catalytic reactor tube to be dropped to the 370 °C approximate needed temperature, cryogenic liquid nitrogen at approximately 20-25 psig is injected into the cooling section. Liquid nitrogen flow is controlled by manual adjustment of a flow metering valve located near the elbow and observing the thermocouple temperature in the elbow nearest to the reactor tube entrance.

Upon exiting the cooling section, most of the soot laden gas flows through a horizontal 1.875" i.d. tube off the elbow (see Figure 3.6). Most of the gas stream bypasses the catalytic reactor tube and exists from the system. The amount of bypassed flow is controlled by using an orifice. The remaining gas stream flows up through the reactor tube where the effects of an external electric field and catalyst on the soot particles will be analyzed. This bypassing arrangement is necessary to reduce gas velocity (i.e. increase gas residence time) through the catalytic reactor.

The elbow has a 90 ° angle with an i.d. of 3 inches. Several penetrations in the elbow allow for injection of vaporized toluene (SOF) into the gas laden soot stream

entering the reactor tube, gas chromatography and filter paper sampling, particle counting, and temperature monitoring using a K type thermocouple. Vaporized toluene as a soluble organic fraction (SOF), co-mixed with metered oxygen, flows through 1/4" stainless steel tubing and enters through a penetration in the bottom of the elbow as shown in Figures 3.6 and 3.9.

The vaporized SOF toluene originates as a liquid in two partially filled glass flasks equipped with spargers (called gas saturators or bubblers) as shown in Figure 3.9. The carrier gas used to vaporize toluene is air. Air from a gas cylinder is controlled by a 0-3 psig pressure regulator to approximately 1.4 psig. This air is metered by a rotameter to obtain a desired flow rate. This flow rate generates steady bubbling in the gas saturators and produces toluene-saturated air. The bubblers are immersed in an ice bath in order to reduce the toluene vapor pressure (3.47 kPa at 25 °C), and hence the concentration of toluene in the gas phase. The temperature of the liquid toluene in the flasks is about 1 °C using the ice bath. Two bubblers in series are used to ensure that the air in the bubblers is saturated with toluene. The derivation of the flow rate and concentration of the vaporized toluene is shown in Appendix B.

The vaporized toluene and carrier gas exit the bubblers and flow through a check valve where it enters into a tee. A K type thermocouple and low pressure gauge (0-3 psig) located just prior to the check valve provide temperature and pressure indication at the outlet of the bubblers. Outlet pressure is approximately 0.5 psig for a carrier gas flow rate of 350 m*l*/min. The vaporized toluene and carrier gas then flows through a 90 micron cartridge filter and into the bottom of the elbow as shown in Figure 3.6 and 3.9.

A sampling port for measuring concentrations of the combustion gases and the soot stream mass density prior to entering the catalytic reactor tube is located at the top portion of the elbow. The piping is 1/4" stainless steel tubing and is configured to sample the low flow gas stream going into the catalytic reactor. The inlet sampling port can also be used to direct the soot laden gas stream to the particle counter by simply changing the valve line-up (see Figure 3.14).

The catalytic or reactor section consists of a stainless steel cylindrical tube with an i.d. of 1 inch and length of 18.125 inches as shown in Figure 3.7. Seven penetrations along the axial length of the tube house type K wire thermocouples sheathed in ceramic for temperature indication of the catalyst sheet. The ceramic sheathing electrically insulates the thermocouples from the metal catalyst sheet. The catalyst material is a flat stainless steel sheet treated with alumina washcoat at 30 mg/in^2 surface concentration and platinum at 0.5 mg/in^2. The platinum accounts for approximately 2.0 % of the washcoat mass. This catalyst mesh is rolled and fitted inside the outer tube such that the ceramic sheathed thermocouples touch the back surface of the catalyst sheet. The catalytic reactor is housed in a three zone tube furnace equipped with three separate temperature controllers.

A central wire (0.060" in diameter) runs axially down the tube length and is electrically charged. Together with the electrically grounded catalyst sheet, the wire functions as an electrostatic precipitator. The wire is fed through an electrically grounded support and is held in place using a collar with a set screw on both ends of the reactor tube (see Figure 3.8). The power supplied to the central wire comes from a Glassman Model

MJ30N400 DC power supply rated from 0 to -30kV and 0 to 0.4 milliamps of current. The power cable from the DC power supply and the thin central wire are connected and held together by use of copper posts mounted onto an insulated board. This arrangement facilitates removal of the thin wire when the reactor tube is disconnected from the elbow. A ceramic insert between the elbow and reactor flanges is used to electrically isolate the reactor tube from the elbow section.

Voltage and current measurements are monitored using a Hydra Fluke 2620A data acquisition unit. Voltage is increased or decreased by use of a potentiometer on the DC power supply. The digital output for voltage and current on the data acquisition unit is read in kVolts and microamps, respectively. Current measurement indicates electron flow in the radial direction beginning from the central wire to the grounded reactor tube surface. When current reaches its maximum value of 400 microamps, the DC power supply has a limiting device to prevent voltage from increasing even though the potentiometer can still be turned.

3.2 Analytical System

The analytical system is composed of three subsystems covering sampling and analysis for gas composition, soot mass density, and soot particle size. Each subsystem is described separately below.

The gas and soot sampling and gas analytical systems are shown in Figure 3.10. The sampling or transfer line to measure inlet concentrations is located in the elbow section. A vacuum pump (#1) draws sample gas through a calibrated rotameter. The sample gas flows through 1/4" stainless steel tubing and into a water vapor condensate

trap to remove condensate in the line before it flows through the rotameter. The soot filtering system is also located in the transfer line just prior to the condensate trap. During gas sampling, the filters remove soot particles to prevent clogging the rotameter and interfering with the gas chromatography. After the rotameter, a tee in the sample line allows for gas/particulate sampling and particulate sampling only. The line for particulate sampling using vacuum pump #2 is installed as a back-up only and is not normally used.

3.2.1 Gas Sampling and Analysis

For gas sampling, the ball valve in the path to vacuum pump #2 is shut while the ball valve for gas sampling is opened (normal flow path) allowing combustion gas to be drawn by vacuum pump #1 to the Hewlett Packard HP 5840A Gas Chromatograph (GC). The transfer line is approximately 320 inches (8.13 m) in length from the inlet sampling port to the inlet of the six (6) port gas sampling valve located on top of the GC. The transfer line is heated from the outlet of the rotameter to near the inlet of the six port sampling valve using coiled heater strips, and insulated with thermal cloth. The heater strips are connected in a parallel arrangement with three strips in series. This arrangement prevents overheating of the heater strips with too high a current. Temperature is maintained at 100 °C to prevent water vapor condensation which can effect concentration levels of CO and CO_2. An Omega Model CN370 K temperature controller wired to an external relay is used to keep the temperature constant in the transfer line. A rugged and replaceable external relay, controlled by the CN370, actually switches the heater circuit load because the contacts in the CN370 relay are less durable.

The six port gas sampling valve is housed in an insulated heater box and maintained at 100-115 °C by use of a variac. Gas sampling flow rate is controlled through the use of two needle valves with their corresponding pressure gauges located on the inlet and outlet lines (sampling loop) of the six port gas sampling valve as shown in Figure 3.10. A pressure difference is maintained between the two pressure gauges by adjustment to obtain an average pressure across the gas sampling loop on the six port gas sampling valve. The flow rate from the adjustment of the two needle valves is known by reading the calibrated rotameter, as described in paragraph 3.2, located on the instrument panel of the test bench assembly.

The vacuum pump (#1) continuously draws sample gas through the transfer line to the GC. When the six port gas sampling valve is in the collection or load position, gas flows continuously through the 1.0 m*l* sampling loop and outlet line (see Figure 3.10a). When the sampling valve is switched to the inject position, the gas flow in the transfer line bypasses the sampling loop and the carrier gas line now flushes the 1.0 m*l* loop to the GC packed column.

Table 3.1 Operating Gas Flow Rates in the Gas Chromatograph

Gas	Flow rate (m*l*/min)*	Cylinder Press. Gauge (psig)
He (carrier gas)	31	33
H_2 (FID)	15	29 (total H_2)
H_2 (to catalyst converter)	15	
Air (FID)	308	35

Flame Ionization Detector (FID) temperature: 225 °C

* GC oven temperature = 50 °C

The operating flow rates of carrier gas, hydrogen, and air are shown in Table 3.1. The gas chromatograph is equipped with one 1/8" o.d. and 6 ft length stainless steel packed column. The packing material used is Porapak Q because of its ability to separate toluene, benzene, CO, CO_2, and C_1-C_2 hydrocarbons. Helium (zero grade) is the carrier gas used. The packed column effluent flows through a catalyst material of ruthenium (5%) on alumina powder where CO and CO_2 gas are converted to methane (CH_4) in the presence of excess hydrogen gas and at a temperature of 300 °C. All other gases are unaffected. This methanizer and assembly are shown in Figure 3.11. The methanizer is needed since a GC flame ionization detector will not detect CO and CO_2. The housing for the catalyst material consists of a 5 inch length of 1/4" stainless steel (s.s.) tubing with Swagelok nuts and 1/4" to 1/8" reducing unions on each end. The ruthenium is filled in the middle 2 inch portion of the housing and is held by stuffing glass wool on each end. In addition, glass beads of approximately the same diameter as the inner diameter of the housing are filled to each end and held in place by the reducing unions (see Figure 3.11). The gas flow from the packed column follows a tortuous path around the glass beads and through the ruthenium catalyst.

The catalyst material is originally in powdered form and is compressed to form a tablet using a die cast and hydraulic press. Approximately 20 grams of ruthenium is needed to make a 1/2" diameter tablet of varied thickness so that it can broken into small chunks and fitted into the 2" section of the housing. The 1/4" s.s. housing is placed between two rectangular aluminum blocks and bolted together. A cartridge heater is embedded in the bottom half of the aluminum block and connected to a variable

autotransformer (variac) and set at approximately 40% of maximum output voltage to attain a constant 300-305 °C. A type K thermocouple is also housed in the aluminum block to provide temperature indication. Excess hydrogen gas is fed into the gas stream through a tee on the upstream side of the housing (see Figure 3.11) The aluminum block is then covered with insulating material and is placed on top of the gas chromatograph.

The separated species are then determined by a flame ionization detector (FID). Separate peaks are recorded and integrated by the GC integrator. Scott Standard gas mixtures of CO, CO_2, CH_4, C_2H_2, C_2H_4, C_2H_6 at 1.0 % by volume are used to provide the species retention times and calibrated integrator areas in order to identify and determine the concentration (mole fraction) of combustion gases during experimentation.

Single point calibrations of the standard gas are performed prior to each experimental run for that day. Standard gas, under pressure, is introduced into an evacuated portion of the transfer line. The sampling loop is then filled with standard gas by slowly opening the upstream needle valve (See Figure 3.10). The gas sampling loop is evacuated prior to allowing the standard gas to flow in. A needle valve located upstream of the gas sampling loop is slowly opened until 18" of vacuum is reached. This pressure is approximately the condition during sampling when the vacuum pump is drawing the combustion gas stream through the transfer line. Once the GC integrator areas are recorded using the standard gas at 1.0 % by volume, the unknown concentration of the same gases can be calculated by the ratio of the integrator areas as follows:

$$Concentration\ (\%\ by\ volume) = Conc_1 \frac{Area_2}{Area_1} \qquad \text{(E3.3)}$$

where $Conc_1$ = known concentration of standard gas (% by volume), $Area_1$ = GC integrator area of standard gas, and $Area_2$ = GC integrator area of sample gas.

Toluene, on the other hand, was calibrated from measured tiny amounts (microliters) of liquid injected into 160 m*l* serum bottles. The resulting gas mixtures containing evaporated toluene and air in sealed serum bottles were injected into the GC for different toluene concentrations using a gas syringe. Toluene calibration was done on a mole basis in order to calculate its concentration (mole fraction) from the GC output to the total gas injected for analysis.

Toluene was injected into the serum bottles at 1.0, 2.0, 3.0, 4.0, 7.0, and 8.0 μ*l* using a liquid syringe and then sealed with a teflon stopper and cover. Three serum bottles were used at each liquid volume so that an average detector peak and integrator area could be established. The liquid volume of toluene injected into the serum bottle is converted into moles (n_1). A sample calculation for determining moles and concentration of toluene in the serum bottles is shown in Appendix C. The evaporated toluene and air in the serum bottles were drawn at a volume of 1.0 m*l* using a gas syringe and injected into the GC injection port for analysis. Since the pressure and temperature of the gas in the syringe is assumed to be the same as in the serum bottle (temperature = 25 °C and pressure = 1 atmosphere), the relation $n/v = P/RT$ is a constant. Therefore, the number of moles in the gas syringe is calculated as follows:

$$\frac{n_1}{V_1} = \frac{n_2}{V_2} \quad or \quad n_2 = n_1 \frac{V_2}{V_1} \tag{E3.4}$$

A plot of moles of toluene vs GC integrator area is constructed as shown in Figure 3.12. In order to obtain the mole fraction of toluene in the combustion gas, the following

procedure is used. The combustion gas sample in the loop is present at a known volume, temperature, and pressure. The total moles of gas can be calculated from the ideal gas law. The moles of toluene in the sample are determined by taking the GC integrator area and using Figure 3.12. The toluene mole fraction is then simply the ratio of moles of toluene to the total moles of the gas sample. Similarly, gas injections of benzene were also performed because it was detected on occasion in the soot laden gas stream at equivalence ratios (ϕ) > 1.5.

A GC temperature program for the Poropak Q column was used starting at 50 °C for 3 minutes and then ramped at 25 °C/minute to 215 °C (6.6 min.) and held for 8.0 minutes at 215 °C. Carbon monoxide, CO_2, and, on occasion, C_2 hydrocarbons were detected at 50 °C, and toluene and benzene were detected at 215 °C. The lower temperature was chosen at 50 °C because the time for the GC temperature program cooldown was excessively long. Another reason for using this temperature was the good separation of the CO and CO_2 gas peaks at 50 °C. The retention times for each species separated by the packed column at a carrier gas flow rate of 30 cm^3/min during temperature programming are listed in Table 3.2.

Temperature programming was required because the GC has only one detector. The time to analyze a sample using the temperature program, as well as the time required to cool the GC back to the initial temperature, was excessively long (approximately 25 minutes).

Table 3.2 Retention Times of Compounds Detected by FID

Compounds	Formula	Time (min)
Carbon Monoxide	CO	0.70
Methane	CH_4	0.90
Carbon Dioxide	CO_2	1.30
Acetylene	C_2H_2	2.30
Ethylene	C_2H_4	2.30
Ethane	C_2H_6	3.20
Benzene	C_6H_6	11.80
Toluene	$C_6H_5CH_3$	14.80

The transfer line is purged with combustion gas for about 3-5 minutes to remove any residual compounds from the last sample gas before each new injection of sample into the packed column.

When sampling for combustion gases, the vacuum pump continuously draws gas through the transfer line and sampling loop of the six port gas sampling valve. The flow rate through the transfer line is set by adjustment of the needle valves upstream and downstream of the sampling loop. The GC temperature program is then turned on and the gas sampling valve is switched to the inject position. Identification of gases from the GC integrator output is made by comparison of known retention times with standard gases and from calibration of moles of toluene.

3.2.2 Particulate Sampling to Determine Mass Density of Toluene Soot

Filter sampling of the soot stream in the inlet and outlet catalytic reactor flow for total soot mass density (mass/volume of gas) is done in a similar manner as gas sampling.

Vacuum pump #1 draws soot laden gas through the same inlet and outlet sample ports with the flow rate metered using the rotameter as shown in Figure 3.10. In fact, gas sampling to the GC and soot filter sampling are accomplished at the same time. The soot stream in the transfer line is captured by use of particulate filters. The filtering system consists of Gelman Sciences polycarbonate 47 mm diameter in-line filter holders using 0.45 μm (pore size) metricel membrane filters. A parallel arrangement of two in-line filters for both the inlet and outlet sampling ports is used. One of the filters serves as a throw-away sample when the vacuum pump first draws soot laden gas through the sampling system. This is done to purge the sampling lines facing the direction of the soot stream. Another reason for using a discarded sample is allowing the soot to form a layer on the inside tube surface of the transfer line so that all subsequent accumulation occurs on the filter paper. After 5 minutes, the parallel in-line filter is placed in the path of flow by the upstream valve and taking the first filter off-line as shown in Figure 3.10 and 3.13.

The inlet sample line passes through a cooling column of chilled water before the gas reaches the filter paper. This column was included because of a need to cool the gas taken from the top of the elbow section where gas temperatures are over 300 °C. Type-K type thermocouples are placed in-line just prior to the particulate filters for temperature monitoring. However, experience with the sampling system indicated that cooling columns were not needed since the low flow rate of the sample gas through the transfer line sufficiently cooled the gas before it reached the filter paper. The cooling column was left on the inlet sampling line out of convenience.

Mass density is determined by knowing the weight gain of the soot collected on the filter paper, volumetric flow rate of the gas (from the rotameter), and the time of sampling as shown in the following expression:

$$mass\ density = \frac{weight\ gain\ (grams)}{gas\ flow\ rate\ (l/\text{min})\ time\ (\text{min})}$$

3.2.3 Optical Measurement of Soot Filter Paper Samples to Determine Relative Darkness Levels

Relative changes in filter darkness level were determined by laser transmission because of the difficulty in detecting changes by visual observation, or by weight gained.

Optical transmission was measured as applied voltage was varied, especially with light soot loadings. The amount of attenuated light from the laser was measured in volts. Voltage measurements were first obtained by passing the beam through a blank white filter. The beam was then passed through the circular shaped, darkened soot samples in each of the 4 quadrants of the filter paper, and an average of the reduced voltages was obtained. Percent darkness was referenced from the voltage measurement of a clean filter paper sample taken that day. This method enabled a detectable relative change in soot loading from voltage variation.

3.2.4 Particulate Sampling to Determine Size of Toluene Soot Particles

Sampling of the soot to determine particulate size is accomplished using a HIAC/ROYCO Model 1200 particle counter and Model 4100 sensor. A tee at the inlet sampling port is used as the pathway for the soot to reach the particle counter. The flow rate of the soot

sampling stream is set at 0.1 ft^3/min from the internal vacuum pump of the particle counter.

The sampling line is 1/4" stainless steel with valves to isolate the gas sampling system and allow gas and soot stream to be drawn to the particle counter as shown in Figure 3.14. The sample stream then flows through 1/4" coiled copper tubing. The excellent heat conductance of the copper tubing reduces the gas and soot stream temperature below 50 °C. A type-J thermocouple is installed just after the copper tubing for temperature monitoring. The soot laden gas stream then flows into a condensate trap to remove any water vapor. The condensate trap is a sealed, clear, 2.5" diameter plexiglass tube with a height of 11.5 inches. Condensed water vapor is removed by unscrewing a sealed cap on the bottom of the trap. The sample gas and soot stream flows into the bottom portion of the trap and exits at the top.

Six different particle diameter sizes are manually set in the counter for each sample. A calibration curve of particle size diameter as a function of output pulse voltage is provided when the machine is calibrated. The curve is supposed to be linear through the range of calibration. However, this sensor does not exhibit linearity from 0.3 μm to 0.8 μm. Therefore, particle counting in this range is unreliable. In addition, the smallest particle sensitivity of the instrument is at 0.3 μm.

Sampling time of the counter for each run is 10 minutes. A printer hooked up to the sensor prints out the number of particles counted for each set particle diameter upon completion of a run.

Another particle counting device became available after experimentation was completed. An Amherst Process Instruments (API) Aerosizer Model LD using the principle of aerodynamic time-of-flight for measuring a single particle as it passes between two laser beams was used. This instrument provides real time measurements on particle size distribution and particle counts. Particle sizes between 0.2 to 700 μm are accurately measured.

Particles passing through the laser lights scatter light which is detected and converted to electronic signals by two photomultiplier tubes. The time between the scattered light, called time of flight, is measured within a precision of 25 nanoseconds. This time of flight information is fed into the machine's computer program to convert these measurements into particle size. The program requires the operator to input a density for the particle stream being measured.

The API aerosizer consists of four major components: Sample Penetration Device, Aerosizer Sensor Unit, Vacuum Pump, and the Aerosizer Controller. The sample penetration device aerosizes the particles. The aerosizer sensor contains the optics for time-of-flight measurements. The vacuum pump provides the necessary air flows for measurements. The aerosizer controller contains the hardware and software for time-of-flight signal analysis.

Sampling time is either automatically or manually controlled. The sampling time is normally fixed once a stable particle size distribution is reached as seen on the computer monitor.

CHAPTER 4

MODELING METHODS

4.1 Introduction

A mathematical model is presented using an existing algorithm for simulating the capture of weakly charged soot particles due to electrostatic and diffusional effects in a straight tube reactor. The effect of these charged particles, when placed under the influence of an external electric field, will then be investigated. The solutions from the mathematical model will provide an explanation how the axial penetration of lightly charged particles of different sizes are affected by external electric field effects. A comparison of the predicted results with experimental data from filtered paper samples using an applied potential will be evaluated in Chapter 6.

The basis for the model begins with the governing equations presented by Chen (1978) for the deposition of charged particle penetration in cylindrical tubes, all having the same particle radius a and charge q. The model will then incorporate multiple fractions which can be used to approximate the actual size distribution. Each fraction has specific values for a_i, q_i, and D_i (diffusivity). The goal is to calculate total penetration (or deposition) along the tube length by modeling the transport to the wall of charged particles of different sizes flowing through the reactor at varying operating conditions. Finally, the governing equations will be modified to include the application of a specified voltage across a central wire and the surrounding reactor tube. These predictions will be compared to experimental data in Chapter 6.

4.2 Description of the Governing Equations

4.2.1 One Particle Size and Charge (No Applied Voltage)

A description of the governing equations will start with the simple case used by Chen (1978) for particles of radius a. Chen assumed the particles had acquired a uniform electrostatic charge q, prior to entering a cylindrical tube. Two coupled equations are used in the model. The first describes the field due to the presence of the charged particles. The second is the particle transport equation. Particle density ρ (# particles/volume) is specified instead of mass as used by Chen.

A cylindrical coordinate system is used, in which the z-axis is along the center of the tube.

Poisson's equation:

$$\nabla \cdot \boldsymbol{E} = \frac{\rho q}{\varepsilon_o} \tag{E4.1}$$

where $\boldsymbol{E}$ = Electrostatic field of a particle (Volts/m), ρ = particle density (#/m^3), q = particle charge (coulomb), ε_o = permittivity of free space (8.85 x 10^{-12} C^2/N m^2).

Assuming negligible E field effects in the axial direction the equation reduces to:

$$\frac{1}{r}\frac{\partial(re_r)}{\partial r} = \frac{\rho q}{\varepsilon_o} \tag{E4.2}$$

where e_r is the radial component of the electric field.

The transport equation consisting of convective, diffusive, and electrostatic fluxes for uniform particles of radius a and charge q is:

$$u\frac{\partial \rho}{\partial z} = D\frac{1}{r}\frac{\partial}{\partial r}\left(r\frac{\partial \rho}{\partial r}\right) - \frac{1}{r}\left(\frac{q}{6\pi\mu a}\right)\frac{\partial(r\rho e_r)}{\partial r} \tag{E4.3}$$

The convective flux results from the bulk flow u. Particle diffusion is driven by a particle concentration, or number density gradient. The electrostatic flux results from a coulombic attraction as the charged particles move to the elctrically grounded wall. The viscosity of the fluid in the electrostatic flux term is shown as μ.

The boundary conditions are:

$\left.\frac{\partial V}{\partial r}\right|_{r=0} = 0$ (symmetry at the axis)

$\left.\frac{\partial \rho}{\partial r}\right|_{r=0} = 0$ (for $z > 0$, symmetry at the axis)

$\left.V\right|_{r=1} = 0$ (at the electrically grounded wall)

$\left.\rho\right|_{r=1} = 0$ (particle density at the wall is zero)

The assumption used in the last boundary condition is that soot particles stick to the wall. A steep radial gradient exits at the wall interface such that the particle density goes to zero.

Initial conditions for the governing equations are:

$\left.\rho\right|_{z=0} = 1$ (at tube inlet, assuming an initial uniform particle density)

$V = \frac{1}{4}\alpha\left(1 - r^2\right)$ (derived initial condition for the potential at the tube inlet)

The second initial condition is determined by integrating the Poisson equation (E4.2) assuming the initial particle density is uniform, or $\rho = 1$. The derivation is shown in Appendix D.1.

A control volume analysis is used to derive the transport equation. The complete derivation of the transport equation is found in Appendix D.1 The equations in dimensionless form using Chen's dimensionless parameters are below:

Poisson's equation in potential form ($e_r = -\partial V/\partial r$) is:

$$\frac{1}{r}\frac{\partial}{\partial r}\left(r\frac{\partial V}{\partial r}\right) = -\alpha\rho \qquad \text{(E4.4)}$$

where α , the dimensionless charge parameter, equals $\frac{\rho_o q^2 r_o^2}{6\pi\mu a D\varepsilon_o}$

The dimensionless transport equation in the potential form is:

$$u\frac{\partial\rho}{\partial z} = \frac{1}{r}\frac{\partial}{\partial r}\left(r\frac{\partial\rho}{\partial r}\right) + \frac{1}{r}\frac{\partial}{\partial r}\left(r\rho\frac{\partial V}{\partial r}\right) \qquad \text{(E4.5)}$$

The following dimensionless terms are used:

$$\rho \equiv \frac{\rho}{\rho_o} \Rightarrow \rho \equiv \rho\rho_o \qquad V \equiv \frac{qV}{6\pi\mu aD} \Rightarrow V \equiv V\frac{6\pi\mu aD}{q}$$

$$r \equiv \frac{r}{r_o} \Rightarrow r \equiv r r_o$$

$$z \equiv \frac{zD}{r_o^2 u_o} \Rightarrow z \equiv \frac{z r_o^2 u_o}{D}$$

$$u \equiv \frac{u}{u_o} \Rightarrow u \equiv u\, u_o$$

where: r_o = inside tube radius, ρ_o = initial particle density

Chen (1978) varied α as a parameter and evaluated its effect on deposition as a function of dimensionless distance for both plug and laminar flow. We examined these results in a more general setting below.

4.2.2 Different Size Particles, Charges, and Diffusivities (No Applied Voltage)

For the case of flow with different size particles, charges, diffusivities, and particle electrostatic effects, the modified form of (E4.3) for particle *i* in the absence of an applied voltage is:

$$u\frac{\partial\rho_i}{\partial z} = D_i\frac{1}{r}\frac{\partial}{\partial r}\left(r\frac{\partial\rho_i}{\partial r}\right) - \frac{1}{r}\left(\frac{q_i}{6\pi\mu a_i}\right)\frac{\partial\left(r\rho_i e_r\right)}{\partial r} \qquad \text{(E4.6)}$$

The same boundary conditions apply as given in section 4.2.1.

Rewriting (E4.6) in terms of V by using the relation $e = -\partial V/\partial r$, the equation becomes:

$$u\frac{\partial \rho_i}{\partial z} = D_i\frac{1}{r}\frac{\partial}{\partial r}\left(r\frac{\partial \rho_i}{\partial r}\right) + \frac{1}{r}\left(\frac{q_i}{6\pi\mu a_i}\right)\frac{\partial}{\partial r}\left(r\rho_i\frac{\partial V}{\partial r}\right) \qquad \text{(E4.7)}$$

Nondimensionalizing (E4.7) as similarly done in section 4.2.1:

$$\rho_i = \frac{\rho_i}{\rho_{tot}} \Rightarrow \rho_i = \rho_i\rho_{tot} \qquad V = \frac{q_{ref}V}{6\pi\mu a_{ref}D_{ref}} \Rightarrow V = V\frac{6\pi\mu a_{ref}D_{ref}}{q_{ref}}$$

$$r = \frac{r}{r_o} \Rightarrow r = r\,r_o$$

$$z \equiv \frac{zD_{ref}}{r_o^2u_o} \Rightarrow z \equiv \frac{zr_o^2u_o}{D_{ref}}$$

$$u = \frac{u}{u_o} \Rightarrow u = u\,u_o$$

The transport equation for particle i becomes:

$$(\delta_i)u\frac{\partial \rho_i}{\partial z} = \frac{1}{r}\frac{\partial}{\partial r}\left(r\frac{\partial \rho_i}{\partial r}\right) + (\delta_i)(\eta_i)\frac{1}{r}\frac{\partial}{\partial r}\left(r\rho_i\frac{\partial V}{\partial r}\right) \qquad \text{(E4.8)}$$

where: $\delta_i = \frac{D_{ref}}{D_i}$ $\qquad \eta_i = \left(\frac{q_i}{q_{ref}}\right)\left(\frac{a_{ref}}{a_i}\right)$ $\qquad \gamma_i = \frac{q_i}{q_{ref}}$

where a_{ref}, q_{ref}, and D_{ref} represent the reference values. The total initial particle density (# particles/unit volume) is ρ_{tot}. For a particle distribution of i = 1, 2, ····, n fractions, there are n dimensionless transport equations that are needed.

The Poisson equation for particle i is:

$$\frac{1}{r}\frac{\partial}{\partial r}\left(r\frac{\partial V}{\partial r}\right) = -\sum_{i=1}^{n}\frac{\rho_i q_i}{\varepsilon_o} \qquad \text{(E4.9)}$$

Using dimensionless parameters and rearranging terms, the Poisson equation with all fractions becomes:

$$\frac{1}{r}\frac{\partial}{\partial r}\left(r\frac{\partial V}{\partial r}\right) = -\alpha_o\sum_{i=1}^{n}\gamma_i\rho_i \qquad \text{(E4.10)}$$

where the modified dimensionless charge parameter alpha (α_o) is a constant given by:

$$\alpha_o = \left(\frac{r_o^2 q_{ref}^2 \rho_{tot}}{6\pi\mu a_{ref} D_{ref} \varepsilon_o} \right)$$

Equation (E4.10) is a single equation of the space charge from summing the contributions over all of the particle size fractions. The detailed derivations of the above equations are contained in Appendix D.2.

Thus, equations (E4.8) and (E4.10) are the partial differential equations for a multiple particle size fraction of particles *i* acting under their own electrostatic field. The solution to these equations are discussed below.

Of practical importance is an overall expression for total particle penetration or deposition. Penetration of particle *i*, $P_i(z)$, is determined by integrating the particle density *i* at any axial distance *z* from the centerline to the tube radius *R* (same as r_o shown above), divided by the initial particle density *i*. If a central wire is present, the lower limit of integration would be r_i, instead of zero. If $\rho_i(r,0) = \rho_{i,o}$, then $P_i(z)$ is expressed as:

$$P_i(z) = \frac{\int_0^R 2\pi\rho_i(r,z) r dr}{\int_0^R 2\pi\rho_i(r,0) r dr} \qquad \text{(E4.11)}$$

$$P_i(z) = \frac{\int_0^R \rho_i(r,z) r dr}{\frac{1}{2}\rho_{i,o} R^2} \qquad \text{(E4.12)}$$

The dimensionless parameter is used: $\boldsymbol{r} = \frac{r}{R}$; *and* $\rho_i = \frac{\rho_i}{\rho_{tot}}$

Inserting this dimensionless parameter into (E4.12), dimensionless $P_i(z)$ becomes:

$$P_i(z) = \frac{\int_0^1 \rho_i \rho_{tot} r R dr R}{\frac{1}{2}\rho_{i,o} R^2} = 2\left(\frac{\rho_{tot}}{\rho_{i,o}}\right)\int_0^1 \rho_i r dr \qquad \text{(E4.13)}$$

We now define f_i as the ratio of the initial fraction of particle density i to the total particle density of all sizes: $f_i = \frac{\rho_{i,o}}{\rho_{tot}}$

Penetration for particle i now becomes:

$$P_i(z) = \frac{2}{f_i}\int_0^1 \rho_i r dr \qquad \text{(E4.14)}$$

One method for determining total penetration of all particles is the use of a volume weighted average of fraction i. The volume of particles in fraction i at any position z is the integral of particle density times its particle volume. Volume $V_i(z)$ is expressed as:

$$V_i(z) = \left[2\pi\int_0^R \rho_i(r,z) r dr\right]\left(\frac{4}{3}\pi a_i^3\right) \qquad \text{(E4.15)}$$

Using the same dimensionless parameters as shown earlier the total volume of particles, $V(z)$, at z becomes:

$$V(z) = 2\left(\frac{4}{3}\pi^2 R^2\right)\rho_{tot}\sum_{i=1}^{n} a_i^3 \int_0^1 \rho_i r dr \qquad \text{(E4.16)}$$

In a similar fashion, the derivation of initial total volume of particles, V(0), at $z = 0$ using nondimensional analysis can be shown as:

$$V(0) = \left(\frac{4}{3}\pi^2 R^2\right)\rho_{tot}\sum_{i=1}^{n} f_i a_i^3 \qquad \text{(E4.17)}$$

By taking the ratio of the total particle volume at any point z over the total particle volume at $z = 0$, the fraction is essentially a "volume penetration" or P_{tot}. The total penetration P_{tot}, after some rearrangement and simplification, results in the following expression:

$$P_{tot} = \frac{\sum_{i=1}^{n} \left\{ f_i a_i^3 P_i(z) \right\}}{\sum_{i=1}^{n} f_i a_i^3} \qquad \text{(E4.18)}$$

Total deposition is 1 - P_{tot}. The complete derivation is shown in Appendix D.2.

A number based particle penetration is likewise determined by summing each product of $P_i(z)$ and its corresponding fraction f_i. Therefore, P_{tot} for particle penetration is:

$$P_{tot} = \sum_{i=1}^{n} f_i P_i(z) \qquad \text{(E4.19)}$$

4.2.3 Different Size Particles and Charges Acting Under an Applied Voltage

When an external field is applied in a cylindrical tube using a central wire along the axial direction, the electric field (e_r), is in the form of $V_o/(rln(r_o/r_i))$ (Bohm, 1982). Here r_o is the tube radius and r_i is the central wire radius.

The electrostatic flux due to the space charge of the particles, however, is still present. The total electric field in the radial direction now consists of two components. The first is due to the particles themselves, while the second is from an external applied field. The electric field created by the particle space charge is derived by integrating the Poisson equation (E4.2). It is equal to $\rho qr/\varepsilon_o$, a linear function of r. The second component is $V_o/(rln(r_o/r_i))$. As the applied voltage (V_o) is increased, e_r (from applied field) tends to dominate. Thus, we tend to ignore the first component when an external field is present.

Substituting $e_r = V_o/(rln(r_o/r_i))$ into the particle transport equation (E4.3), we obtain:

$$u\frac{\partial \rho}{\partial z} = D\frac{1}{r}\frac{\partial}{\partial r}\left(r\frac{\partial \rho}{\partial r}\right) - \frac{1}{r}\left(\frac{q}{6\pi\mu a}\right)\frac{\partial}{\partial r}\left(r\rho\frac{V_o}{\ln\left(r_o/r_i\right)}\frac{1}{r}\right) \tag{E4.20}$$

which reduces to:

$$u\frac{\partial \rho}{\partial z} = D\frac{1}{r}\frac{\partial}{\partial r}\left(r\frac{\partial \rho}{\partial r}\right) - \left(\frac{qV_o}{6\pi\mu a ln\left(r_o/r_i\right)}\right)\frac{1}{r}\frac{\partial \rho}{\partial r} \tag{E4.21}$$

The first term on the right hand side (diffusional flux) formally makes the PDE parabolic. As V_o increases, the second term dominates. For high V_o, solutions develop which are like those obtained when the diffusional term is dropped, i.e., ones in which a steep radial gradient moves from r_i to r_o as z increases. As a consequence, these solutions cannot be well approximated on a fixed radial grid. Adaptive gridding techniques are required in such cases. Indeed, the diffusional term is only important in the vicinity of the steep gradients at which position, diffusion would act to smooth them out to some degree. Nonetheless, on an integrated basis such as that used to determine penetration, eliminating the diffusional flux at high applied field should have little effect.

Therefore, equation (E4.21) reduces to:

$$u\frac{\partial \rho}{\partial z} = -\left(\frac{qV_o}{6\pi\mu a ln\left(r_o/r_i\right)}\right)\frac{1}{r}\frac{\partial \rho}{\partial r} \tag{E4.22}$$

Using the nondimensional parameters in Section 4.2.1, including $z = z/L$, (E4.22) becomes:

$$u\frac{\partial \rho}{\partial z} + \beta\frac{1}{r}\frac{\partial \rho}{\partial r} = 0 \tag{E4.23}$$

where the dimensionless parameter $\beta = \dfrac{qV_oL}{6\pi\mu a \ln\frac{r_o}{r_i}u_o r_o^2}$

The derivation for (E4.23) is contained in Appendix D.3.

The dimensionless velocity u is a function of r. If a dimensionless parabolic expression $(1 - r^2)$ for laminar flow is used, the PDE is rearranged as:

$$\frac{\partial \rho}{\partial z} + \beta \frac{1}{r(1-r^2)} \frac{\partial \rho}{\partial r} = 0 \qquad \text{(E4.24)}$$

The solution to this PDE is in the form of:

$$\rho(z,r) = g\left(\frac{r^2}{2} - \frac{r^4}{4} - \beta z\right) \qquad \text{(E4.25)}$$

where $g(\cdot)$ is an arbitrary function. This expression, (E4.25), is essentially a family of characteristic curves such that $\frac{r^2}{2} - \frac{r^4}{4} - \beta z = constant$. Alternately, multiplying the equation through by 4 gives $2r^2 - r^4 - 4\beta z = const.$ From this equation, an expression for density, $\rho(r,z)$, can be derived on any point r, z lying on a characteristic curve (see Appendix D.3). The density at any point along these characteristic curves is:

$$\rho(r,z) = \rho_{init}\left(\left[1 - \sqrt{(1-r^2)^2 + 4\beta z}\right]\right) \qquad \text{(E4.26)}$$

The number penetration is derived through integration (see Appendix D.3). Noting that $r_i \cong 0$ in $(1 - r_i^2)$, the penetration along the dimensionless distance z is:

$$P(z) = \sqrt{1 - 4\beta z} \qquad \text{(E4.27)}$$

For a more general case using a multiple particle sizes along the dimensionless distance z, the number penetration is:

$$P_i(z) = f_i\sqrt{1 - 4\beta_i z} \quad for\ z \le \frac{1}{4\beta_i} \qquad \text{(E4.28)}$$

The term f_i is defined as the initial fraction of particle i or $\rho_{i,o}/\rho_{tot}$.

The total penetration or P_{tot} is:

$$P_{tot} = \sum_{i=1}^{n} P_i(z) \qquad \text{(E4.29)}$$

Volume penetration for multiple size particles is performed in a similar manner as (E4.11 through 17). The resulting expression for volume penetration is:

$$P_{tot} = \frac{\sum_{i=1}^{n} f_i a_i^3 \sqrt{1 - 4\beta_i z}}{\sum_{i=1}^{n} f_i a_i^3} \qquad \text{(E4.30)}$$

The complete derivation for the above equations is found in Appendix D.3.

Hinds (1982), using laminar flow theory, derived an expression for collection efficiency for tube length L:

$$\eta = \frac{2\pi ZVL}{Q \ln\left(r_o / r_i\right)} \qquad \text{(E4.31)}$$

where Z is the electrical mobility of the particles, $Z = \frac{qC_c}{6\pi\mu a}$, and C_c is the Cunningham correction factor.

C_c is used to correct for noncontinuum effects when particles diameters are so small they approach the same order as the mean free path of the suspending fluid. When particle diameters are ≥ 1 μm, C_c approaches one. Q is volumetric flow rate ($u_o \pi r_o^2$). When $Z = \frac{qC_c}{6\pi\mu a}$ is put back into (E4.31) the expression is exactly defined as β in (E4.23). β is typically small in these applications. If penetration is used instead of collection efficiency (E4.31) becomes 1 - 2β. If 1 - 2β is squared, and its square root is taken:

$$\sqrt{\left(1 - 2\beta\right)^2} = \sqrt{1 - 4\beta + 4\beta^2} \cong 1 - 2\beta$$

Therefore, the equation (E4.31) used by Hinds is the same as (E4.27) for $z = 1$ (reactor tube exit).

4.3 Mathematical Models

4.3.1 Description of the Mathematical Program for a Charged Particle Size Distribution in the Absence of an Applied Voltage

A model to predict the deposition of particles onto an inner tube surface acting under its diffusional and electrostatic field effects was run using an existing algorithm called Chebyshev Polynomial Software for Elliptic-Parabolic systems of PDEs (PDECHEB) developed by Berzins and Dew (1991). PDECHEB uses Chebyshev polynomials to approximate a continuous solution of the PDE between each pair of spatial breakpoints. The algorithm was chosen because the governing equations were compatible with the form of the software, and because it can handle the system of partial differential equations which result from considering multiple size fractions.

The system of partial differential equations (PDEs) consisting of the particle transport equations and Poisson's equation for the electric field potential has been solved using PDECHEB, a package solved by Berzins and Dew (1991) for the numerical solution of parabolic-elliptic systems. It is a high quality code which has undergone extensive testing on a full range of sample problems.

This software automatically discretizes a spatial variable to give a system of ordinary differential equations. In this application, the radial variable r, is discretized and the resulting system integrated with respect to the "time-like" variable z, the axial distance along the reactor length. The discretization is accomplished using a piecewise polynomial approximate of the form $\sum a_i(z)T_i(r)$, where $T_i(\cdot)$ is the Chebyshev polynomial of the first kind of degree i. In the derivation of the algorithm, this approximant is substituted into the partial differential equations and the resulting relations are required to hold at a set of

points which are the roots of the approximate Chebyshev polynomial. The software, thus, achieves spatial discretization by the method of orthogonal collocation. When combined with the boundary conditions, the resulting system consists of both differential and algebraic equations. The widely used differential algebraic system solver DASSL (Brenan et al., 1989) was employed for the z integration.

In order to use this software, it was necessary to code a driver in FORTRAN which initializes PDECHEB and repeatedly calls DASSL to integrate with respect to z. The system of PDEs and the boundary and initial conditions are specified by writing three subroutines in the required PDECHEB format. Values for the operating parameters (e.g. gas velocity, reactor length, particle size) are read from a user-supplied input file. The output consists of the radial profiles of particle density and electric field potential at the indicated value of z.

4.3.2 Mathematical Model for a Multiple Particle Fraction in the Presence of an Applied Voltage

When there is an applied voltage, the applicable equation is (E4.23). The solutions for number and volume penetration of different size particles are defined in (E4.29) and (4.30).

A FORTRAN 77 program was written using the above equations to solve for the penetration of each fraction i, as well as total penetration, at each incremental distance z. The input file, source code, is found in Appendix E and F. Sample output is shown in Appendix G.

One important factor to remember is that the model is designed for particles ≥ 1 μm. The charge acquired by these size particles is primarily by field charging. As the particles pass through an ion charged applied field, a theoretical saturation charge can be determined.

The saturation charge (Flagan and Seinfeld, 1988) of a particle ≥ 1 μm is approximated by:

$$q_{sat} \cong 3\pi\varepsilon_o E D_p^2 \qquad \text{(E4.32)}$$

where: $E = V_o/(r\ln(r_o/r_i))$, D_p = particle diameter

CHAPTER 5

DESIGN CHANGE MILESTONES IN THE EXPERIMENTAL APPARATUS LEADING TO FINAL DESIGN FOR QUALITY EXPERIMENTATION

5.1 Introduction

Much of the effort spent to meet the objectives in this dissertation was directed toward a feasible design, construction, testing out individual components and subsystems, and then testing the entire system. This chapter is devoted to describing the evolution of design changes from initial concept to a properly working experimental system.

5.1.1 Initial Construction of the Experimental Apparatus

Once an initial combustor design was found, engineering drawings were made and machining of the combustor , cooling, and elbow sections commenced. The reactor tube design followed, and was then built. Much of the design was driven by available and donated equipment and material, as well as purchased equipment. The ancillary systems shown in Figures 1.2, 1.3, and 3.1 of Appendix A were sized, built, and mounted onto the test bench once the machined sections were in place. Considerable time was spent building the gas sampling and soot filter paper system, and the air and fuel delivery arrangement to their present configurations.

5.1.2 Design Changes Once the Experimental Apparatus was Built

Testing of the combustor section commenced upon completing construction of the entire system. Initial runs of the combustor indicated several needed design changes in order to produce a steady and reliable soot stream. The nozzle that was initially used had a much wider spray angle and merely soaked the refractory lining with toluene. The swirl and dilution air could not keep the flame centered in the confined space of the combustor. The inside diameter of the combustor region was approximately 1.75". The spray angle and small inside diameter caused the flame to be pushed out of the combustor section and caused excessive sooting for the air and fuel flow mixture. In addition, the spray nozzle was positioned about 1" forward of the swirl air vanes. These design flaws caused the flame to extend out of the combustor region by at least 12". The nozzle was initially placed further forward of the swirl vanes because it was thought that the ignitor terminal leads would not survive the heat. At that time no consideration about the combustor flame was given. The ignitor became positioned behind the spray nozzle once it was moved slightly forward of the swirl vanes. Dilution air helped push the ignitor flame toward the spray nozzle for ease in starting up the combustor. When the nozzle was pushed back closer to the swirl vanes, the ignitor was back in front of the spray nozzle. Unfortunately, the nozzle spray angle was such that the fuel mist sprayed into the ignitor penetration and soaked the refractory material facing the combustor housing. This caused a small secondary flame in the small air gap between the refractory material and the combustor housing. The combustor flame also burned the ignitor leads.

Fortunately, the problems wee solved through minor redesigns and changes by machining and use of different parts. The spray nozzle was moved back closer to the swirl vanes. The combustor inside diameter was increased to 2.0". A nozzle with a 45° angle, 0.40 gph (25.2 ml/min at 100 psig), and hollow point spray pattern was installed. A redesign and relocation of the ignitor (see Figure 3.4a of Appendix A) was completed. Further testing showed that the flame still extended about 5" from the combustor. Adjustments with the swirl and dilution mixtures showed that swirl air alone confined the flame region close to the nozzle. The absence of dilution air resulted in intense flame radiation back on the nozzle itself and swirled burner assembly. As a result of the heat, nozzle lifetime was significantly reduced and replacement was necessary after a few hours of running time. In addition, it was necessary to use chilled water flowing through coiled 1/4" copper tubing around the swirled burner assembly and over 50% of the combustor section to prevent overheating. Another refinement included matching inside diameters throughout the swirled burner assembly, combustor, cooling section, and elbow section for smoother flow.

Successive runs of the combustor showed that a light to moderate soot stream was achieved at an equivalence ratio (ϕ) between 1.3 and 1.4. At this time all of the exhaust stream from the combustor went through the catalytic reactor tube before exiting. Therefore, the reactor residence time was dependent on ϕ, gas temperature, and the amount of liquid nitrogen needed to cool the gas stream. The gas velocity exiting the reactor tube was approximately 9-11 m/s. The literature (Masuda et al., 1983) suggested gas velocities above 1.0 m/s result in a rapid drop in collection efficiency using

electrostatic particle capture only. However, several runs using a blank stainless steel tube and the electrostatic precipitator were performed. Filter paper samples indicated some agglomeration of soot particles at around -3.0 kV and up. At -4.0 kV, the amount of agglomerated soot particles continued to increase. This observation appears to be similar with previous studies by Kittelson et al. (1991) and Thimsen et al. (1990) who used an electrostatic agglomerator. Keeping the agglomerated soot on the filter was difficult during removal from the in-line holder. This occurred because the agglomerated soot maintained a residual charge and usually jumped at the slightest jolt to the inside surface of the polycarbonate in-line holder. Since gas velocity was too high for electrostatic particle capture at the wall, the agglomerated particles were readily picked up on the filter paper samples at the reactor tube exit. The majority of the agglomerated soot simply did not adhere to the blank tube surface and was swept away by the high gas flow rate.

The same experiment with the blank tube was repeated with a positive voltage applied to the central wire. The results were very similar to the previous run, but it appeared that the agglomerated soot was slightly larger and somewhat more numerous. This evidence again was consistent with previous studies by Kittelson et al. (1986, 1991), and Thimsen et al. (1990) who stated that diesel soot is bi-polar charged, and that the soot agglomerated under the influence of an externally applied electrostatic field. Bohm (1982) noted that carbon is neither electro-positive nor electro-negative. This may explain why soot agglomeration occurs from an applied field of either polarity. No further experiments were performed with a positive polarity voltage.

To ensure that soot was actually collected on the filter paper, samples were observed under an electron microscope at 500 X and 1000 X magnification. Soot particles of sizes 10 μm or less were indeed deposited on the filter paper as shown in Figure 5.1 of Appendix A. A clean filter paper is compared with a sample of light soot loading shown in Figure 5.2.

5.1.3 Follow On Changes Leading to Final Arrangement of Experimental Setup

In order to slow down the gas flow through the reactor tube and increase reactor residence time, a 1.875" i.d. bypass tube was machined and welded into the elbow section so that most all of the combustion gases were exhausted. An orifice was installed in the bypass line in order to provide some flow restriction so that some of the stream would go up the catalytic reactor tube. Several runs using various size orifices indicated that an orifice diameter of 1.80" in the 1.875" i.d. bypass tube provided a small flow to the catalytic reactor tube at typical operating conditions. The bypass tube also allowed the combustor to exhaust freely with no backpressure acting on the flame region. In the prior design, the sudden decreased flow area between the elbow and the reactor tube entrance was so excessive that it caused disruptions in the flow pattern and a backpressure. In addition, heavy soot buildup in the cooling and elbow sections were a common occurrence prior to the elbow design change.

Pure, metered oxygen flow was relocated from the bottom of the elbow section to the top portion where the gas flow was angled up into the reactor tube. This change was significant because without supplemental oxygen, very little catalytic oxidation was

occurring on the catalyst surface. The oxygen concentration in the combustion gases was approximately 2.5-3.5% by volume. Air was originally mixed with the SOF flow in the elbow, but it was discovered that the oxygen concentration was so diluted in the soot stream. Thus, the metered pure oxygen was used and relocated closer to the reactor tube inlet. The O_2 flow was angled up into the reactor tube, resulting in an oxygen rich gas stream. In addition, this angled oxygen flow injection helped direct the soot laden gas stream upward in a controlled way through the catalytic reactor tube. Velocity measurements of the gas stream exiting the reactor tube were made using an anemometer. A parallel line for nitrogen gas injection was also added. The N_2 served as a baseline prior to O_2 injection.

Another advantage in using the bypass tube was that reactor residence time was now no longer dependent on the equivalence ratio and the amount of liquid nitrogen needed to cool the exhaust stream. Since most all of the exhaust soot stream exits through the bypass, the remaining flow up through the reactor tube doesn't change significantly. Gas velocity flowing through the catalytic reactor tube is now controlled by the following parameters: (1). orifice diameter in the bypass line, (2). the flow rate of O_2 or N_2 at the reactor tube inlet, (3). and tube furnace temperatures.

The liquid nitrogen injection point was moved from the elbow section to near the exit of the combustor cooling section. This location was better because the liquid N_2 sprayed into a smaller flow area and resulted in better temperature control.

Continued testing of the combustor indicated some nagging problems with the flame length and complete combustion of the atomized toluene mist. The nozzle was

finally changed to a 30° angle, 0.40 gph (25.2 ml/min at 100 psig), and solid spray pattern. A stable, swirling flame located near the nozzle produced a gold colored, cone-like plume that exited the combustor section.

The electrostatic precipitator experienced short circuiting problems during this time period. Soot buildup on the wire support bars caused electric shorts and arcing to develop as the voltage on the central wire was increased. The cutout area where the support bars rested on the reactor tube flanges was increased by machining to prevent the bars from touching the flanges. Insulating material (zirconia felt) was placed so that the support bars were insulated from the flanges. In addition, the ceramic tube inserts that insulated the wire from the support bar were lengthened to prevented arcing between the wire and support bar at higher voltages. Another enhancement in the electrostatic precipitator was increasing the wire diameter from 0.0201" to 0.060". A straight, stiff stainless steel wire rod supported on both ends resulted in better centering of the wire.

Subsequent runs did not completely eliminate the short circuiting problems at higher voltages. It was discovered that the support bars holding the central wire in place built up a significant layer of soot and contributed to short circuiting. In addition, the originally designed support bars hindered flow gas flow at the reactor tube entrance. The bars were rectangular in shape and blocked the gas flow across the 0.75" i.d. rolled sheet of catalyst material. A redesign by necking down the width between the center hole and ends to 0.0625" (see Figure 3.8 of Appendix A) left a smaller exposed surface area for soot deposition, as well as a greater flow area at the reactor tube entrance. As a final

means of reducing short circuiting, removable insulating "shoes" were made from hardened alumina and fitted between the support bar ends and the reactor tube flanges.

One final change to the experimental apparatus was to allow for an increased combustor running time. A large 3.5 liter tank was installed in place of the 2.2 liter flask. Maximum combustor running time increased from 2 - 2.5 hours to about 3.5 hours. However, in order to obtain a full set of voltage variation from 0 to -5.0 kV in a given experiment, the 2.2 liter tank was re-installed in a parallel arrangement with the 3.5 liter tank. Once the large tank begins to empty, the smaller tank is put on-line. The fuel level in both tanks equalizes and maximum running time increases between 5.5 and 6.0 hours.

As a result of these design changes, the final arrangement in the experimental apparatus was now complete. The experiments were now directed to taking quality data for analysis.

CHAPTER 6

RESULTS AND DISCUSSION

6.1 Operating Conditions of the System

The dilute swirled combustor was normally operated to produce a light to moderate soot stream so that the reactor tube exit filter paper samples for a given gas flow rate did not completely blacken the filter paper. This was done in order to reproduce similar sooting conditions for gas and filter paper sampling analysis. Inlet gas temperature flowing into the catalytic reactor, as well as catalyst surface temperatures, were maintained at approximately the same conditions for each experimental run.

The combustor was operated at ϕ between 1.3 and 1.4, with a fuel flow rate of 20-22 cm^3/min at 110-120 psig as measured at the toluene rotameter outlet. Slight variations in swirl air to fuel flow rate existed between each experimental run because it was difficult to reproduce the same sooting conditions using a measured fuel flow rate as a guide. Part of this problem was due to slight variations in measured fuel flow rate at the operating pressure that sometimes occurred with each new nozzle. These small differences were discovered when measuring the nozzle flow rate at operating pressure and room temperature prior to combustor start-up. Because of the short life of the nozzle at operating conditions, a new nozzle was installed before each experimental run. The important consideration with respect to the combustor was adjusting the air and fuel flow

rates in order to reproduce a similar exhaust soot stream density, and near consistent CO and CO_2 levels.

Since most of the combustion gas exited through the bypass, the small flow through the reactor tube was easily controlled by the orifice in the bypass tube and with the use of oxygen. Metered nitrogen gas flowing through the reactor was first used so that baseline steady state catalyst monolith temperatures were recorded. No catalytic oxidation was expected when a large amount of nitrogen gas was present. Previous O_2 measurements indicated that the combustion gas contained 2.5-3.5% by volume oxygen. The nitrogen flow further diluted this oxygen. Pure, metered oxygen was then introduced. The O_2 flowing through an inlet angled toward the catalytic reactor tube inlet (as described in Chapter 5, section 5.1.3) provided a controlled flow stream and well as diluting both gas and soot concentrations. The approximate O_2 concentration (mole fraction) after being introduced into the reactor was 0.453. The temperature controllers in the three zone tube furnace were set so that the catalyst surface temperatures were near 400 °C at operating conditions. Gas stream flow for the experimental runs remained in the laminar regime with the Reynolds number approximately 1000.

6.2 Experimental Results

6.2.1 Voltage Variation in the Catalytic Reactor Tube

The experimental set-up in the catalytic reactor tube section was set up with the following conditions as listed in Table 6.1 and 6.2.

Table 6.1 Experimental Set-up in the Catalytic Reactor with Tube Furnace Controllers Set for Lower Catalyst Surface Temperatures

---

Run Dates: 2/20/97, 3/7/97, 3/14/97
Conditions: Catalyst material and center wire inside of reactor tube
Pure O_2 gas flowing at 7.03 liters/min at 5 psig into reactor tube
Temperature controllers in tube furnace set at:

#1 (top):	445 °C
#2 (middle):	475 °C
#3 (bottom):	475 °C

Voltage variation: 0 up to -5.0 kV in 500 volt increments, except 2/20/97
Inlet reactor tube gas stream temperature: 370 °C

Sooting Conditions:

Light:	2/20/97, 3/7/97
Heavy:	3/14/97

Table 6.2 Experimental Set-up in the Catalytic Reactor with Tube Furnace Controllers Set for Higher Catalyst Surface Temperatures

---

Run Dates: 3/18/97, 4/1/97
Conditions: Catalyst material and center wire inside of reactor tube
Pure O_2 gas flowing at 9.21 liters/min at 5 psig into reactor tube
Temperature controllers in tube furnace set at:

#1 (top):	490 °C
#2 (middle):	520 °C
#3 (bottom):	520 °C

Voltage variation: 0 up to -5.0 kV in 500 volt increments
Inlet reactor tube gas stream temperature: 370 °C
Sooting Conditions:

Light:	3/18/97
Moderate to Heavy:	4/1/97

Voltage variation throughout all experimental runs began at a condition of no applied field. The DC potential was then increased in 500 volt increments. The reason for this procedure was to begin with a clean catalyst, and then gradually increase soot deposition to the wall so that catalyst activity would remain fairly high.

As shown in Figures 6.1 through 6.5, the filter paper soot samples showed that little deposition occurred at voltages less than -3.0 kV. This occurrence may be explained by the strength of the electric field and by the nature of the particle size and charge distribution. The electric field strength closest to the center wire decreases proportionally by $1/r$ (Bohm, 1982) as r increases. Lightly charged particles near the wire are more likely to be deflected toward the wall than particle sizes located further away. These deflected particles probably collide with unaffected particulates and most never make it to the wall. Instead, these charged particles are swept out of the reactor tube along with most of the soot. A transition region between -3.5 to -4.0 kV appears to exist where detectable changes in soot deposited may or may not be observed depending on the soot concentration. In light sooting conditions, a slight decrease in darkness on the outlet filter paper was noted at -3.5 kV, whereas, no change was seen in the heavy soot data. Specks of agglomerated soot began to appear on the filter paper at voltages of -3.0 to -3.5 kV, and increased in number at -4.0 through -5.0 kV. The DC power supply was not increased above -5.0 kV due to arcing occurring inside the catalytic reactor tube.

As the DC voltage was increased to -4.0 kV, a noticeable decrease in soot collected on the filter paper was observed for both light and heavy soot conditions. The decrease was more significant at -4.5 and -5.0 kV. The applied field strength was now

sufficiently strong to entrain a large portion of the soot particles to the wall, resulting in the lighter soot loading on the filter paper.

Figures 6.6 and 6.7 are plots of darkness levels of outlet filter paper samples (raw data) as a function of applied voltage. The data for light sooting conditions (Figure 6.6) shows a gradual downward trend. On the other hand, the data for heavy sooting conditions shows a much different trend. The trend for data taken on 3/14/97 (heavy sooting) starts out flat and begins to drop after -3.0 kV. The data for 4/1/97 (moderate sooting) shows an increase in darkness up to -3.0 kV and then goes down. This increase was due to a slowly changing condition in the combustor flame which started off producing light to moderate soot and drifted toward a heavier sooting condition. Even after dilution of the soot stream into the catalytic reactor, the outlet filter paper samples still showed higher darkness levels. The uncertainty for the laser measurements of darkness levels was approximately $\pm$ 0.01.

Approximately 50% decrease in darkness was seen with the lighter soot samples at the -4.5 kV, while a 40-45% drop was measured at -5.0 kV under heavy soot conditions. It is likely that the electrostatic precipitator was driving a significant number of soot particles to the catalytic surface at voltages of -4.0 to -5.0 kV.

Soot mass density in the gas stream was determined from the filter paper samples by weight gain. Table 6.3 and 6.4 is a tabulation of weight gain and mass density as a function of applied voltage for the light and heavy sooting samples. Figures 6.8 and 6.9 show mass density as function of applied voltage. The data in both plots is highly scattered, and it is difficult to predict trends. Uncertainty analysis was performed and

found to be $\pm$ 3.9 x 10^{-8} g/cm^3. As shown in both figures, the uncertainty is so large that most of the data points fall within the uncertainty. This occurred because of the difficulty in obtaining accurate filter paper weight measurements.

Table 6.3 Weight Gain and Mass Density of Soot From Outlet Filter Paper Samples Light Sooting Conditions

Voltage (-kV)	Weight Gain (mg)		Mass Density (x 10^{-8} g/cm^3)	
	3/7/97	3/18/97	3/797	3/18/97
0	0.18	0.12	3.462	2.353
1.0	0.14	0.13	2.692	2.549
1.5	0.11	0.15	2.115	2.941
2.0	0.21	0.10	4.039	1.961
2.5	0.06	0.22	1.154	4.314
3.0	0.09	0.07	1.731	1.373
3.5	0.05	0.08	0.962	1.569
4.0	--	0.14	--	2.745
4.5	--	0.09	--	1.765
5.0	--	0.31	--	6.078

Table 6.4 Weight Gain and Mass Density of Soot From Outlet Filter Paper Samples Heavy Sooting Conditions

Voltage (-kV)	Weight Gain (mg)		Mass Density (x 10^{-8} g/cm^3)	
	3/14/97	4/1/97	3/14/97	4/1/97
0	0.60	0.12	8.627	1.961
1.0	0.50	0.13	9.804	1.961
1.5	0.40	0.15	7.843	2.549
2.0	0.28	0.10	5.490	2.157
2.5	0.50	0.22	9.804	2.941
3.0	0.50	0.07	9.804	7.059
3.5	0.63	0.08	12.353	1.961
4.0	0.44	0.14	8.627	7.255
4.5	0.23	0.09	4.510	2.941
5.0	0.16	0.31	3.137	2.549

Based on uncertainty in the data, the optical measurements using the laser provided an accurate method of measuring soot loading changes, as opposed to mass density data. Thus, penetration was equated to the amount of soot collected on the filter paper samples. As the applied voltage was increased, less soot penetrated and was collected on the reactor outlet samples. The optical measurement method, therefore, provided a way of determining relative changes in soot loading as the applied voltage was increased.

As soot is being driven to the catalyst wall, the other significant issue is whether catalytic oxidation of the soot has occurred. One major indicator of catalytic oxidation is the increase in the levels of CO and CO_2. A possible mechanism for this type of oxidation begins with the diffusion of O_2 through the bulk stream with its subsequent predissociation on the catalyst active site. As the soot (carbon) particles are driven to the surface by the electrostatic precipitator, they come into contact with the oxygen, and a reaction occurs. The presence of a catalyst helps to induce this reaction at a significantly lower temperature. Catalytic oxidation of diesel soot, using platinum as the catalyst, normally occurs at approximately 400 °C (Wyatt et al., 1993). Carbon monoxide and CO_2, produced as a result of catalytic oxidation, are desorbed from the surface, and diffused back into the bulk flow.

Figure 6.10 is a plot of CO and CO_2 (CO_x) concentration as a function of applied voltage for several experimental runs. The plotted runs were separated into two operating conditions: light and heavy sooting. For the light sooting conditions, the data points indicate an upward trend for CO_x concentration as applied voltage is increased from 0 to

-2.5 kV. At -2.5 kV, CO_x concentration reaches a peak and decreases with increased applied voltage. This peak CO_x concentration is nearly 50% higher than at 0 kV for the data taken on 3/18/97, and well above the 10-20% data scatter. For the light sooting experimental runs, the data on 3/18/97 has a higher oxygen flow through the catalytic reactor compared to the other runs on 2/20/97 and 3/7/97.

An increase in the measured catalyst surface temperatures over baseline values is a good indicator of oxidation taking place. Figure 6.11 is a plot of the increased catalyst surface temperature at -2.5 kV along the middle portion of the catalytic reactor tube for the experimental runs under light sooting conditions. The temperature increase is referenced to the surface temperatures taken when nitrogen gas (i.e. no oxidation likely) was flowing through the catalytic reactor.

The effect of increasing O_2 concentration in the catalytic reactor was significant. Higher temperature changes result with increased O_2, as opposed to 3/7/97 run with the same sooting conditions, but with a lower oxygen flow rate. This increase is also seen in Figure 6.12 where the maximum ΔT was plotted for both light and heavy sooting conditions. Maximum ΔT is defined as the highest surface recorded during the experimental run minus the baseline temperature (during N_2 addition into the catalytic reactor) during the experimental run. Most of the highest temperatures (light sooting conditions) occurred when the applied voltage was at -3.0 kV for the 3/18/97 run, while the majority of ΔT_{max} for 3/7/97 happened at -2.5 kV. The reason for the highest recorded temperatures being at -3.0 kV for 3/18/97 was because the surface temperatures not reaching steady state when they were recorded at -2.5 kV. However, the change in

temperature differences amounted to no more than 5 °C. The run at 3/797 had two recorded temperature readings at -2.5 kV, and the second recording was used in the calculation for ΔT_{max}.

From this data, there is a direct correlation for highest CO_x levels and highest surface temperatures corresponding at -2.5 kV applied voltage, under light sooting conditions.

Figure 6.11 also shows a steady increase in ΔT as one moves further up the catalytic reactor for the data taken on 3/18/97. This upward trend is consistent with soot capture at -2.5 kV. At low voltages, axial particle trajectory to the wall is much longer, so that particles further from the wall are more likely to be captured at the top portion of the catalytic reactor. Soot flowing nearer the wall is probably deposited by a combination of electrostatic precipitation, and diffusion. Since less soot is likely to be deposited in the lower portion of the catalytic reactor at this applied voltage, a lower temperature increase would be expected. These temperature increases on the catalyst monolith surface are an indication of exothermicity which characterizes oxidation reactions. With increased surface temperatures, one would expect that CO_x levels to be higher for the 3/18/97 run, in comparison with the runs of 2/20/97 and 3/7/97. Yet, from Figure 6.10, the CO_x concentration appears to be lower in comparison with the other two runs. The lower CO_x levels are attributed to dilution by the increased oxygen flow into the catalytic reactor. The higher catalytic oxidation effect by increased oxygen is consistent with Ciambelli et al. (1996), who noted increased catalytic oxidation (increased levels of CO_2) of diesel soot with increased partial pressure of oxygen.

In comparison, heavy soot conditions shown in Figure 6.12 show very low increases in monolith surface temperature. The higher soot particle density tends to heavily coat (i.e. foul) the catalyst, so that oxidation activity is reduced. The middle portion of the monolith shows the smallest change in temperature. This shutdown effect was also observed at higher applied voltages (-5.0 kV) even under light sooting conditions. The difference between light and heavy soot densities is that catalyst shutdown occurs at little or no applied voltage.

Visual inspection of the catalyst sheet after earlier experimental runs showed a heavy, uniform coating of entrained soot. Specks of agglomerated soot could be seen along the length of the sheet. Other run such as 3/7/97, 3/14/97, and 3/18/97 the middle portion of the sheet had a lighter or no coating of soot, while the ends retained a heavy coating of soot. This occurrence is consistent with the oxidation of the soot in the middle portion of the sheet, as further evidenced by that being the location of the highest surface temperatures.

Another interesting observation was made when the direction of the voltage variation was reversed; i.e. going from high to low. Once measurements were made at -5.0 kV, the applied voltage was decreased to -2.5 kV or to zero. Analysis for CO and CO_2 indicated continued high concentration levels similar to those found at -4.5 and -5.0 kV. When the applied voltage is turned down or off, the amount of soot depositing on the wall drops. The oxygen can more easily diffuse through the soot layer, so that catalytic oxidation continues at the same rate until the soot layer is oxidized.

One other note to remember is that when these data were taken, the catalyst had already been used extensively for over three months. Aging effects very likely reduced catalytic oxidation efficiency. The experimental run performed on 4/1/97 was supposed to determine whether the catalyst performance would increase with a combination of higher surface temperatures and O_2 flow. Unfortunately, the combustor flame drifted toward heavier soot during the middle of the run, so that this effect was negated.

Reactor residence time varied between 150-200 ms. The higher CO_x levels and increased change in monolith surface temperatures during the run on 3/18/97 had a residence time of 170 ms. The time the gas spent in the reactor during the heavy soot runs of 3/14/97 and 4/1/97 was approximately 150 ms. This residence time during the heavy soot runs may be a minor factor contributing to low oxidation.

At higher applied voltages the CO_x concentrations for light sooting conditions consistently decreased after -3.5 kV as shown in Figure 6.10. As discussed earlier, more of the soot particles reach the catalytic surface as evidenced from the outlet filter paper samples for voltages greater than -3.5 kV. It is likely that the layer of soot is accumulating on the catalyst surface at a faster rate than it is being consumed. Hence, this occurrence may cause decreased activity of the catalyst, which is consistent with the decreased CO_x levels observed.

On the other hand, the CO_x concentration for heavy sooting conditions showed a slight increase (see Figure 6.10). It is difficult to determine if this increase is real or whether this is due to data scatter. CO_x concentrations remained fairly constant from 0 through -3.5 kV. The heavy soot particle density probably coats the catalyst surface with

enough soot to cause an unchanged activity level of the catalyst. At voltages greater than -3.5 kV, the soot is accumulating more rapidly on the catalytic surface. The combination of a higher soot particle density and greater deposition evidently causes the catalytic activity to decrease dramatically, leading to shutdown. It is likely that this heavy soot layer impedes the diffusion of oxygen to the catalytic surface, representing another contributor to decreased catalytic activity.

6.2.2 SOF Effects on Catalytic Oxidation

Vaporized toluene (acting as a surrogate for SOF) was introduced into the catalytic reactor several times to determine whether it would enhance catalytic oxidation.

The SOF was first used when the center wire was absent. With no wire, the entrance of the reactor tube could be sampled. Chromatography analysis for both inlet and outlet toluene concentrations was performed. The introduction rate of SOF (vapor and carrier gas) at 25 °C during the two runs was approximately 360 cm^3/min.

These data were then compared with CO and CO_2 levels with and without SOF present. Small increases in CO_x occurred within the range of data scatter, but no significant increases in CO_x concentration were seen. Peak concentration of toluene decreased in the outlet samples, but this decrease was probably due to gas phase reactions. With no wire present, only a small amount of soot was depositing by diffusion, and hence, undergoing catalytic oxidation.

The central wire was then placed in the catalytic reactor tube. The SOF was again introduced into the reactor and measurements were taken. With the wire present no gas

samples at the entrance of the tube could be taken due to tight spacing. The SOF feed rate was then increased to 600 cm^3/min and no increased CO_x levels were detected from the reactor outlet gas samples. The toluene concentration, however, was 4 times higher than the previous outlet sample with no SOF. The peak concentration of toluene at the tube inlet would have been much higher if sampling was possible, but the outlet samples were lower due to gas dilution, and gas phase reactions.

From these results, SOF studies were concluded with no further investigation. The SOF was introduced in a gaseous state, and it is likely that the toluene remained in the gas stream rather than being adsorbed on the carbon of the soot. Unlike diesel soot that has some SOF coating the soot particles, the vaporized toluene may not have acted as an adsorbed hydrocarbon to the soot particle. The vaporized toluene was probably diluted in the bulk stream, which may explain the decreased concentration at the tube exit.

6.3 Soot Particle Sizing

Before any mathematical modeling was performed, particle size distribution data were needed. During the experimental runs, the HIAC/ROYCO particle counter was unable to provide a reliable and consistent indication of soot particle counts. Particle counts sometimes varied widely in the inlet samples with no apparent changes in operating conditions.

After the experiments were completed, the API Aerosizer (described in Section 3.2.4) was available for one time use only. Its time-of-flight measurement for determining particle size and real time output was instrumental in providing much needed information.

Figure 6.13 shows the output for two reactor inlet samples taken two hours apart. The result indicates the soot stream to be bimodal where the major peak occurs at 1.4 μm with a smaller peak at 3.0 μm. Since the particle size settings on the HIAC/ROYCO were set for 0.3-1.2 μm, the counts were always low with the exception of 0.3 μm. The majority of the soot particles were expected to be in the submicron range, much like diesel soot. The high counts at 0.3 μm seemed to confirm this. However, the API data showed these 0.3 μm counts to be simply noise.

The only input needed for the aerosizer instrument to report size data was particle mass density. The instrument's library has reference values for various particle mass densities. Carbon is listed as 1 g/cm^3. Soot is not just a pure carbon sphere, but rather it is a highly porous material. Therefore, a value of 1 g/cm^3 for soot was not reasonable. Hence, a value of 0.2 g/cm^3 for soot was used.

The instrument then generated the bimodal peaks at 1.4 and 3.0 μm. The density value of 0.5 g/cm^3 was then used in order to see how the peak distribution shifted. The distribution shifted downward showing the peak to be around 0.8 μm. The HIAC/ROYCO instrument, which does not require a density input, did not record any particles in this range. Increasing, the value of density closer to one would simply shift the peak curve further downward. Therefore, we concluded that the input density of 0.2 g/cm^3 was reasonable for this soot.

The API aerosizer also contained an aerodispenser which determines particle size from soot placed in a chamber. Soot scraped off the walls in the elbow section was analyzed. Repeated measurements indicated that the particle size for this soot was at 10

μm. This heavier size agglomerated soot probably settled on the walls or simply flowed out through the bypass. Only the smaller sizes such as 1.4 and 3.0 μm particles were able to flow up into the catalytic reactor section. Actually, the agglomeration may have helped the electrostatic precipitation, because the agglomerated soot has the capacity to carry more charge than smaller, submicron particles. These particles were more likely to be deposited at applied voltages of -4.0 to -5.0 kV as seen from the filter paper samples. Otherwise, the filter paper weight gain and percent darkness may have been higher.

6.4 Modeling Results

A two particle size fraction model was proposed based on the API Aerosizer results. The multi-fraction mathematical models, beginning with no applied field, and the second with a potential present were run with 90% of the particles at 1.4 μm and 10% at 3.0 μm. The first model, as discussed in Chapter 4, is an enhancement to Chen's single particle size and charge model by inclusion of multiple fractions. The second model is a variation obtained by deleting the diffusional flux term because the electric field flux term becomes dominant at high applied voltages.

The input file for the first model requires the tube radius, number of fractions, the particle radius, number of charges, and fraction of the total particle density for each size fraction. In addition, operating conditions such as gas stream temperature and velocity are specified. The input file for the second model was slightly different due to the applied field. In addition to the above inputs, it requires the radius of the central wire, the fraction

of saturation charge applied to each fraction, and the applied voltage. The input files for both models are shown in Appendix E.

The first multi-fraction model using the operating conditions in the catalytic reactor with no applied field yielded 0.899 volume penetration or 0.101 deposition at 40 cm (approximate length of the catalyst sheet). The 3.0 μm particle, even though it constitutes only 10% of the fraction, carries a higher weighted average because of its larger diameter. This fact may attribute to a higher deposition. The model was tested with 98% at 1.4 μm and 2% at 3.0 μm in order to determine the large particle effect. The model now predicted 97.7% penetration. As a comparison, the second model which includes an applied voltage predicted 2-3% deposition with -1.0 kV using 90% at 1.4 μm and 10% at 3.0 μm at 40 cm.

The output of the first model shows at axial distance $z = 0$, the appearance of a uniform, radial particle density as stated by one of the initial conditions. This uniform density goes to zero at the wall. As the distance z increases, this uniform core begins to decrease closest to the wall. Thus, this uniform core "leaks" radially outward (i.e. the value of the particle density decreases as the gas flows downstream). Chen (1978) assumed the existence of a uniform core. His solution technique then employed a cubic polynomial density profile in the concentration boundary layer and used the Integral Method to obtain the approximate solution. In both cases, the inlet particle density was assumed to be radially uniform at the tube inlet.

Chen presented his results with penetration and deposition as functions of the dimensionless distance. The dimensionless distance depends on the value for the

diffusivity, and thus looking at those results for a case with real values, one did not know how far to go to obtain high deposition. The multiple fraction model with no applied field predicted only 25% deposition at 5.6 miles (9000 meters) in a 0.75 in tube.

It is important to note that both Chen's model and the multiple fraction model with no applied potential produced consistent results, even though each model was solved using much different solution techniques.

Figure 6.14 shows a plot of applied voltage and catalytic reactor tube exit penetration using the two particle size fraction, applied voltage model at 35% saturation charge. Experimental data under light sooting conditions and the results from the API aerosizer are also plotted. The computer model computes both volume and number penetration information. The predicted penetration and the experimental results show excellent agreement. Soot reduction as determined by percent changes in the outlet darkness measurements gives results that are best compared to calculated volume penetrations/depositions generated from the model. The relative darkness measurements are based on the percent change at the applied voltage referenced to the darkness level with no applied field. The discontinuities in both curves are atttributed to plotting the predicted penetrations in 500 V increments, resulting in "piecewise" curves. Plotting smaller applied voltage increments would produce smoother curves except at the "kink" occuring at -4.0 kV. This discontinuity occurs because the large particle fraction (3.0 μm) is completely captured at the catalytic reactor wall. The smaller slope is the result of the smaller, lightly charged fraction (1.4 μm) being captured at a slower rate. Uncertainty in

penetration based on the darkness measurements is ± 0.02. An uncertainty bar is shown in Figure 6.14 at the data point (3/18/97) corresponding to -3.5 kV.

The model also showed the same trend with heavy sooting conditions at 35% saturation charge as shown in Figure 6.15. In this case, the model does not predict penetration as well. In fact, the model is overpredicting penetration. It appears that lowering the percent saturation input would shift both number and volume penetration curves to the right in order for the model to closely predict the heavy sooting condition.

Particles flowing through an applied field pick up charge from ions present in the field. When the particle will not accumulate any more charge, At this point, it is saturated. Particles > 1.0 μm usually pick most of their charge through "field charging" (Flagan and Seinfeld, 1988). Electrostatic precipitators often employ a corona discharge to charge the particles. The current experimental apparatus does not produce a corona; hence the particles must pick up their charge either from the combustion process or from thermal interaction between particles (Lawton and Weinberg, 1969). Based on the experimental results, the simulation using a 35% saturation level appears to accurately model the experimental system without the use of an external charging mechanism.

The applied voltage model can be used to predict both volume and number total penetration along the axial distance of the catalytic reactor tube. Figures 6.16 and 6.17 are parametric voltage variations (-1.0 to -5.0 kV) at 35% saturation charge using the two particle size fraction model of penetration along the axial distance z in cm. Figure 6.16 shows volume penetration of two particle sizes, 90% of the total number of particles are taken to have a diameter of 1.4 μm, with the remaining 10% at 3.0 μm. For applied

voltages of -1.0 to -3.5 kV the curves are linear. Most of the particles are penetrating (very little deposition) at the low voltages between -1.0 to -3.0 kV. These results are consistent with the filter paper samples.

Figure 6.17 shows number penetration along the axial distance. The difference in the steepness of the slopes (Figures 6.16 and 6.17) in the range of -1.0 to -3.5 kV is the weighting factor obtained by cubing the particle radius used in calculating volume penetration (see Appendix D). As the applied voltage is increased to -4.0 kV and above, the volume penetration shows a steep drop. Because of the average weight of the large particle fraction carrying more charge, the volume penetration rapidly drops until the large particles are completely deposited on the wall. The curves then resume a linear decrease, but at a slower rate. The smaller slope is due to the slower penetration of the smaller size particles. This increased particle capture to the wall at higher voltages can also be explained from the effects of the migration velocity (See Appendix D.1). Particle migration velocity (U_m) under the influence of an applied field is:

$$U_m = \frac{qV_o}{6\pi\mu a \ln(r_o/r_i)r} \qquad \text{(E6.1)}$$

It is evident that U_m is dependent on the relative magnitudes of the applied voltage V_o, particle charge q, and radius a. For a given particle size, U_m will change as a result of changes in particle charge and the applied field. Thus, U_m increases under the influence of higher V_o, and higher q if a partially charged particle picks up extra ions. Thus, faster particle capture to the tube wall for large size particles results from an increased applied field.

The number penetration curves show linear curves for increasing applied voltages since they carry less charge. A small "kink" in the curve at -3.5 kV and above indicates that the large particle fraction is completely deposited. These kinks are the result of using just two fractions to approximate the actual continuous particle size distribution. The use of more fractions would better approximate the true distribution and would result in their disappearance. Number penetration is weighted by the percent of the particle size, so the simulation results show that the curves are weighted toward the larger fraction particle size. The results of the simulation model can also show the amount of penetration of each particle size for each incremental axial distance z. Thus, as voltage increases, the output shows at what distance a large particle with much charge is completely dropped out.

The simulation models used a fully developed laminar profile in order to derive the equation for penetration. The flow through the catalytic reactor tube was not fully developed, however, it may have been reasonably close. The simulation models were able to predict penetration quite well with the experimental data using a laminar profile. Slight variations may be attributed to actual flow conditions not being quite fully developed in the catalytic reactor. Based on good predictions, no further efforts were made in complicating the derivation for penetration by including entrance effects.

Higher percent saturation charge on the particles shifts the penetration curves toward the left, indicating higher particle capture on the tube wall. (See Figures 6.18 through 6.20). The relative fit to the data is not in good agreement.

CHAPTER 7

FINAL CONCLUSIONS AND RECOMMENDATIONS

7.1 Conclusions

From the experimental observations and model predictions, a reactor as described in the experimental apparatus section shows the feasibility of combining two principles: electrostatic precipitation and catalytic oxidation, as a practical technology for use in soot reduction. The following conclusions are drawn:

(1) Light sooting conditions were an important factor for both the electrostatic precipitator and the catalyst. A lower soot particle number density allowed for a more uniform deposition to the catalyst surface at lower applied voltages. The catalytic oxidation, as evidenced by increased $CO + CO_2$ concentrations, reached a maximum at -2.5 kV.

(2) Increased oxygen concentration in the catalytic reactor gas stream was the most important factor in promoting catalytic oxidation. A higher level of oxidation was evidenced by both increased CO_x concentrations and increased monolith surface temperatures at -2.5 kV under light sooting conditions.

(3) Increasing the applied voltage in stepwise increments, by starting with no applied field, gave best results for catalytic oxidation. If a high applied voltage was quickly applied, the soot rapidly accumulated on the surface, causing the catalyst activity to decrease. Once the applied field was significantly reduced or

turned off, the CO_x concentrations remained high until the built-up soot layer on the surface was oxidized.

(4) The particle size fraction of soot flowing into the catalytic reactor from the combustor indicated a bimodal distribution. The largest peak occurred at 1.4 μm, while a much smaller peak was found at 3.0 μm.

(5) A two particle size fraction, based on inlet soot measurement using the API Aerosizer, was used as input in the mathematical models with and without an applied field present. The input data consisted of two particle sizes, 90% of the total number of particles were of a diameter of 1.4 μm, with the remaining 10% at 3.0 μm. The first model with no applied field showed a high penetration of 0.899, which meant very few particles were captured on the wall by diffusion. Experimental observations confirmed that little or no deposition occurs in the absence of an applied field in the tube length under study. When used with a single particle size, the enhanced model results agreed with those of Chen (1978), who used a different solution technique.

(6) The second model, incorporating the applied field, satisfactorily predicted the observed outlet volume penetration. The model predicted a reasonable penetration of 50% using 35% charge saturation levels for the soot particles. This low particle saturation charge is attributed to the particles having to acquire most of their charge from both the combustion process and by thermal interaction. In addition, the second model appeared to provide a reasonable prediction of volume and

number penetration along the axial distance of the catalytic reactor using voltage variation as a parameter.

(7) For a given soot loading, an intermediate preferred voltage exists for soot capture without regeneration, i.e., catalytic oxidation of soot at the wall. At higher voltages, soot buildup appears to overwhelm the catalyst, decreasing oxidation.

This final point is illustrated in the following recommendations for a hypothetical device utilizing the electrostatically precipitator/catalytic reactor.

7.2 Recommendations

From the results of this research effort, the following recommendations are offered for future work:

(1) Use of monolith sheets with various catalyst loadings. Such a variation would be useful in determining if higher voltages can be applied in conjunction with a reactor using a higher catalyst loading to oxidize soot faster.

(2) Catalyst characterization beginning with a fresh catalyst and observing the ability to catalytically oxidize soot as it ages.

(3) Use of an external charging mechanism in order to further charge the soot particles prior to entering the catalytic reactor. Fully charged particles would require less applied voltage to be deposited. The resulting impact on tube sizing and length could be studied.

(4) Catalytic reactor tubes of various lengths to determine particle penetration and measure the soot loading on filter paper samples under different applied voltages.

Various length tubes may help in observing heavier particle deposition, with subsequent comparison to model predictions along the axial distance.

For a final recommendation, a design guideline based on a higher gas stream flow rate is proposed. A hypothetical situation is considered in order to show that this apparatus can function as an electrocatalytic controller of exhaust soot.

If an exhaust stream flow of 500 ft^3/min at 400 °C, what type of reactor configuration is needed for good soot capture/destruction? Two constraints are that the flow should be laminar with Reynolds Number < 2000, and it is recommended that the exhaust soot consist of a light soot particle density ($\approx 5.0\text{-}7.0 \times 10^{-8}$ g/cm^3)

We will use a catalytic reactor tube of 1.5" i.d. and length of 3 ft. These dimensions were chosen based on experience with electrical short circuiting, and using a length that will allow gradual soot accumulation along the entire surface. A charging device was hypothetically assumed to be in use to fully charge the particles prior to entering the reactor.

Based on the flow constraints, an average fluid velocity of 3.0 m/s will ensure that the flow at 400 °C will remain laminar. The Reynolds number for this velocity and temperature is about 1800. The number of parallel tubes needed for this total flow rate is 69. Unfortunately, the configuration becomes rather complicated and impractical for an application requiring compactness.

Computer simulation runs calculating volume penetration along the axial distance for applied voltages of - 4.0, -5.0, and -6.0 kV are shown in Figure 7.1. A particle size fraction approximating a size distribution was assumed: 1.0, 1.5, and 2.0 μm with the

percentages of 70%, 20%, and 10%, respectively. These sizes were selected because of current environmental interest in removing small size particles. The curves for -4.0 and -5.0 kV shown in Figure 7.1 show a downward linear trend along the tube length with total penetration between 0.60 - 0.80. Therefore, 20% - 40% of the particles are deposited. The curve for -6.0 kV drops much more sharply and shows the "kink" where the 2.0 μm is completely deposited. Uniform soot deposition along the entire tube length is shown with the -5.0 kV curve.

In order to reduce volume penetration below 1%, a tube length of 210 cm is required for a voltage of -5.0 kV. Thus, a considerable tube length is required at this potential to reduce the soot particle density to nearly zero.

Experimentation is required to determine if the catalyst used is able to catalytically oxidize the soot accumulating on the surface with these applied voltages. Maximum CO_x concentration by gas analysis would determine what voltage should be used. The potential for using other catalysts which would sustain higher temperatures and reaction rate should be considered and tested.

It is worth that several factors are important in designing a electrostatically enhanced catalytic reactor.

(1). The flow velocity through a tube should be low enough to remain laminar. Too high velocities will simply cause the captured particles to shear off of the wall. In addition, a longer reactor residence time results from lower velocities, so that better conversion of CO_x is attained.

(2). Catalytic surface temperature should be close to where significant catalytic activity for oxidation is expected. Gas temperature should be high enough or close to the surface temperature to prevent surface temperatures from cooling down.

(3). Catalyst loading is important in oxidizing soot. Higher precious metal loading is recommended.

(4). The tube radius should be sufficiently large in order to prevent electrical short circuiting when voltage is applied.

(5). Some means of preventing soot accumulation near the wire and its connections are important to prevent short circuiting. Soot is an electrical conductor. If enough is present, it can cause the center wire to electrically short..

(6). Use of an external charging mechanism to precharge the particles prior to entering the electrostatic precipitator. Low collection efficiencies result because the particles cannot reach near charge saturation levels.

APPENDIX A

FIGURES

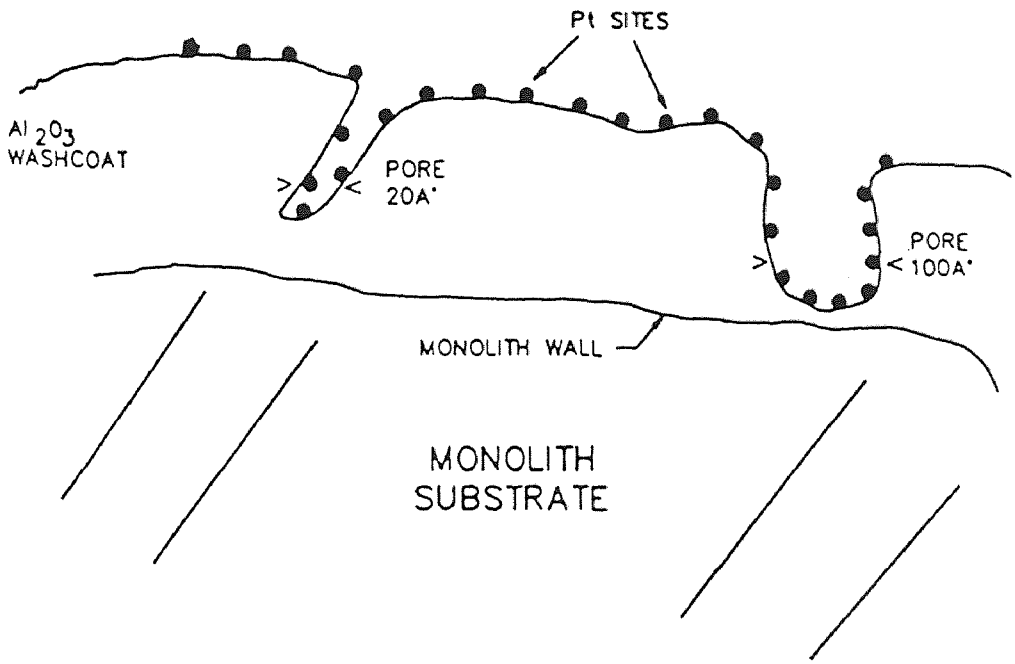

Figure 1.1 Conceptual Model for Catalytic Sites Dispersed on a High Surface Area Al_2O_3 Carrier Bonded to a Monolith (figure taken from Heck and Farrauto, 1995)

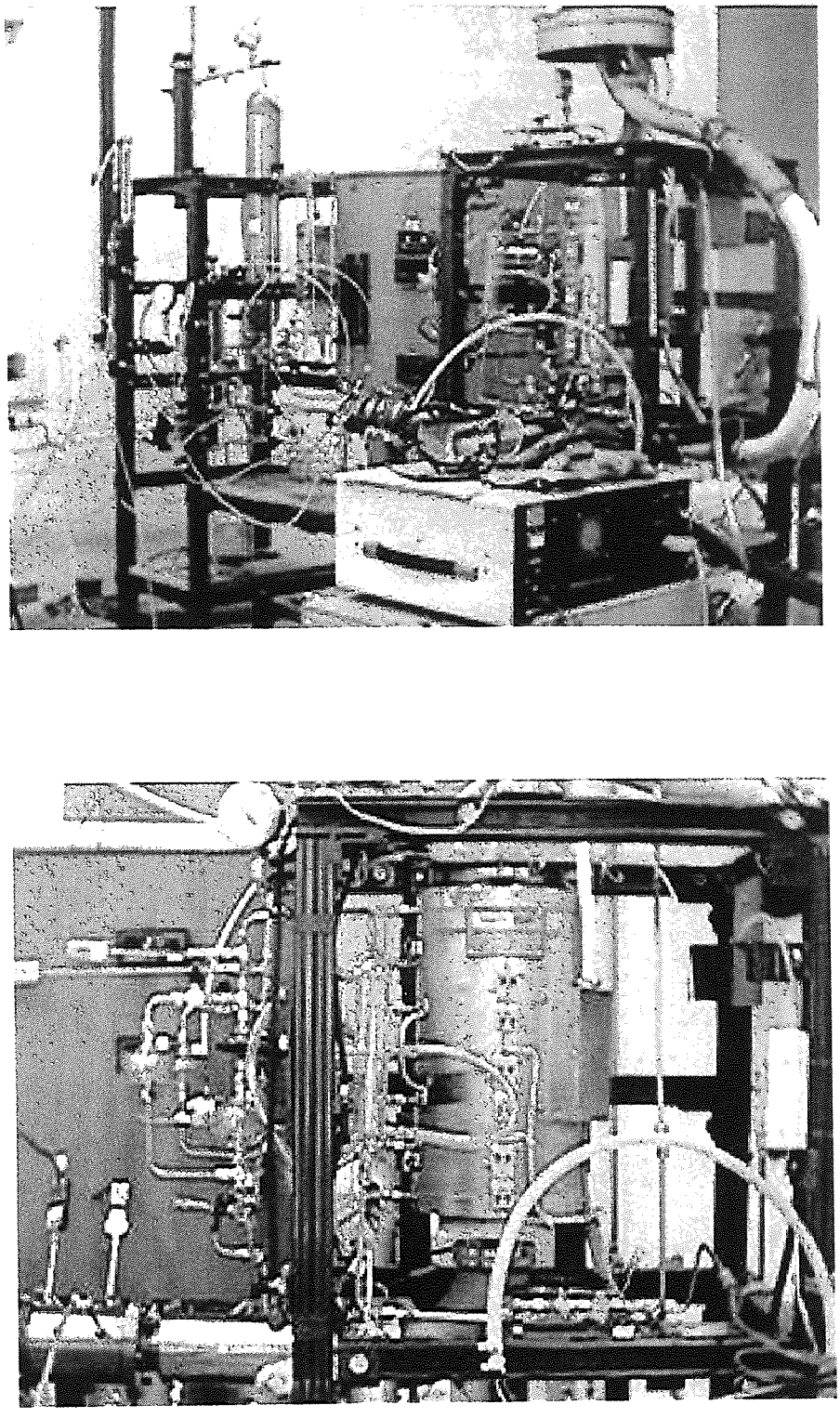

Figure 1.2 Experimental set-up showing test bench assembly and catalytic reactor section

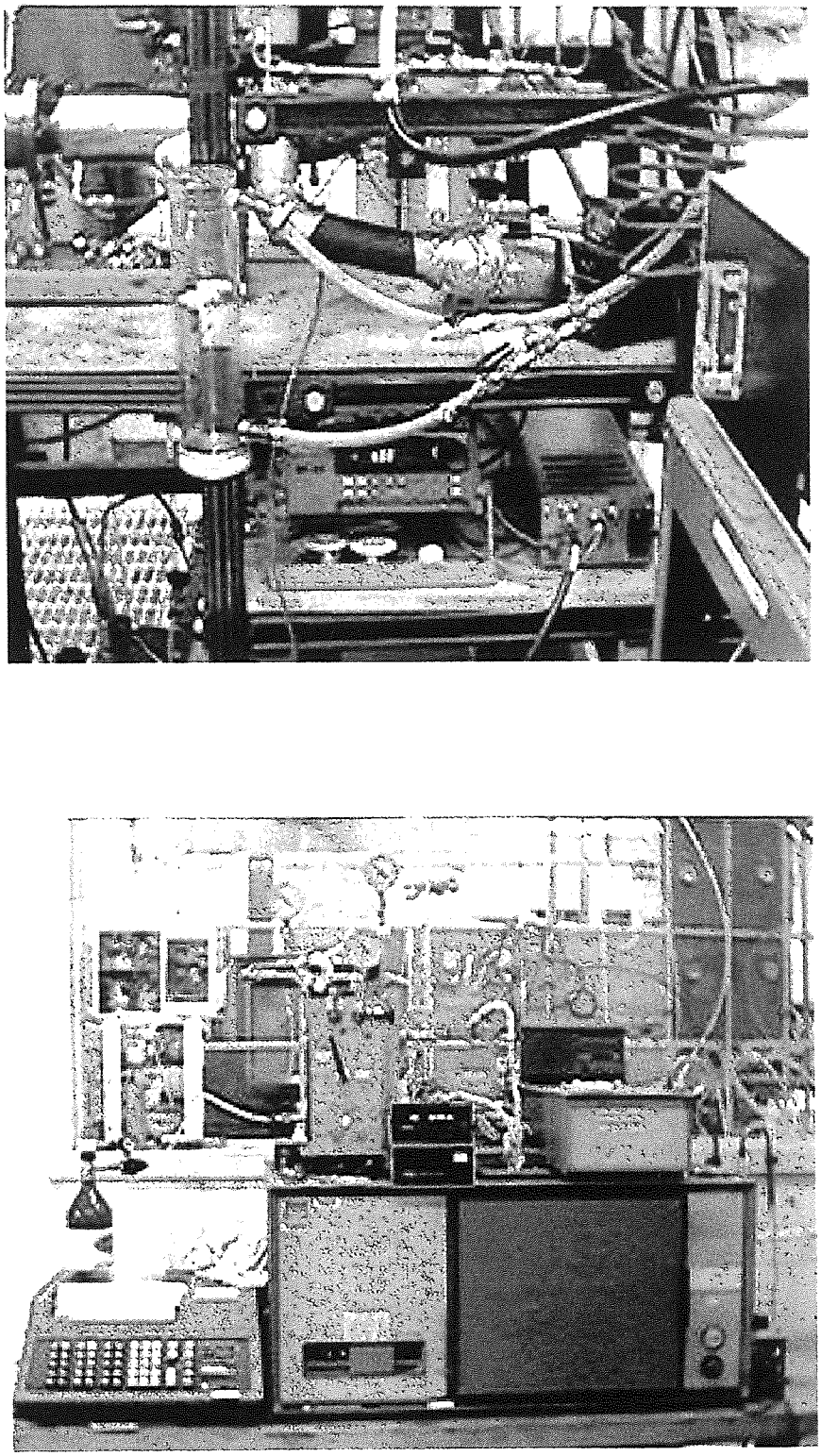

Figure 1.3 Experimental set-up showing data acquisition unit, DC power supply, and gas chromatograph used in gas sampling

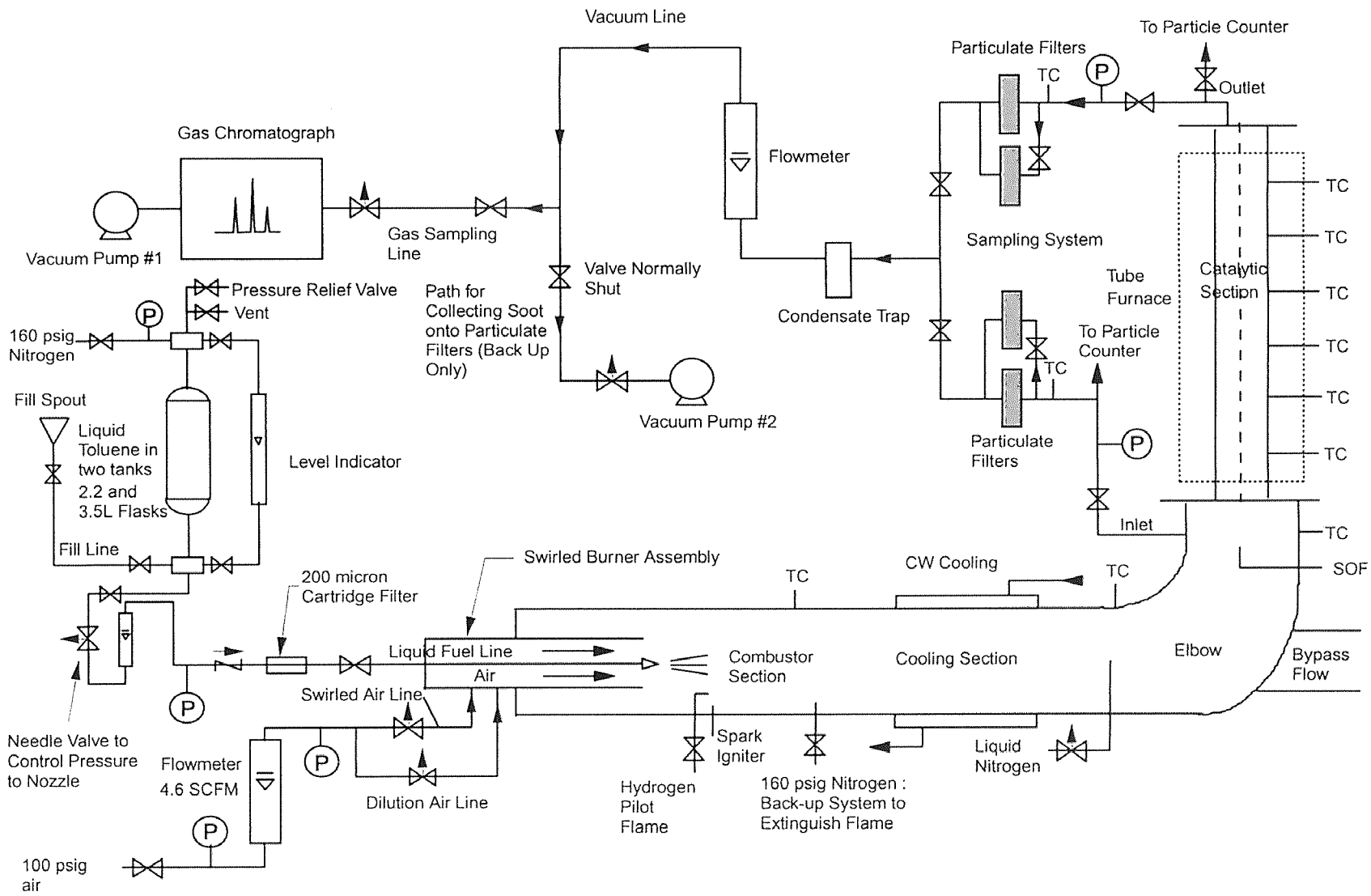

Figure 3.1 Experimental Shematic

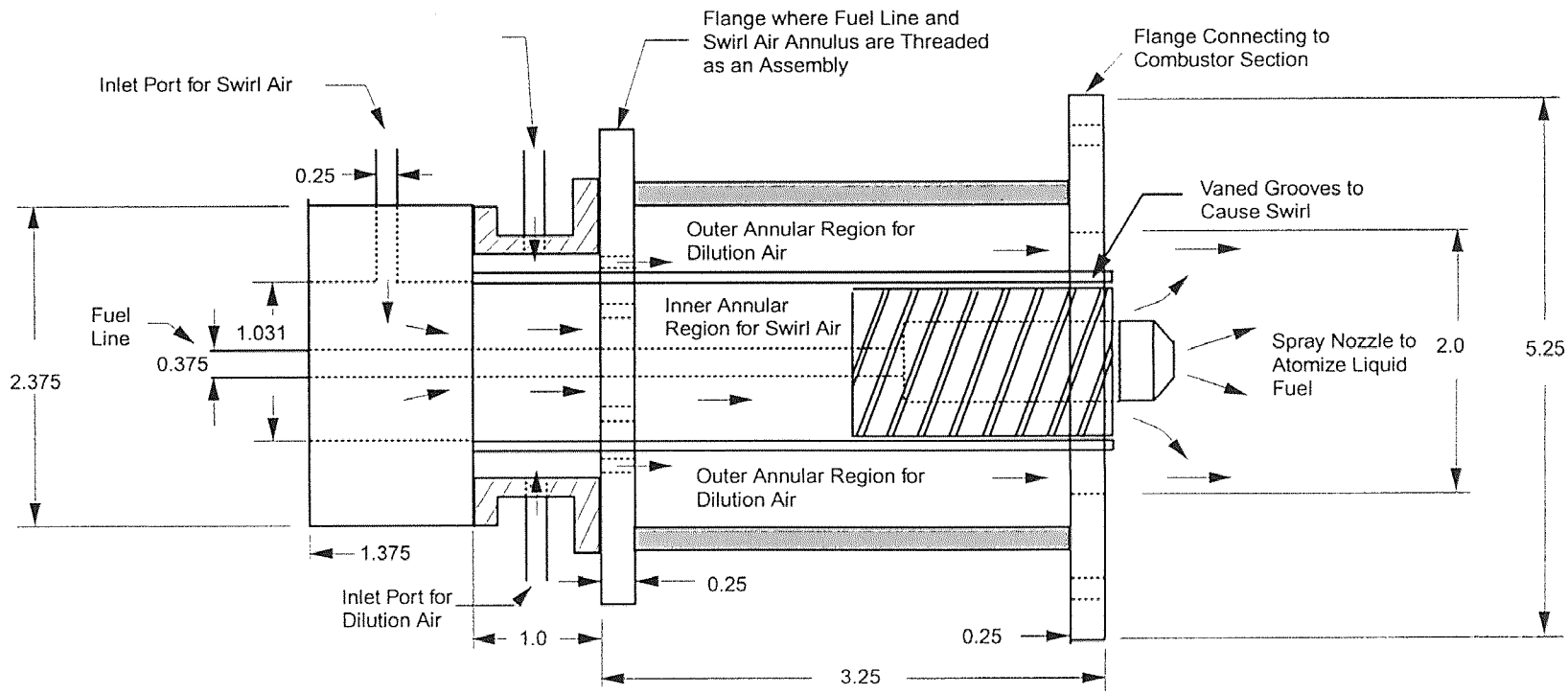

Note: All dimensions are in inches

Figure 3.2 Swirled Burner Assembly (Not Drawn to Scale)

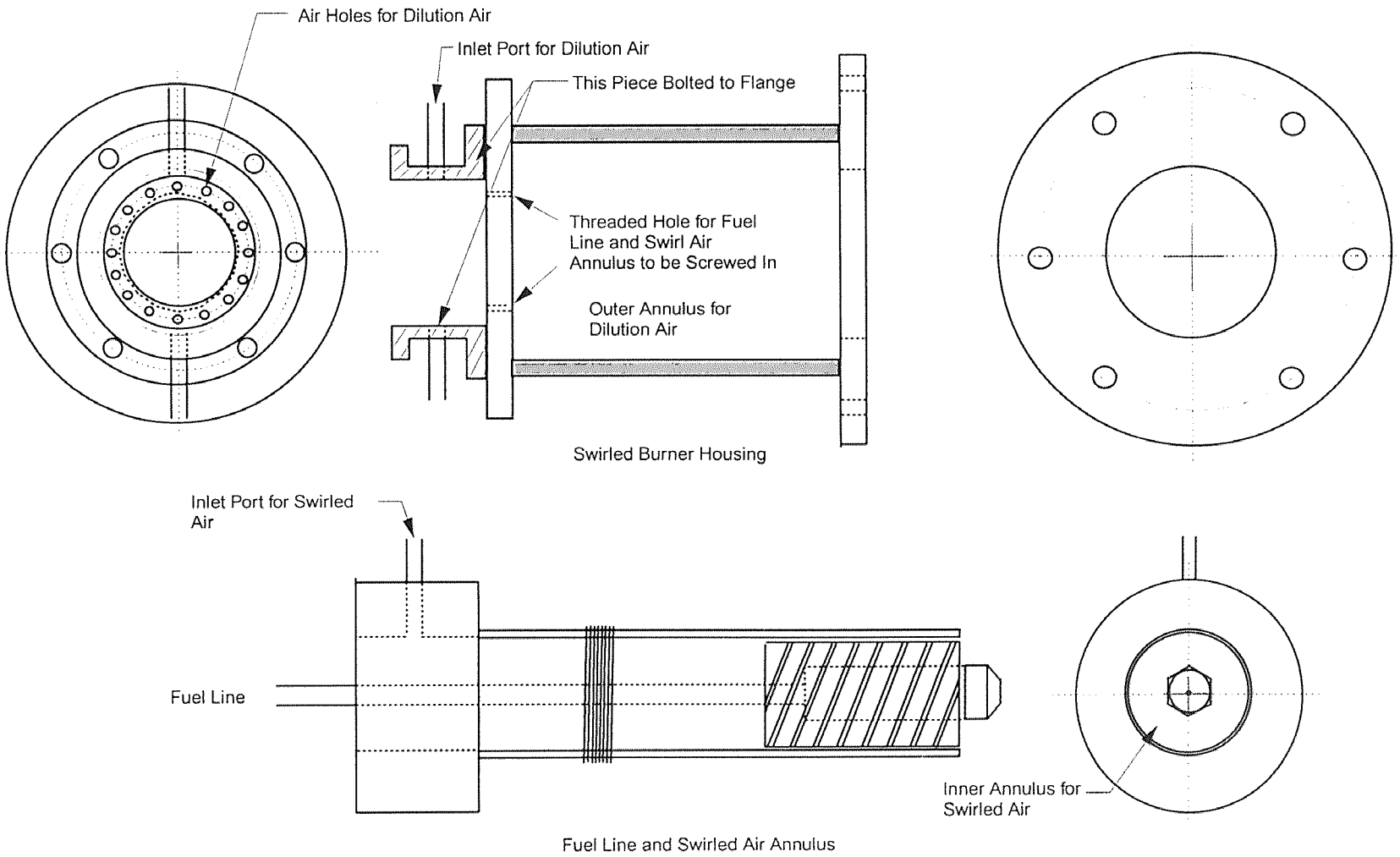

Figure 3.3 Disassembled View of the Swirled Burner Assembly

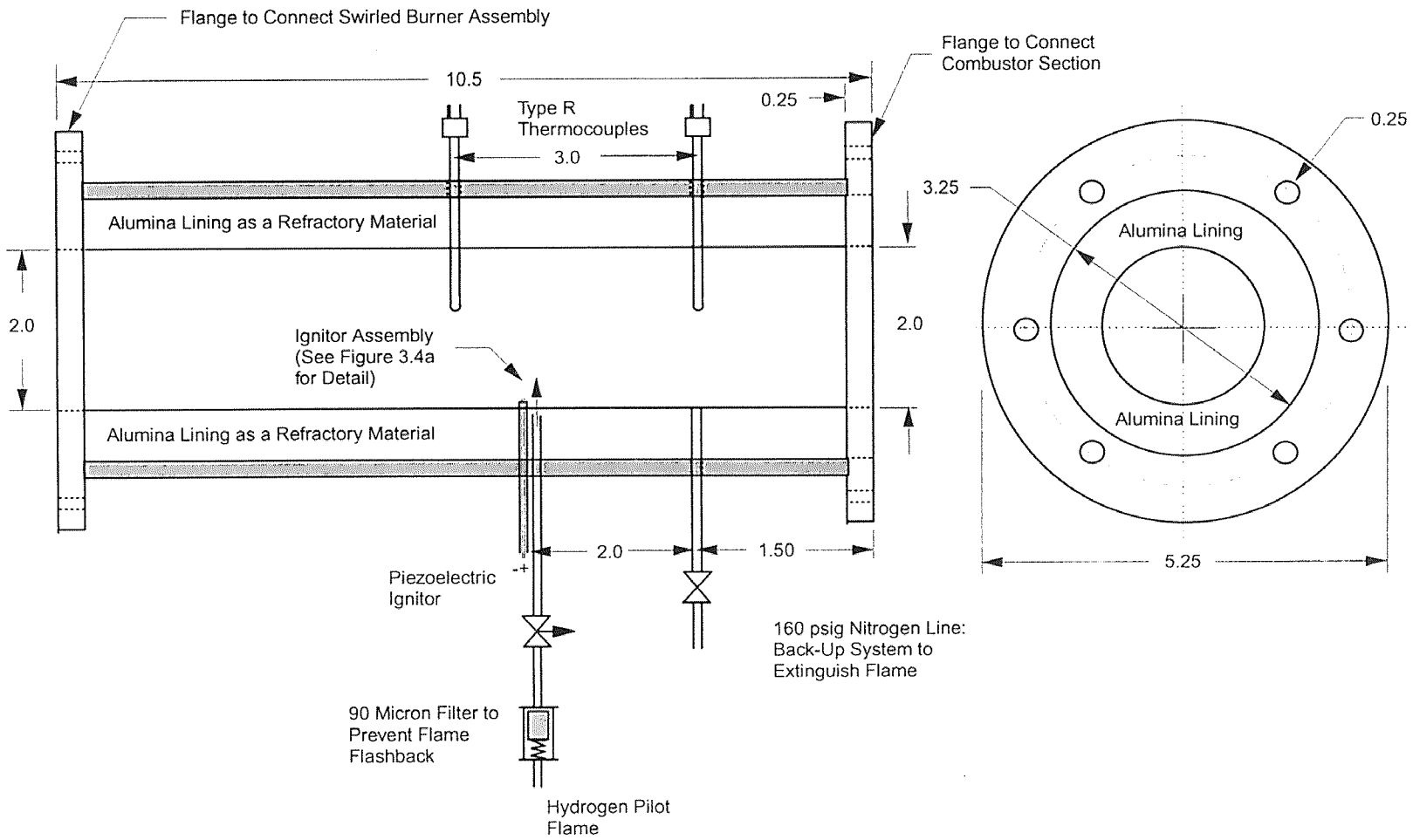

Note: All dimensions are in inches

Figure 3.4 Combustor Section (Not Drawn to Scale)

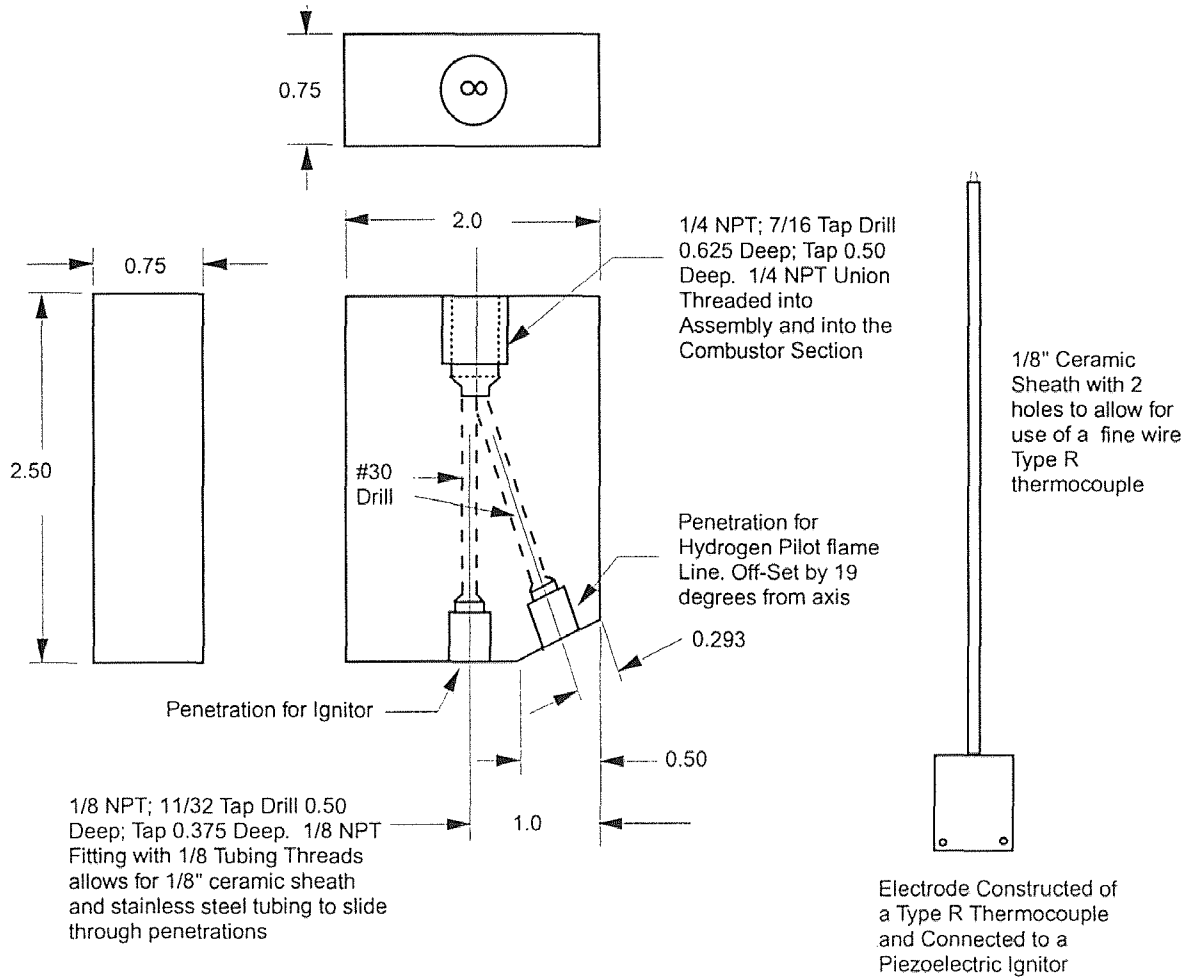

Note: All dimensions are in inches

Figure 3.4a Ignitor Assembly That is Theaded into the Combustor Section (Not Drawn to Scale)

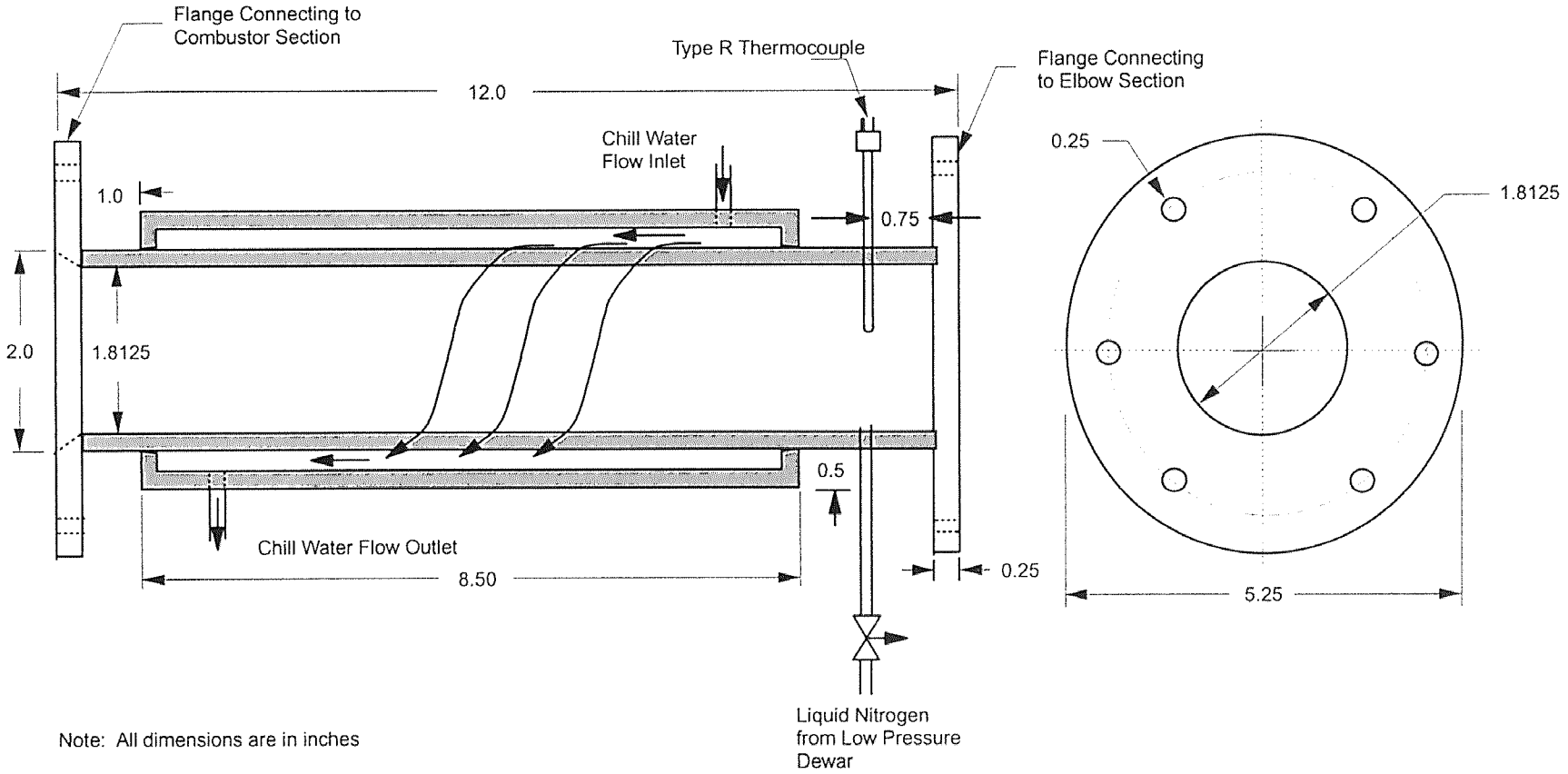

Figure 3.5 Cooling Section (Not Drawn to Scale)

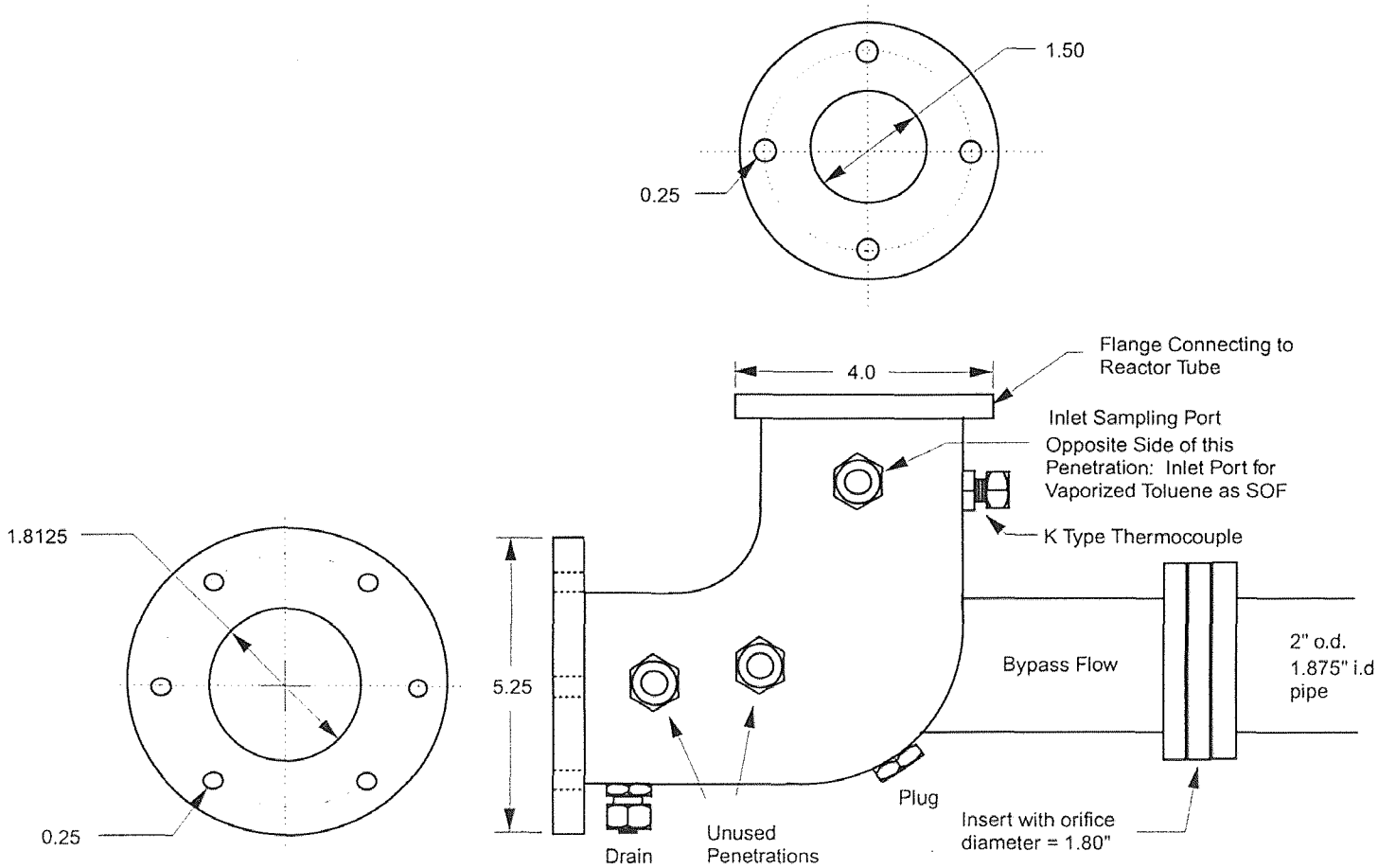

Note: All dimensions are in inches

Figure 3.6 Elbow Section (Not Drawn to Scale)

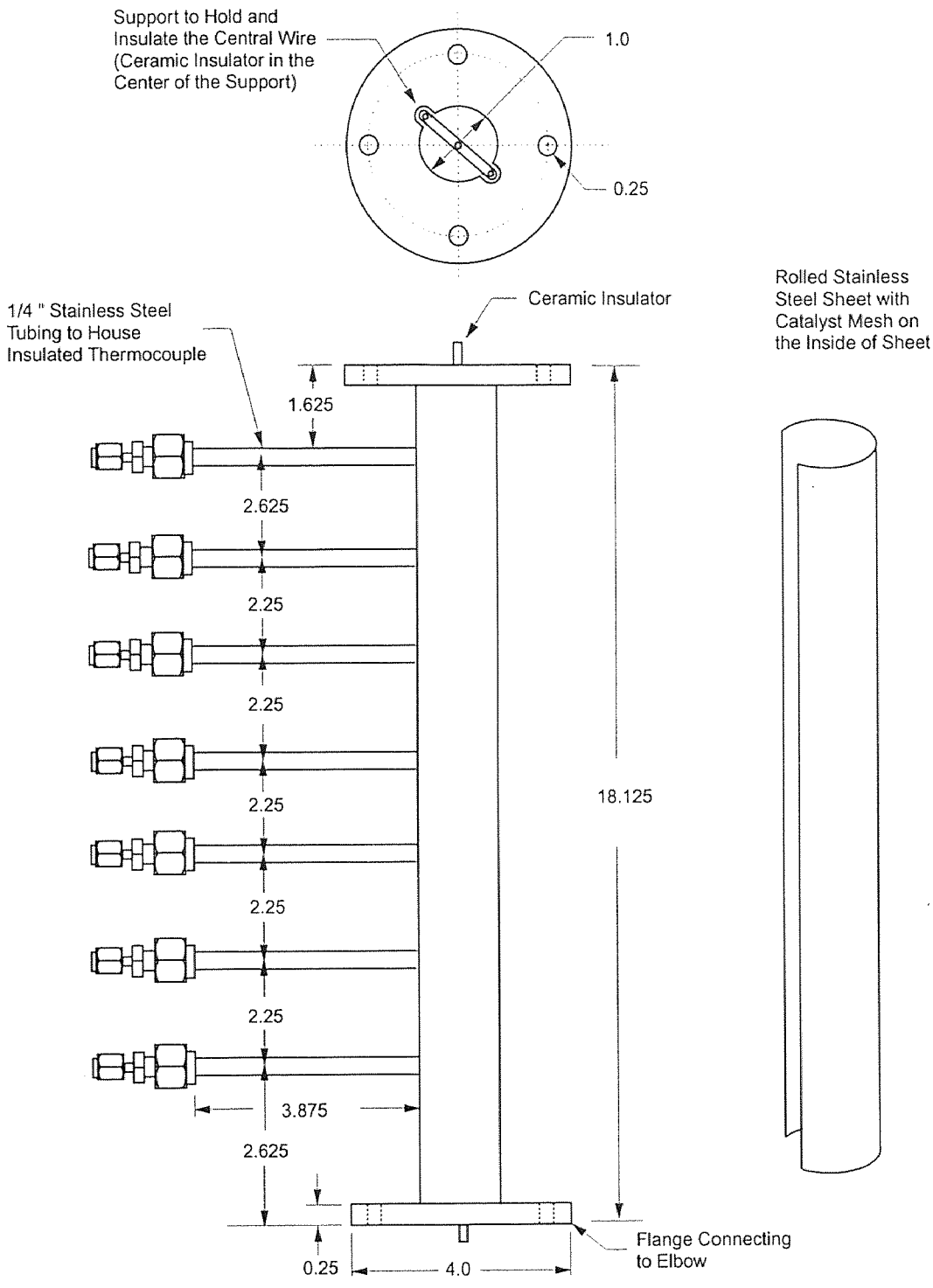

Note: All dimensions are in inches

Figure 3.7 Reactor Tube (Not Drawn to Scale)

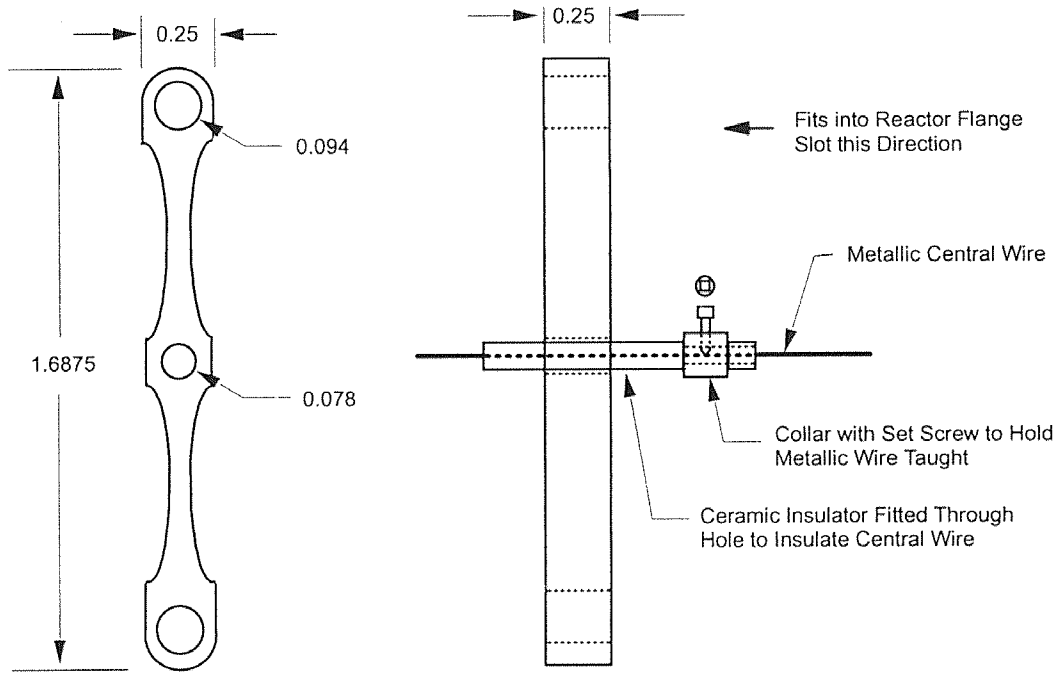

Note: All dimensions are in inches

Figure 3.8 Support to Hold Central Wire in Place on Each End of the Reactor Tube (Not Drawn to Scale)

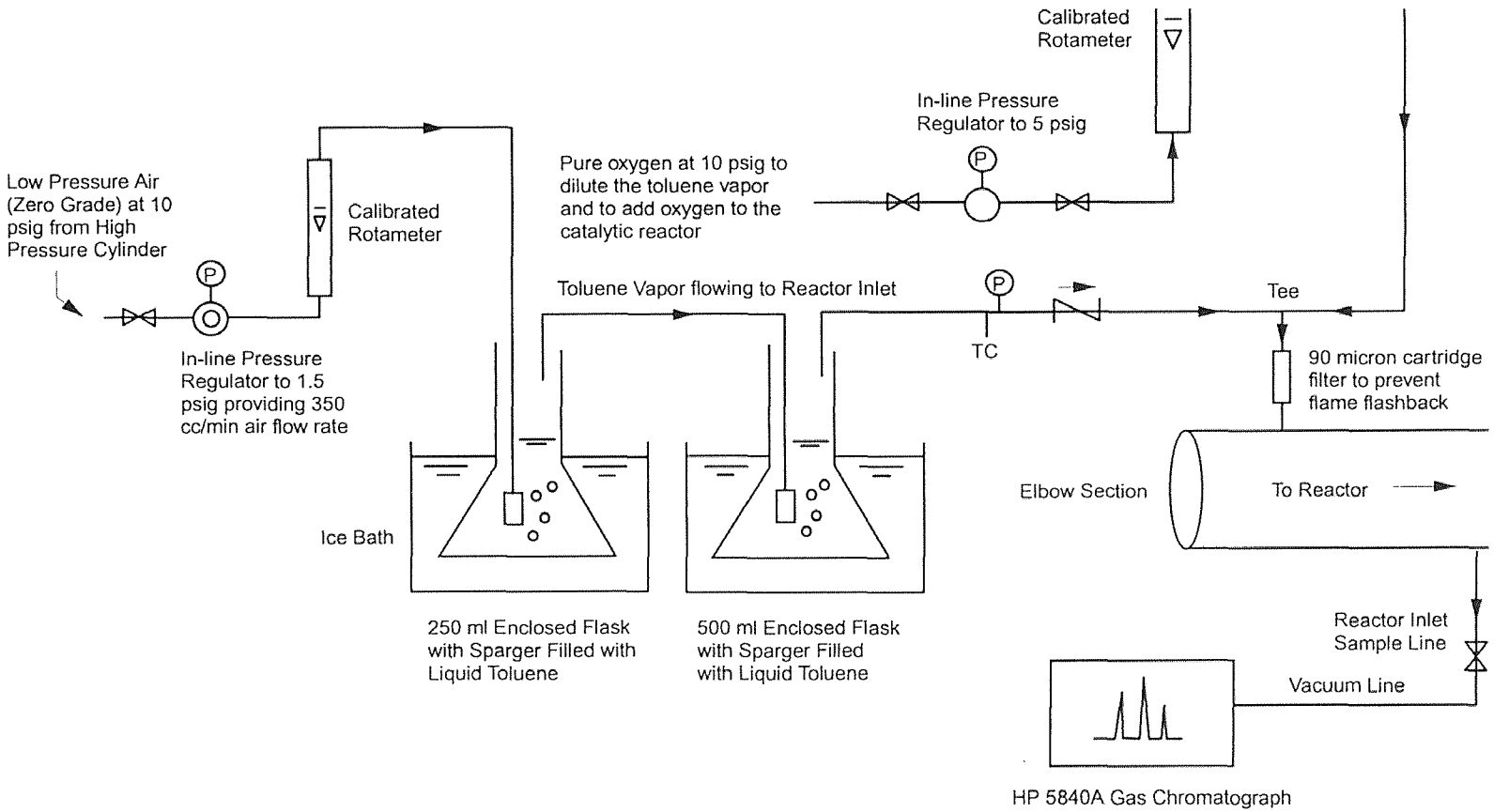

Figure 3.9 Diagram of Vaporized Toluene into the Catalytic Reactor

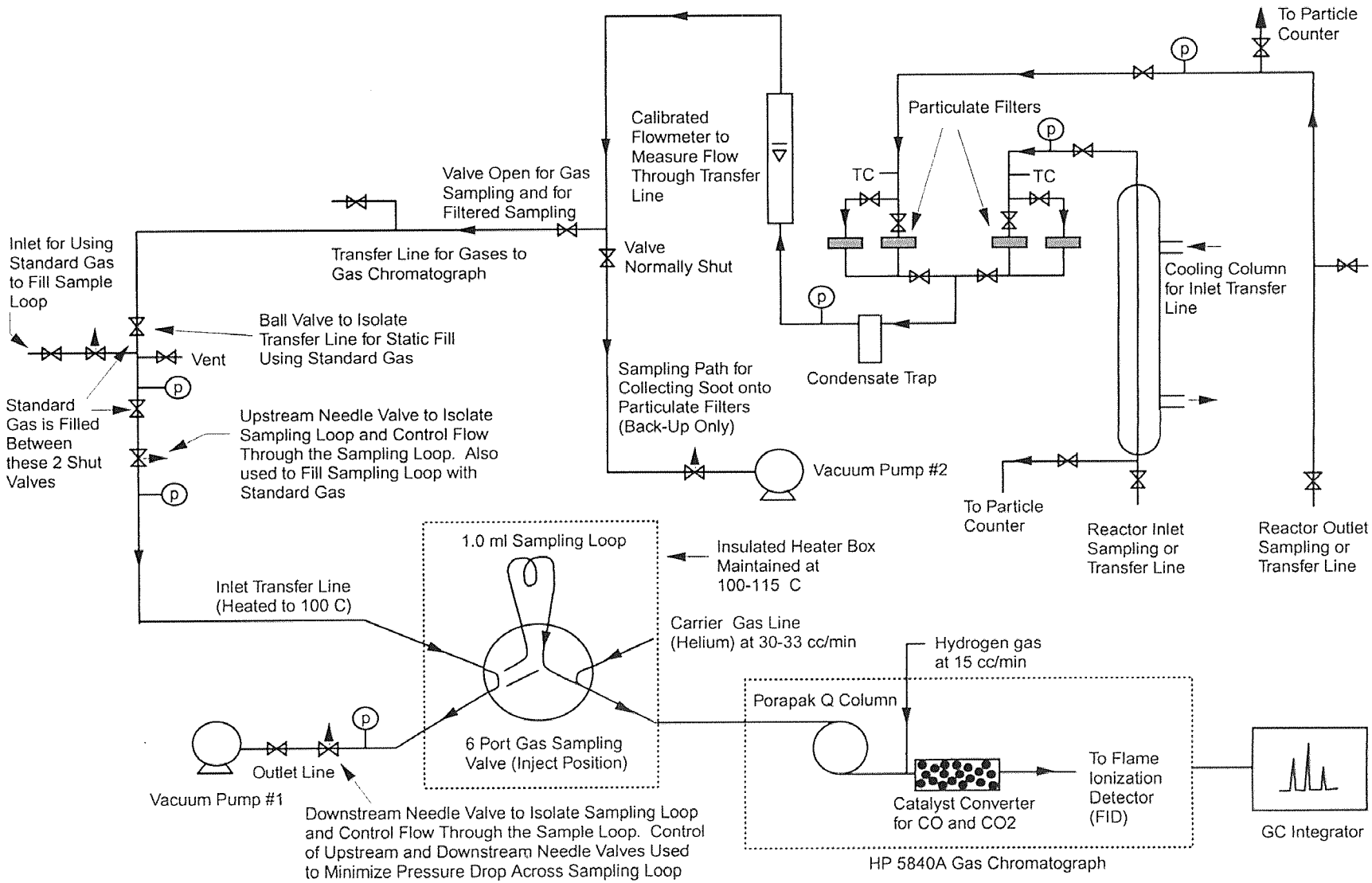

Figure 3.10 Sampling System

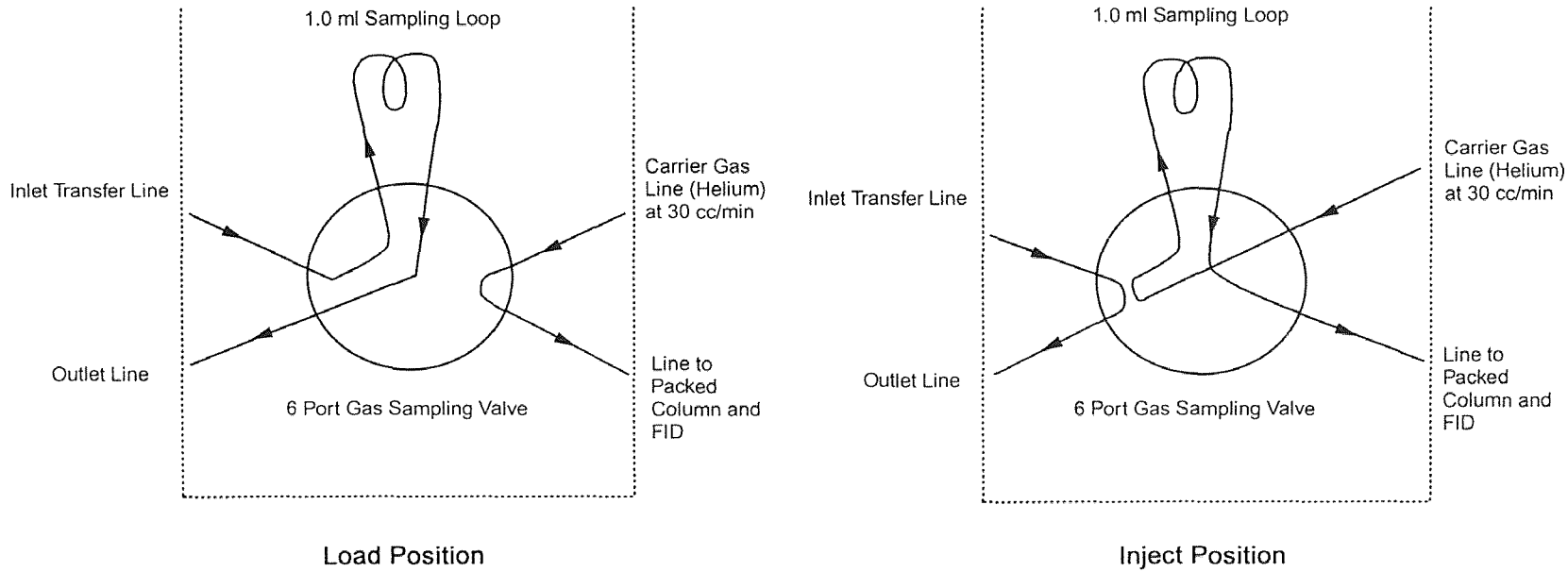

Figure 3.10a Flowpath of Gas for the Two Positions of the 6 Port Gas Sampling Valve

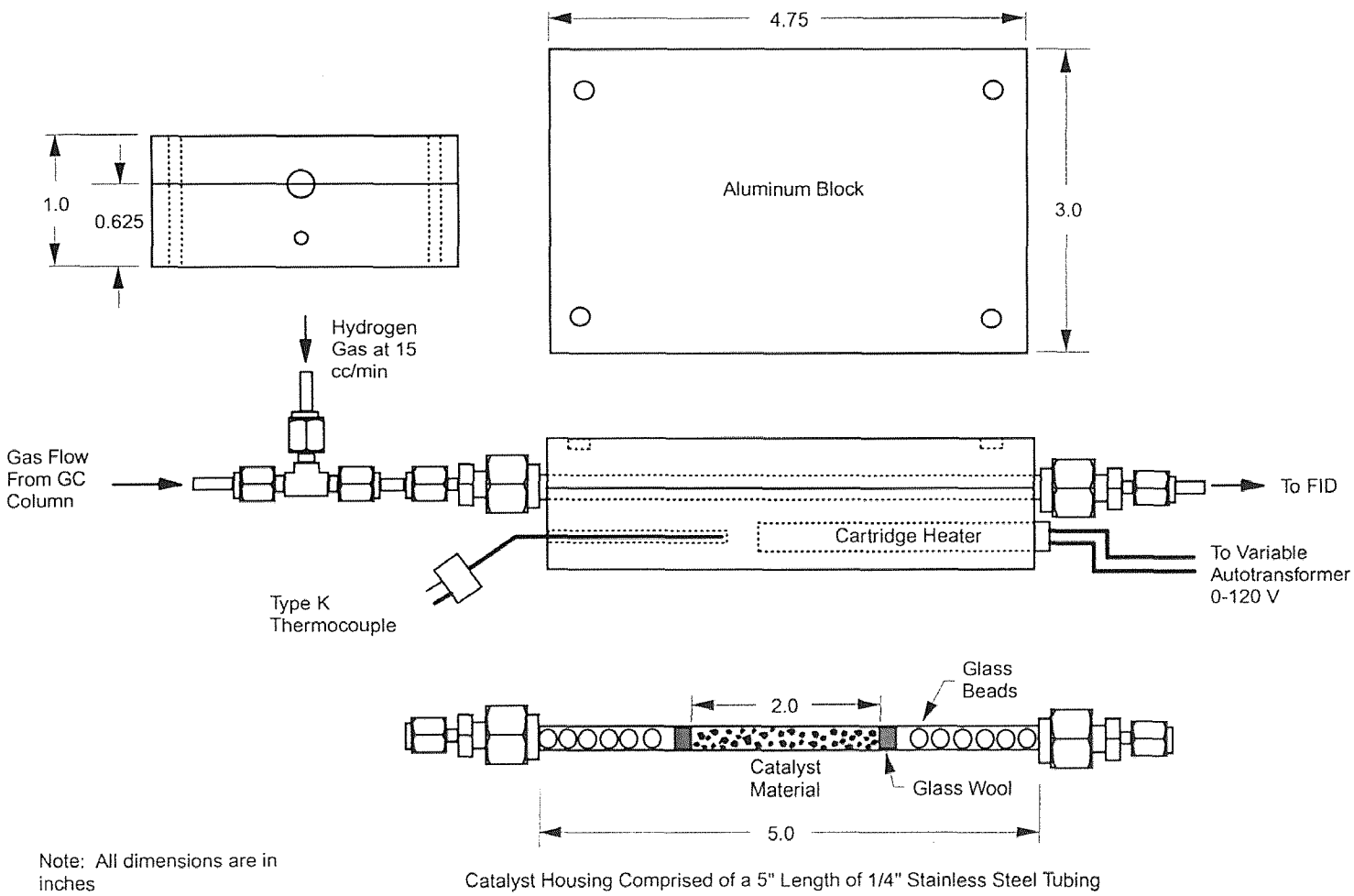

Figure 3.11 CO and CO2 Methonizing Catalyst Housing and Heating Block Assembly (Not Drawn to Scale)

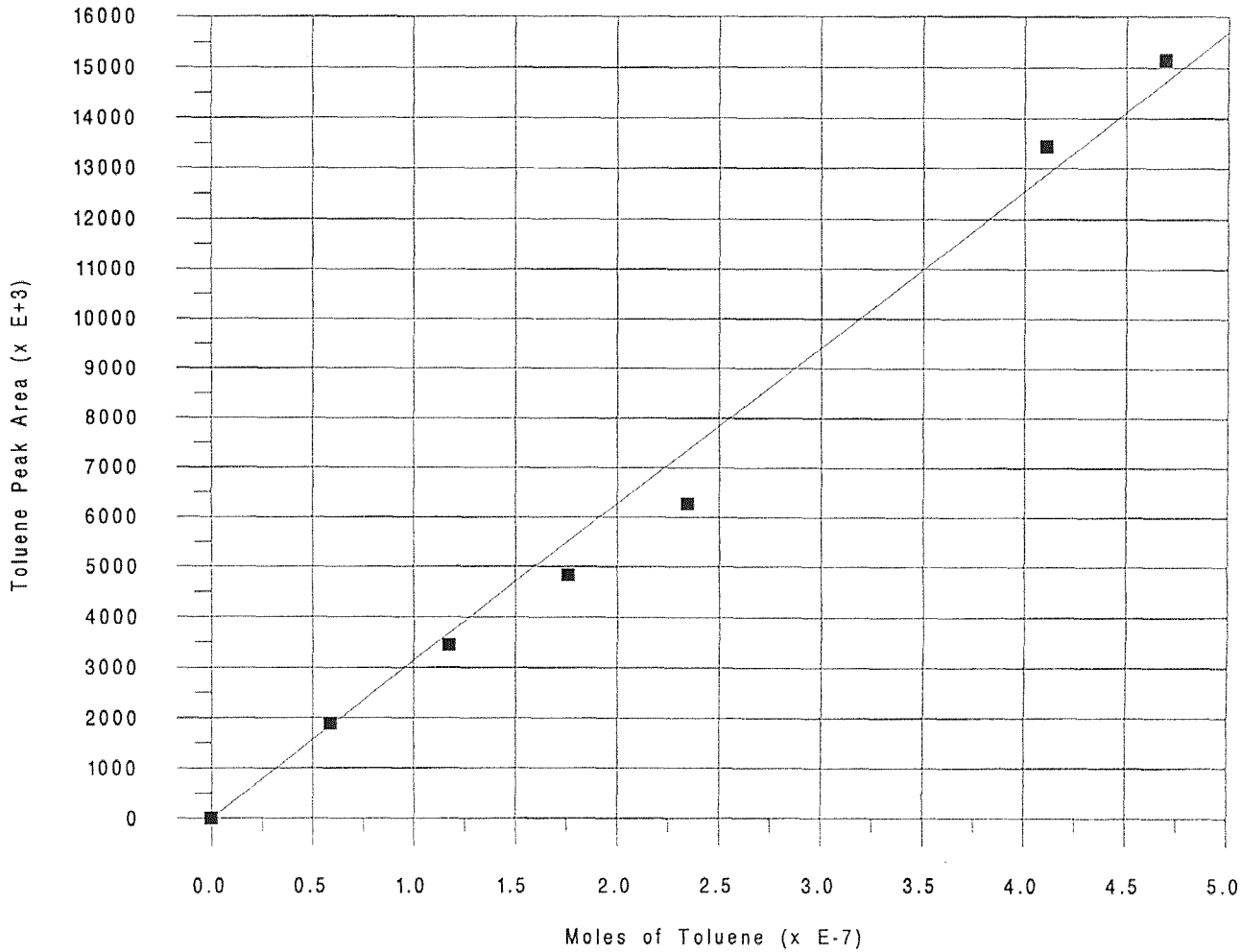

Figure 3.12 GC Calibration Curve for Toluene

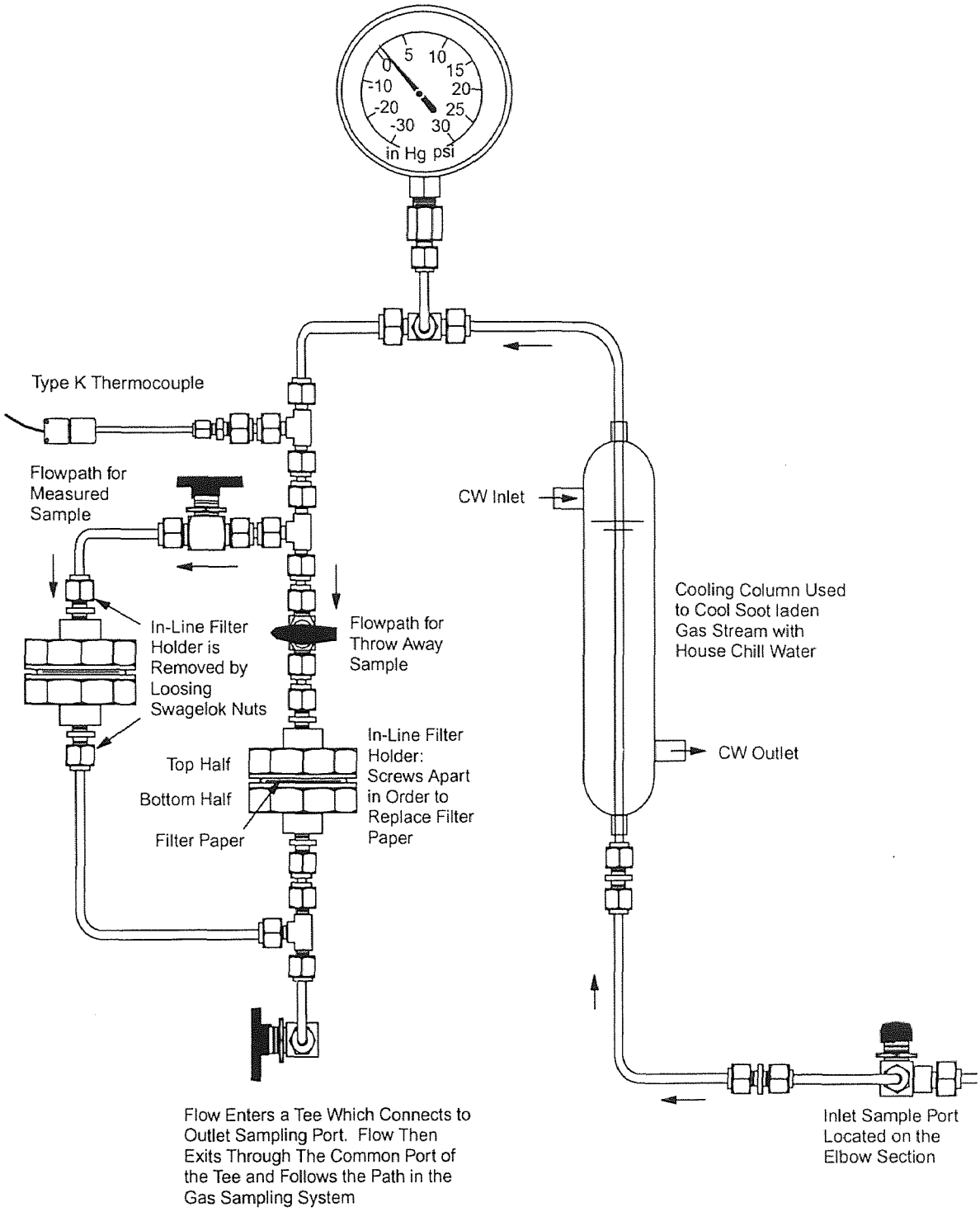

Figure 3.13 Diagram of Inlet Sampling System Showing Arrangement of Particle Filters

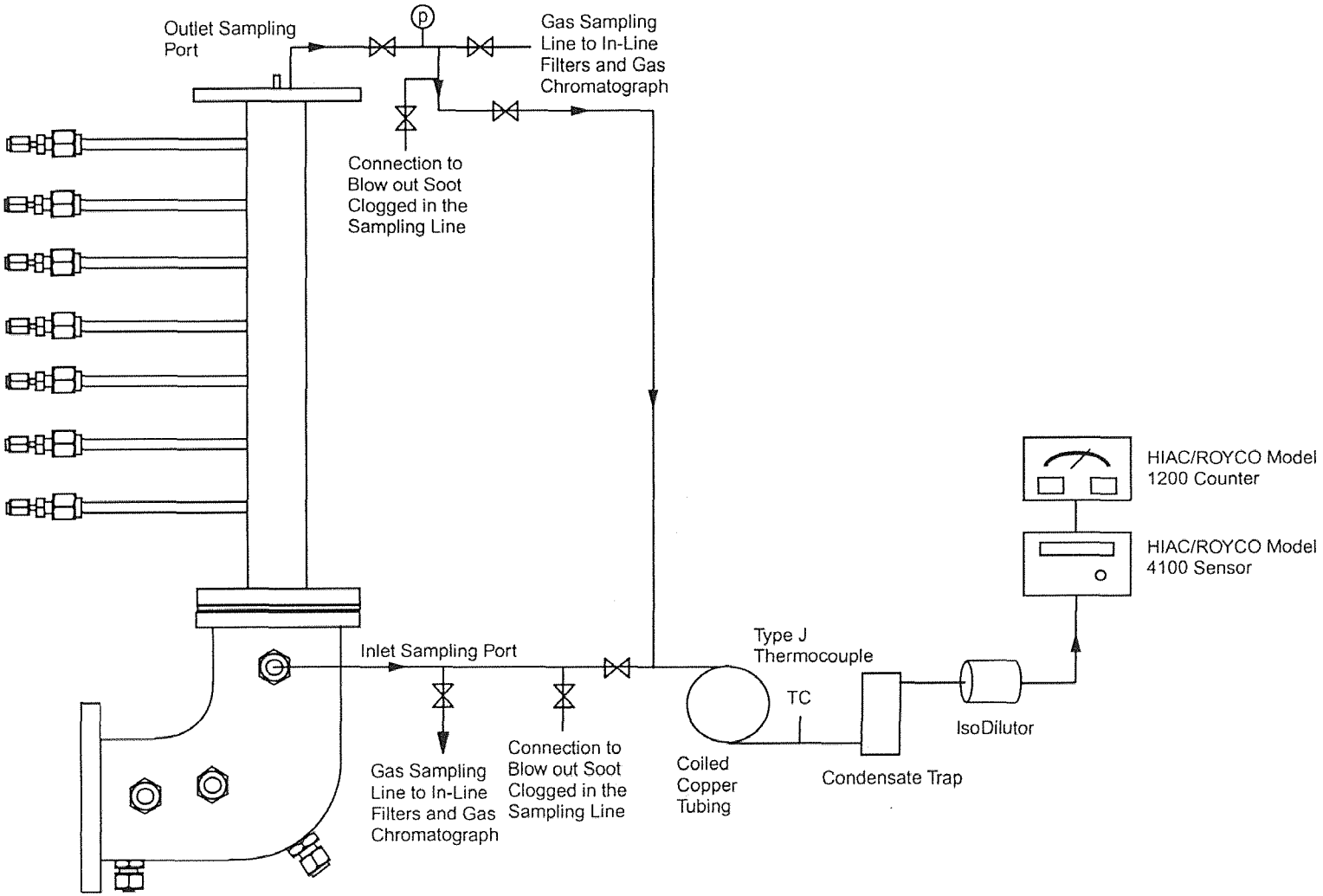

Figure 3.14 Particulate Sampling System Using a Particle Counter

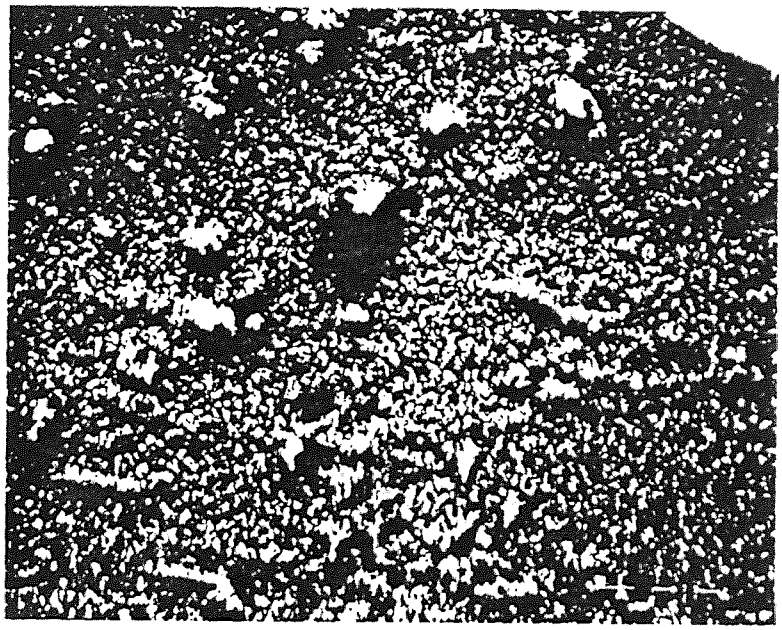

Figure 5.1 Soot Filter Sample Examined Using an Electron Microscope at 500X

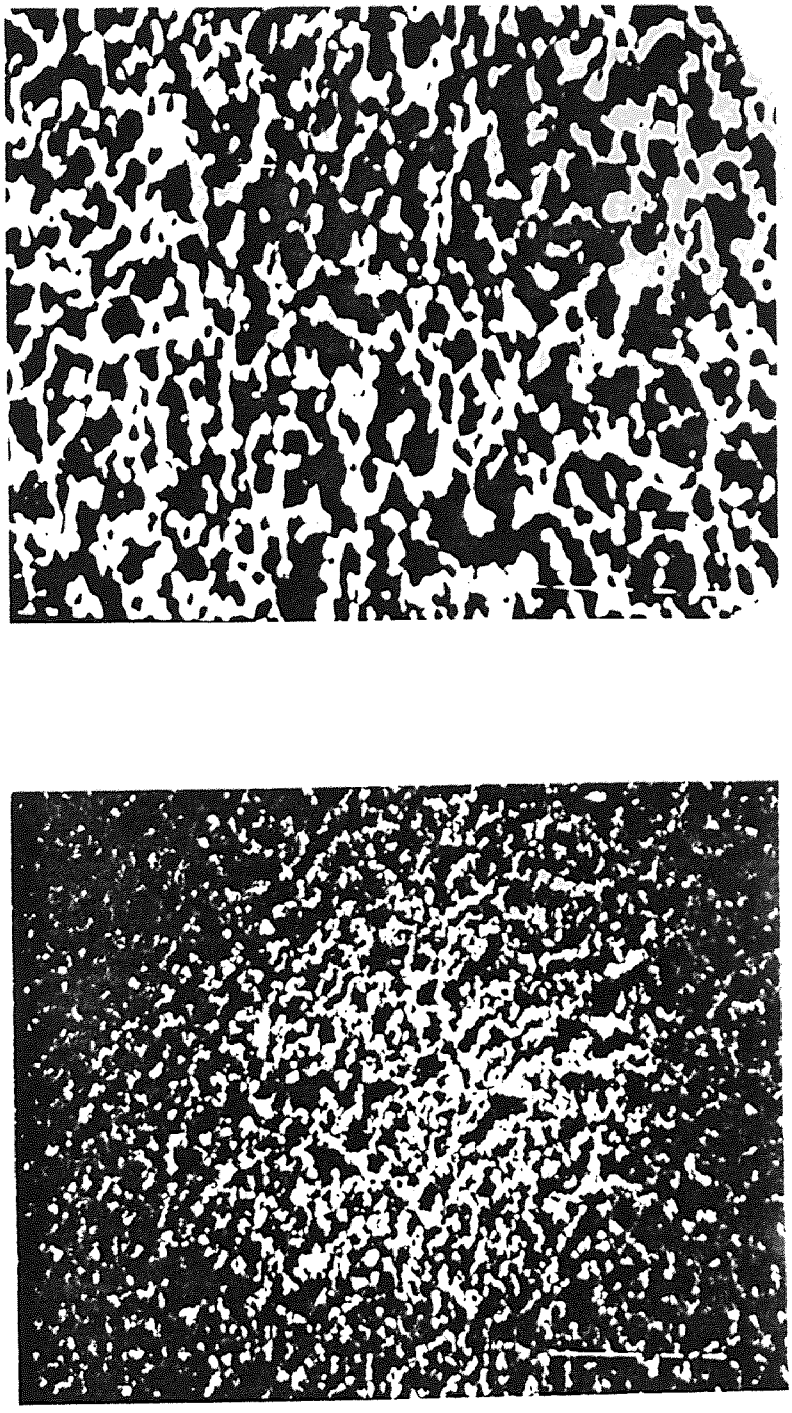

Figure 5.2 Comparison of a Blank Filter Paper (top) and Light Soot Filter Sample Using an Electron Microscope at 1000X

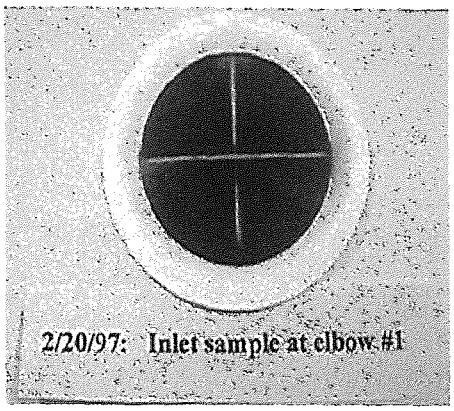

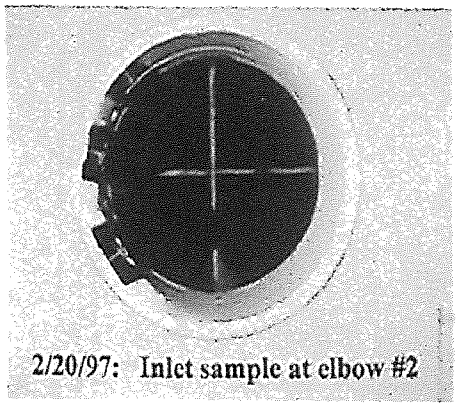

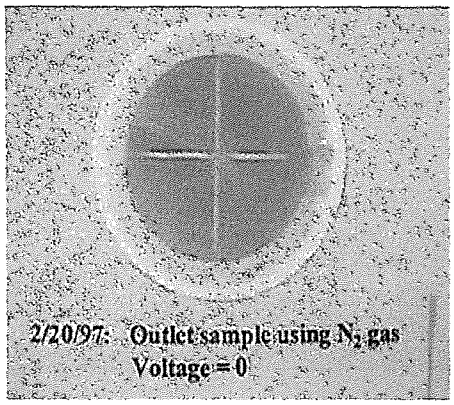

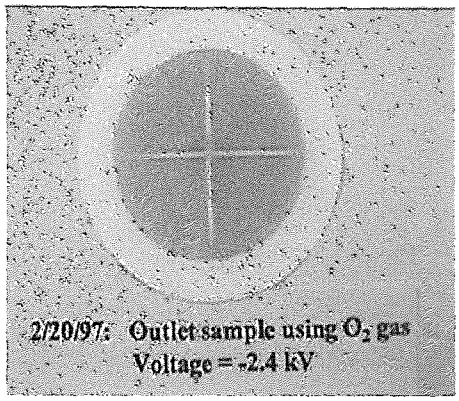

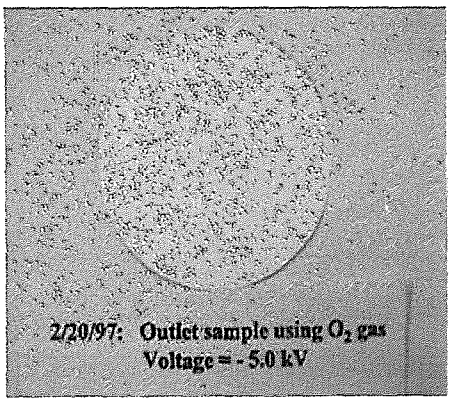

Figure 6.1 Filter Paper Samples with -2.5 and - 5.0 kV Applied (Light Soot Conditions)

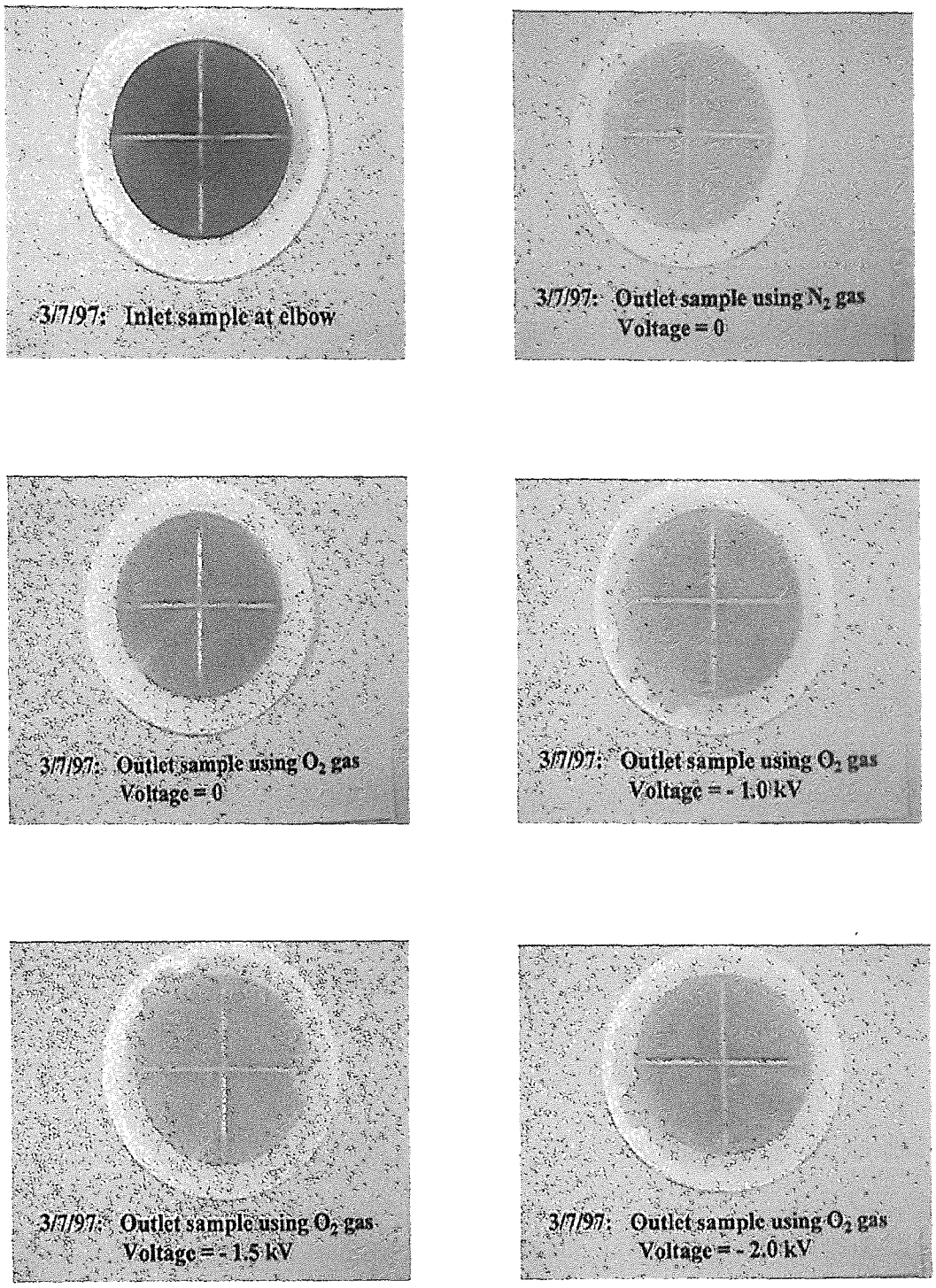

Figure 6.2 Filter Paper Samples with 0 to - 3.5 kV Applied (Light Soot Conditons)

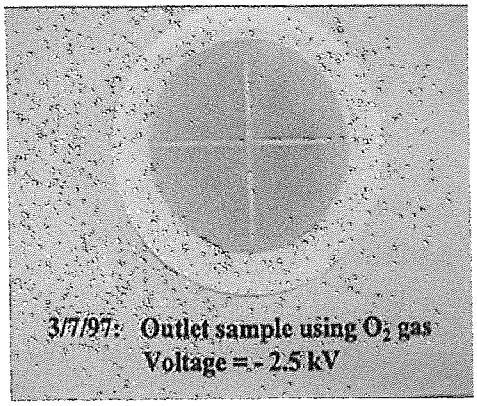

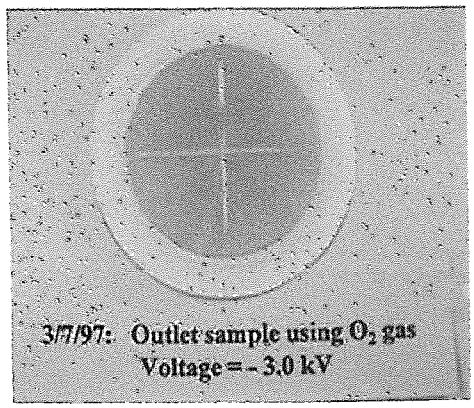

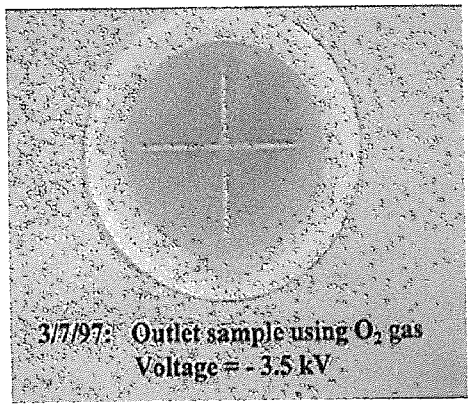

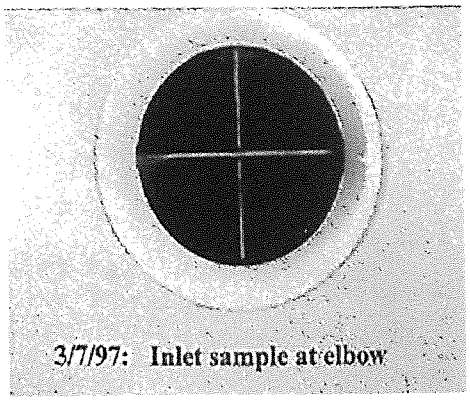

Figure 6.2 Continued

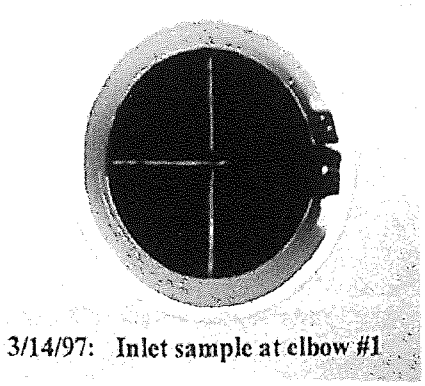

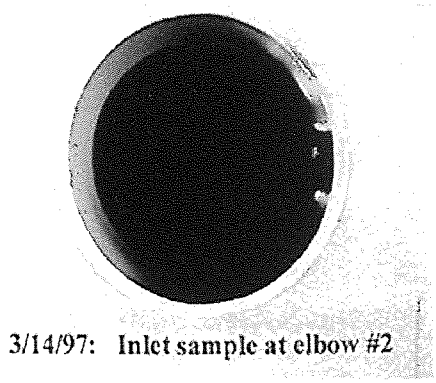

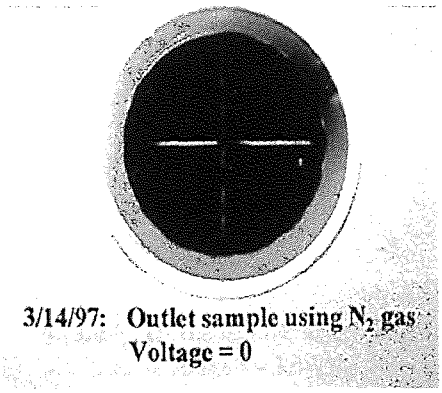

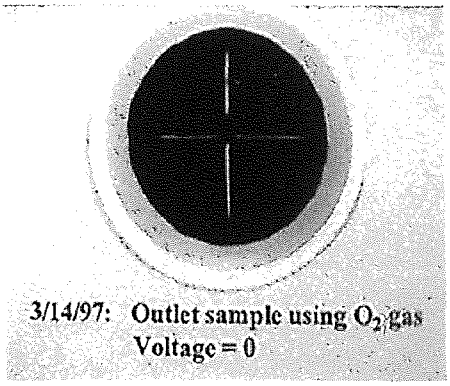

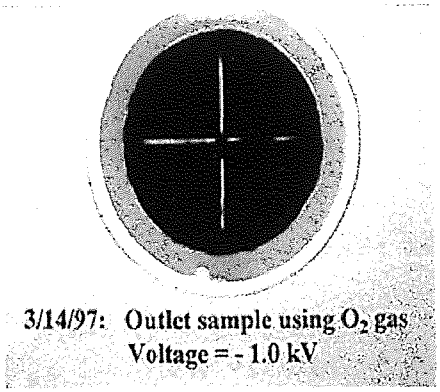

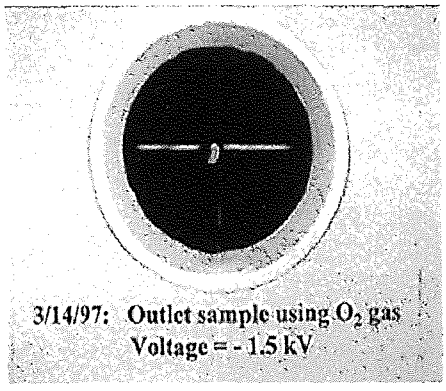

Figure 6.3 Filter Paper Samples with 0 - 5.0 kV Applied (Heavy Soot Conditions)

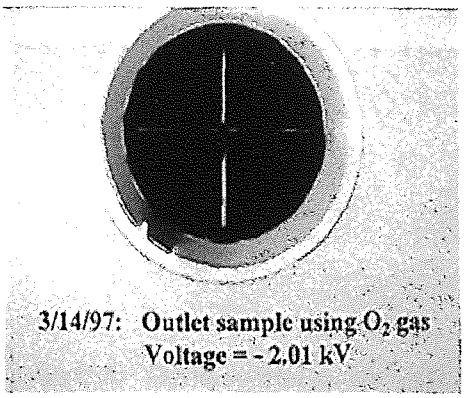

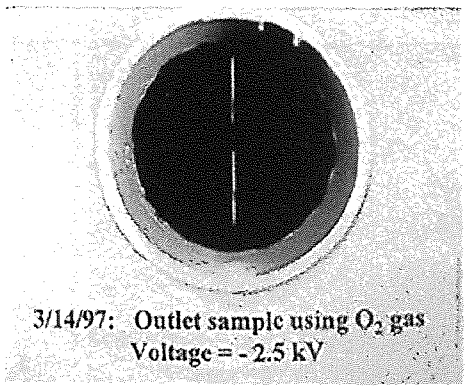

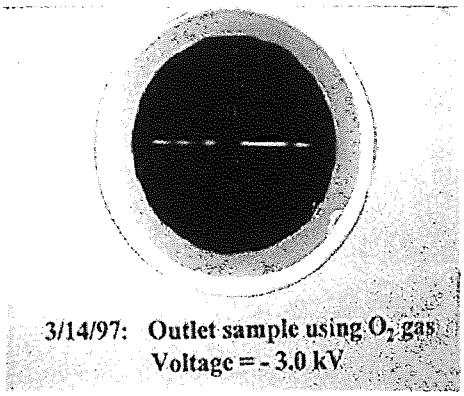

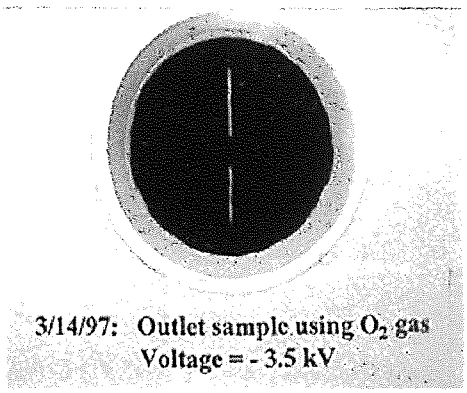

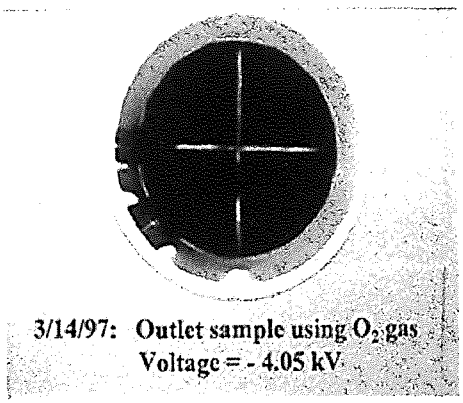

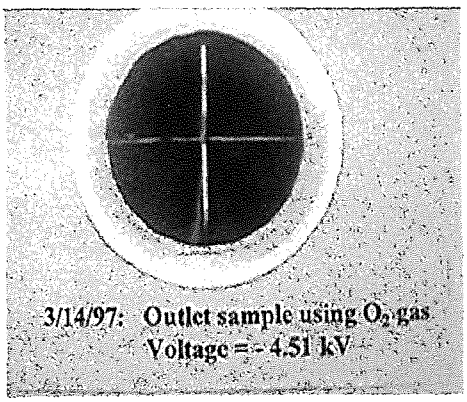

Figure 6.3 Continued

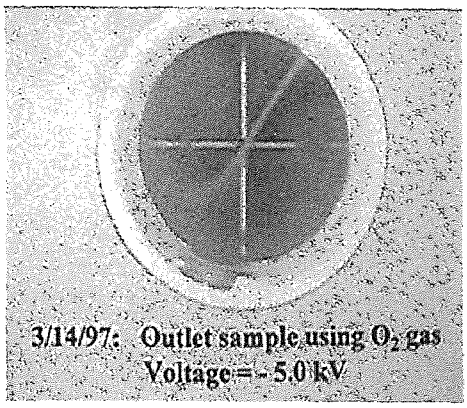

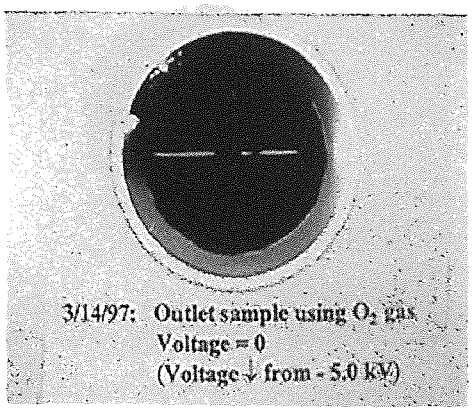

Figure 6.3 Continued

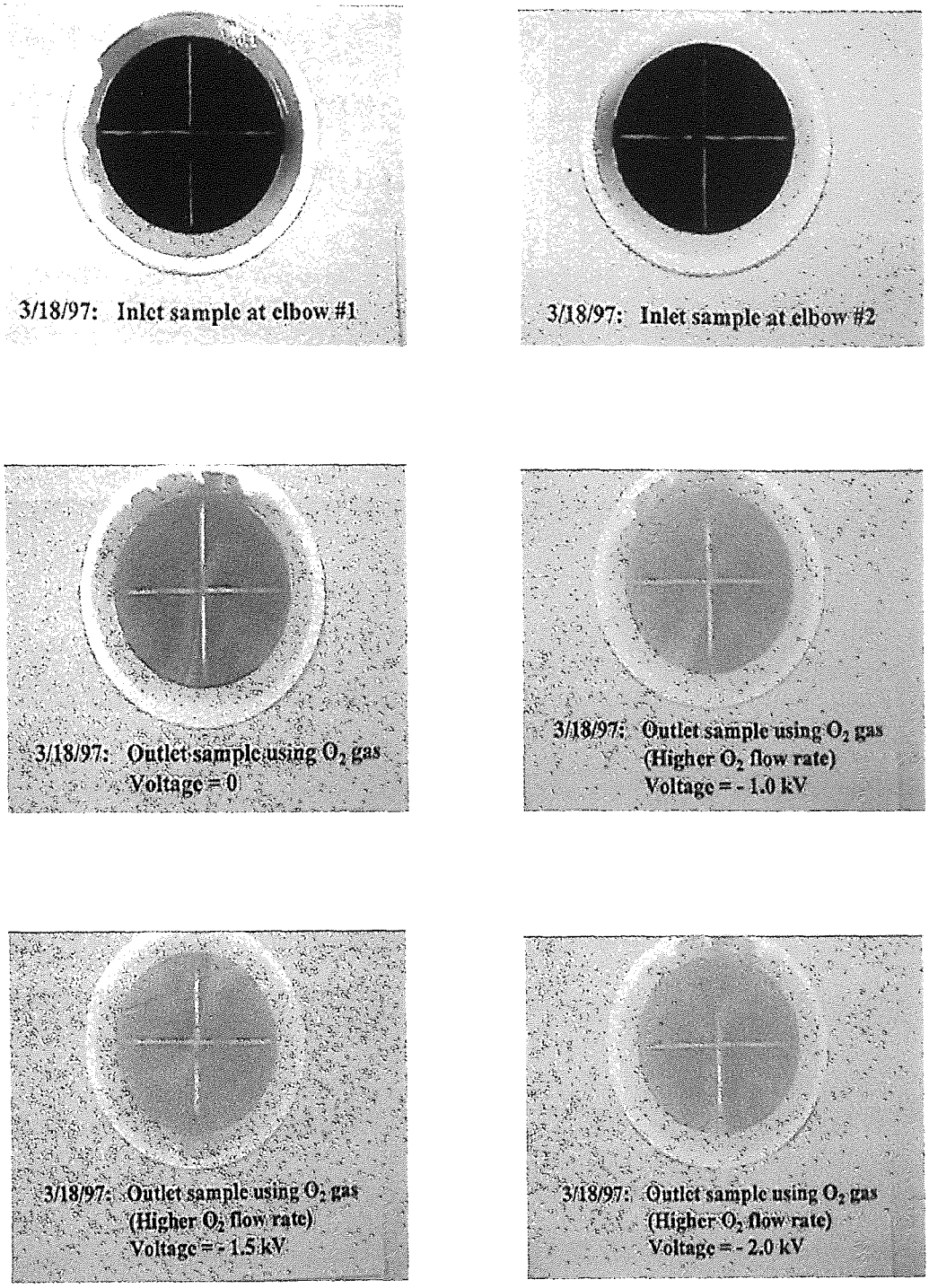

Figure 6.4 Filter Paper Samples with 0 - 5.0 kV Applied (Light Soot Conditions)

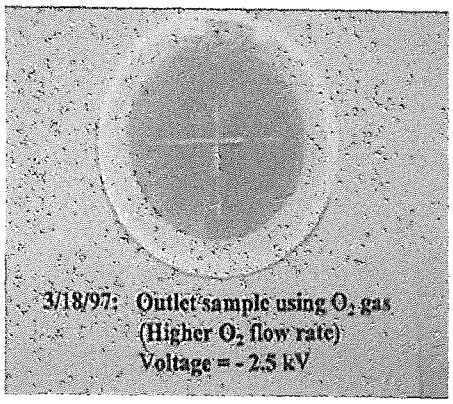

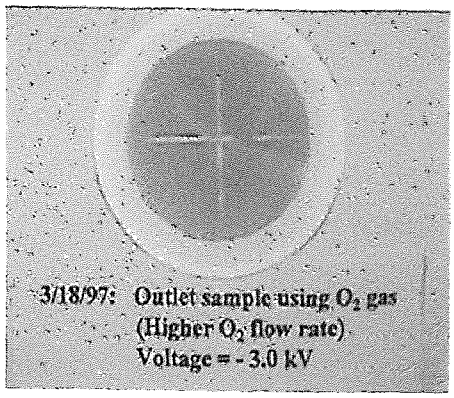

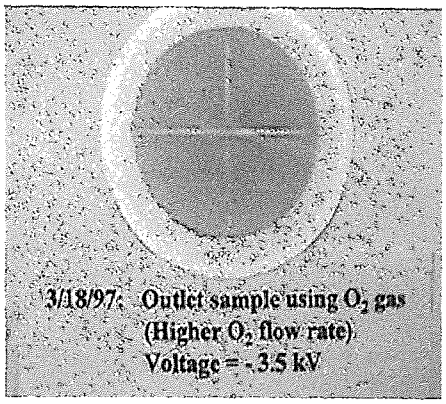

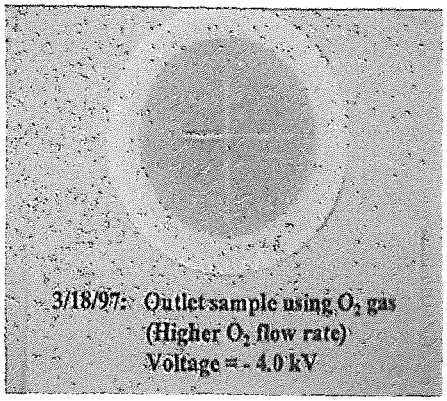

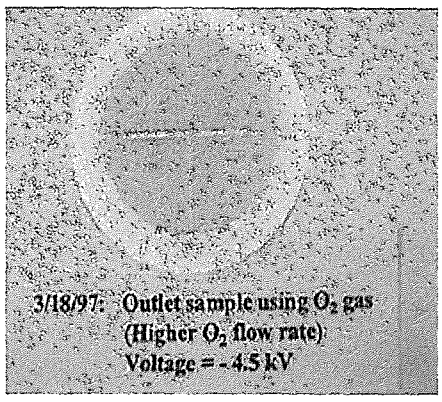

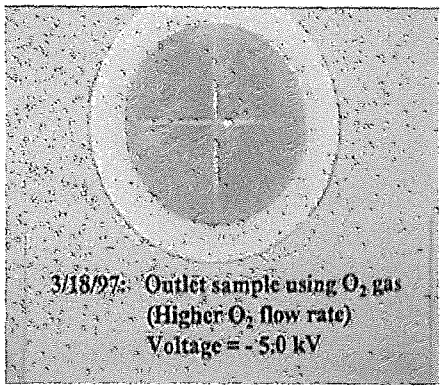

Figure 6.4 Continued

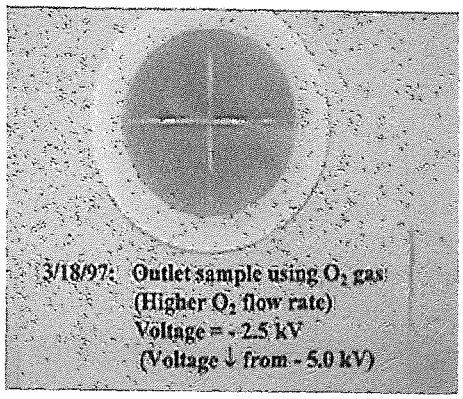

Figure 6.4 Continued

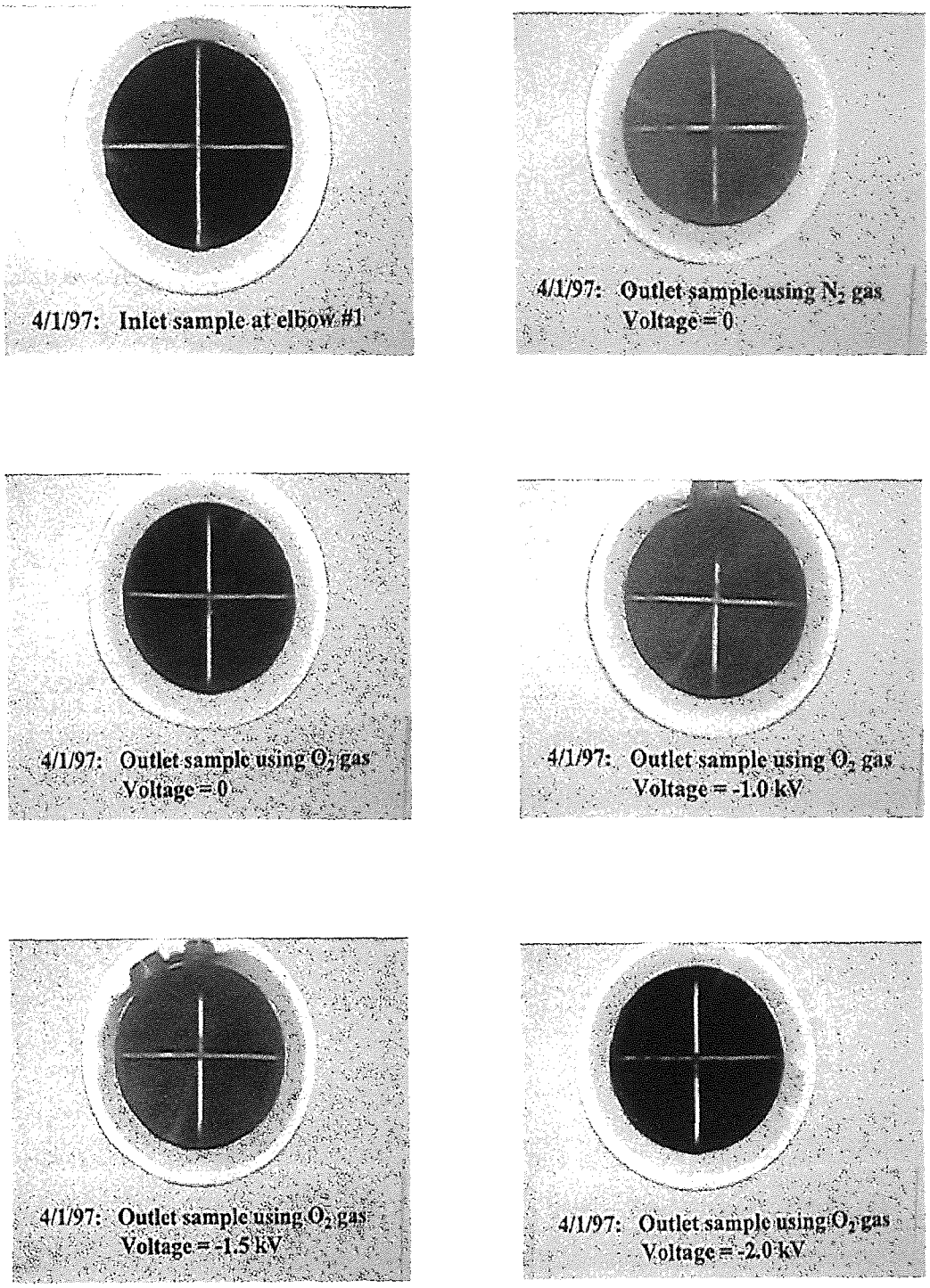

Figure 6.5 Filter Paper Samples with 0 - 5.0 kV Applied (Moderate Soot Conditions)

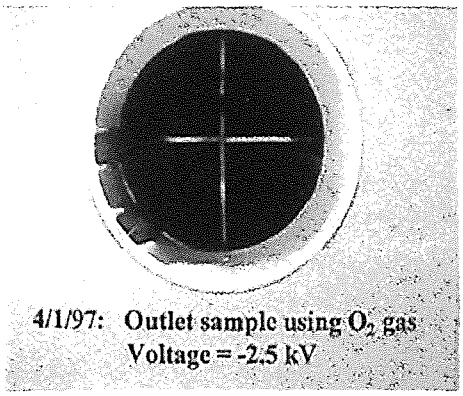

4/1/97: Outlet sample using O_2 gas
Voltage = -2.5 kV

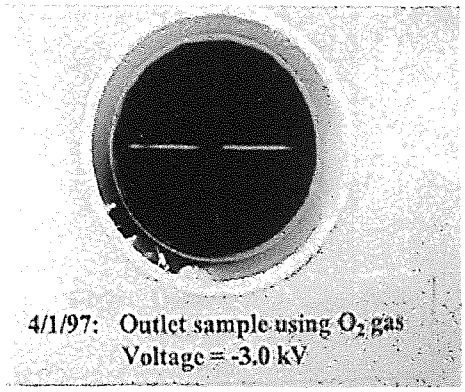

4/1/97: Outlet sample using O_2 gas
Voltage = -3.0 kV

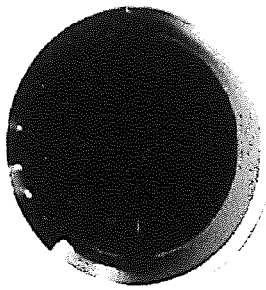

4/1/97: Inlet sample at elbow #2

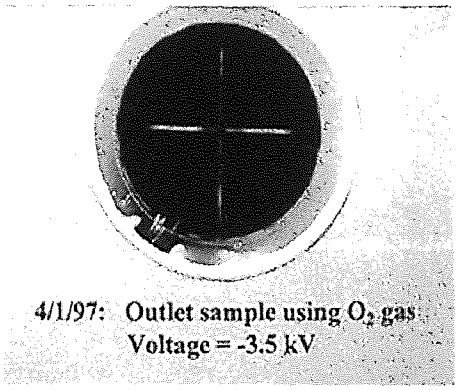

4/1/97: Outlet sample using O_2 gas
Voltage = -3.5 kV

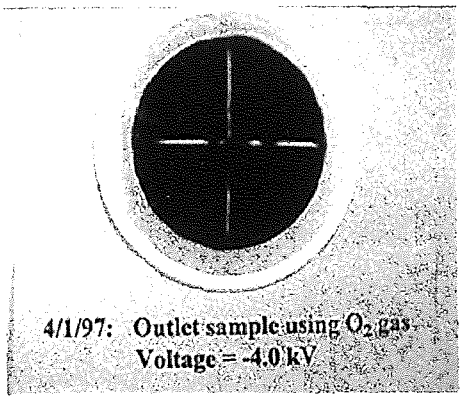

4/1/97: Outlet sample using O_2 gas
Voltage = -4.0 kV

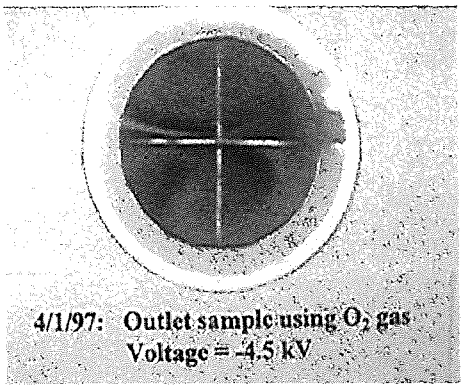

4/1/97: Outlet sample using O_2 gas
Voltage = -4.5 kV

Figure 6.5 Continued

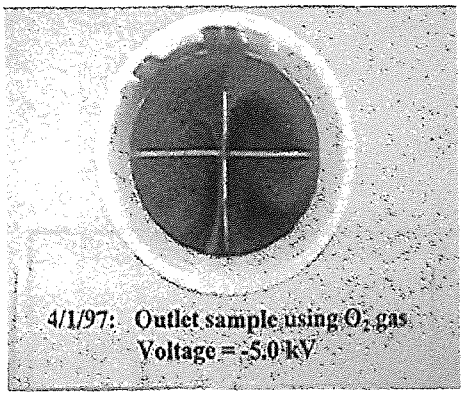

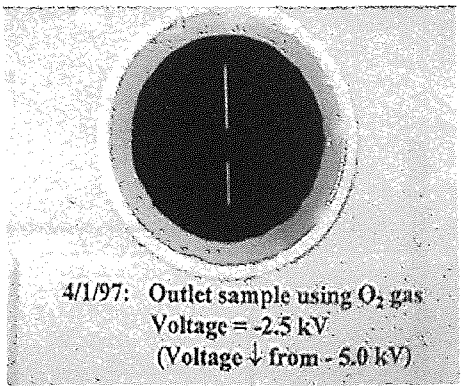

Figure 6.5 Continued

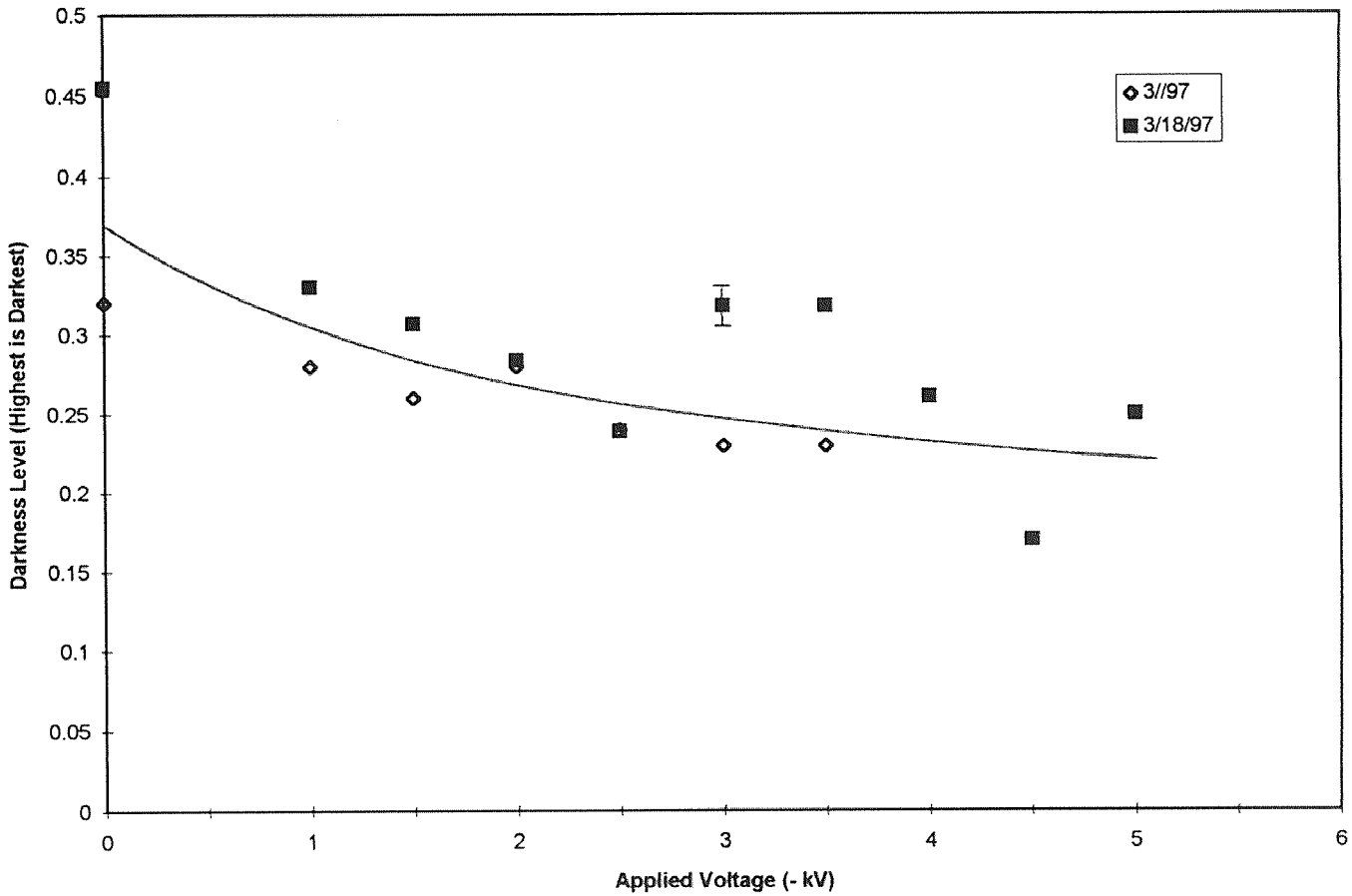

Figure 6.6 Plot of Darkness Levels of Outlet Filter Paper Samples as a Function of Applied Voltage During Light Sooting Conditions

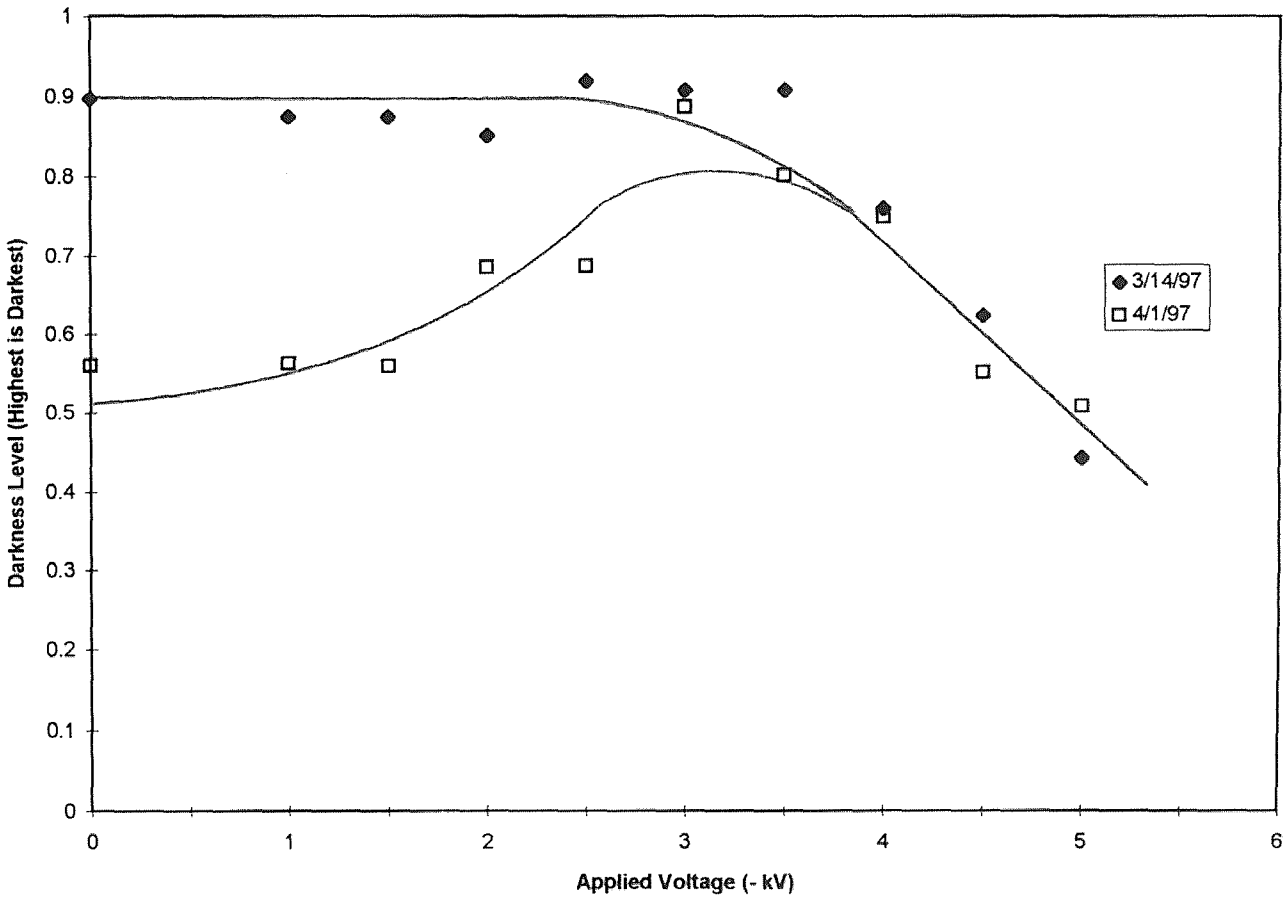

Figure 6.7 Plot of Darkness Levels of Outlet Filter Paper Samples vs Applied Voltage During Heavy Sooting Conditions

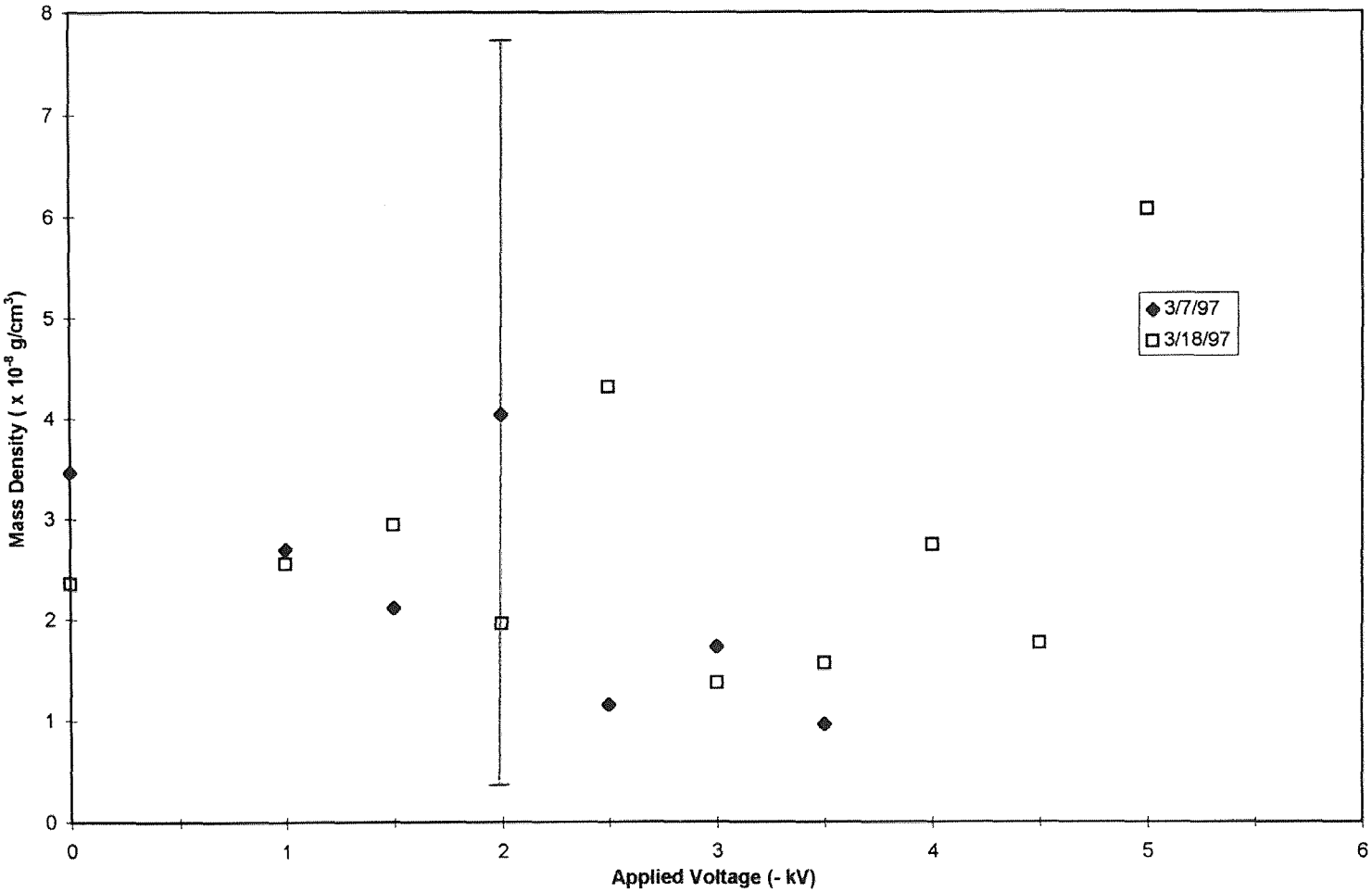

Figure 6.8 Mass Density of Outlet Filter Paper Samples Under Light Sooting Conditions as a Function of Applied Voltage

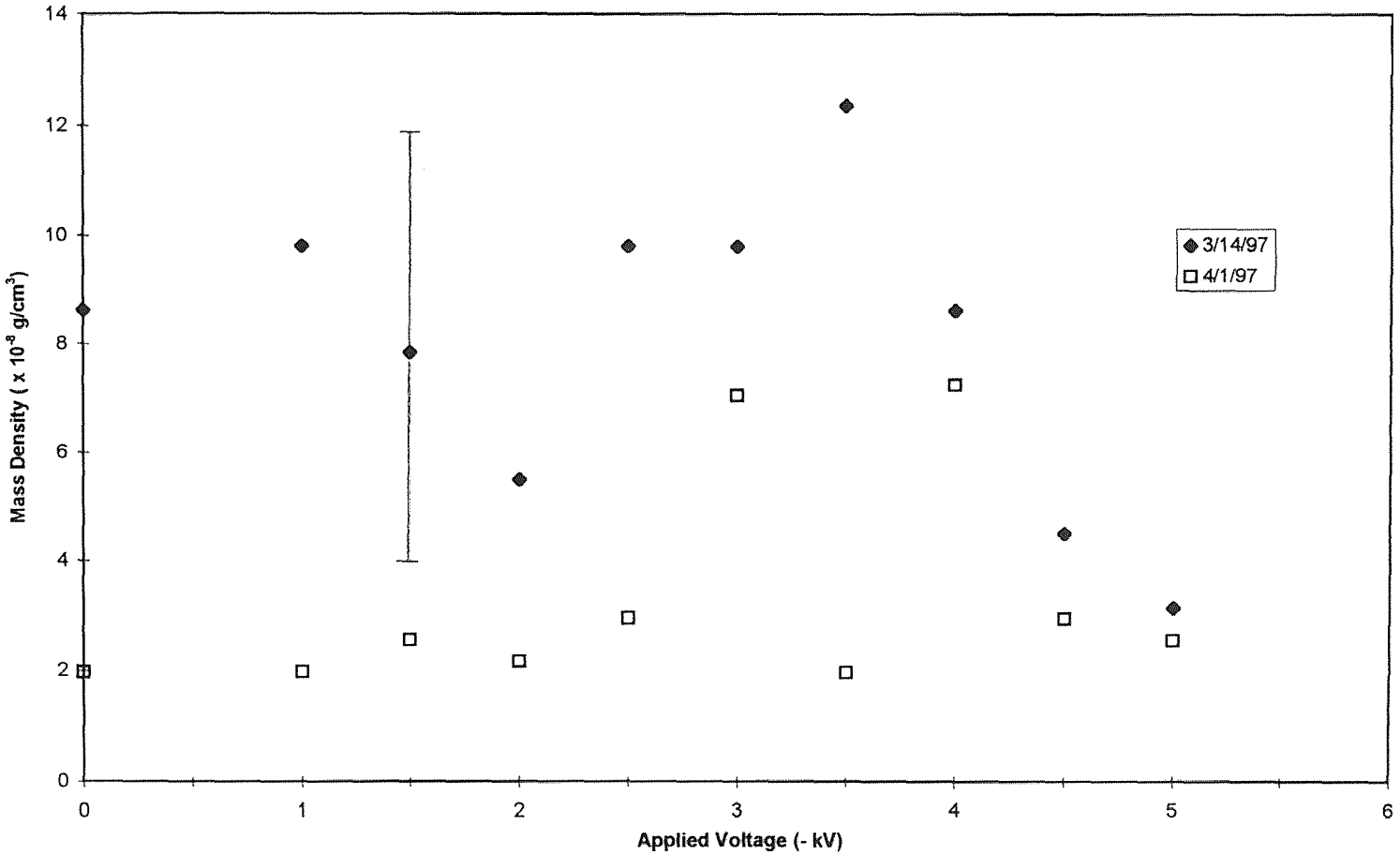

Figure 6.9 Mass Density of Outlet Filter Paper Samples Under Heavy Sooting Conditions as a Function of Applied Voltage

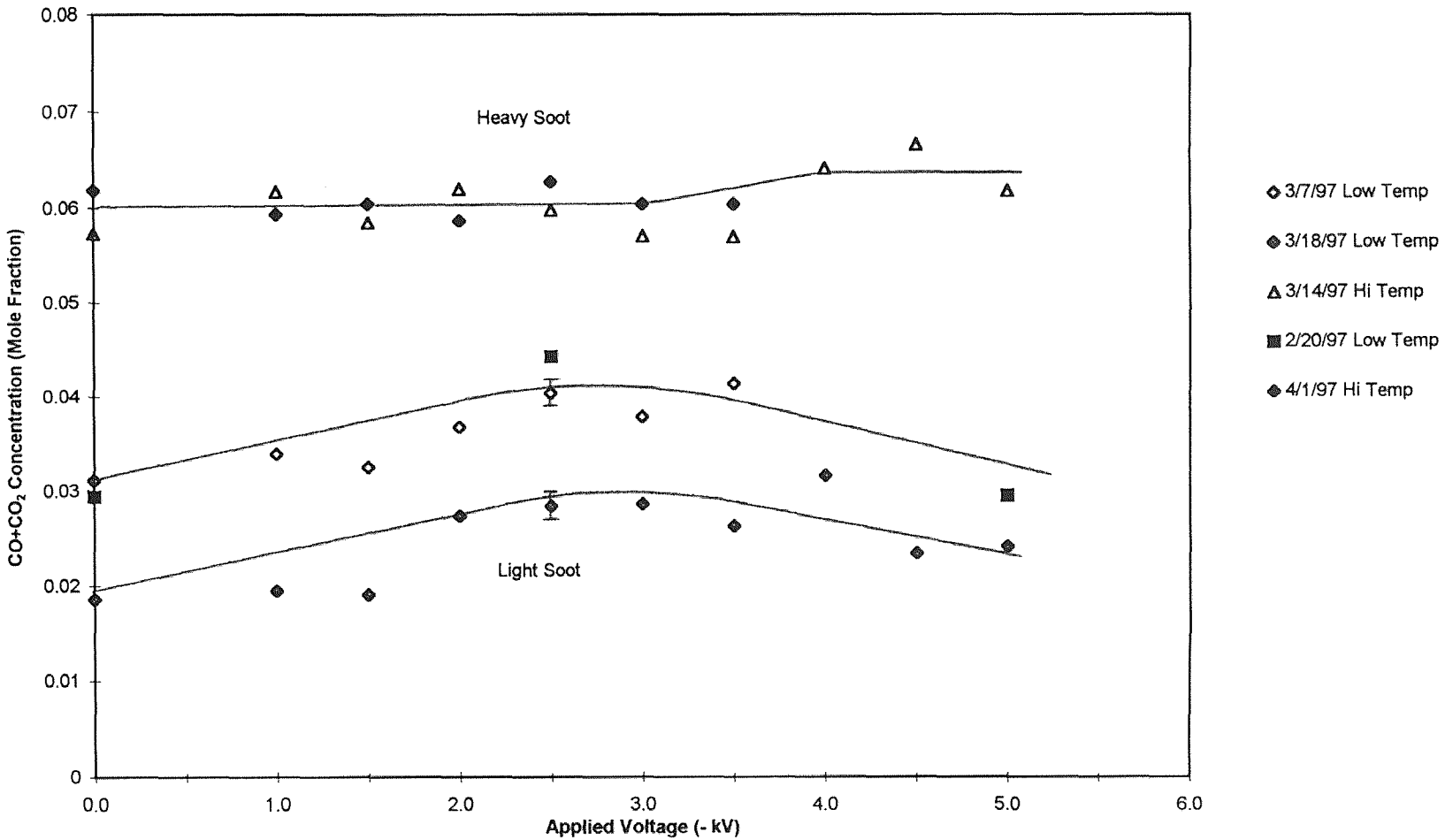

Figure 6.10 CO and CO_2 Concentration (Mole Fraction) as a Function of Applied Voltage for Both Light and Heavy Sooting Conditions

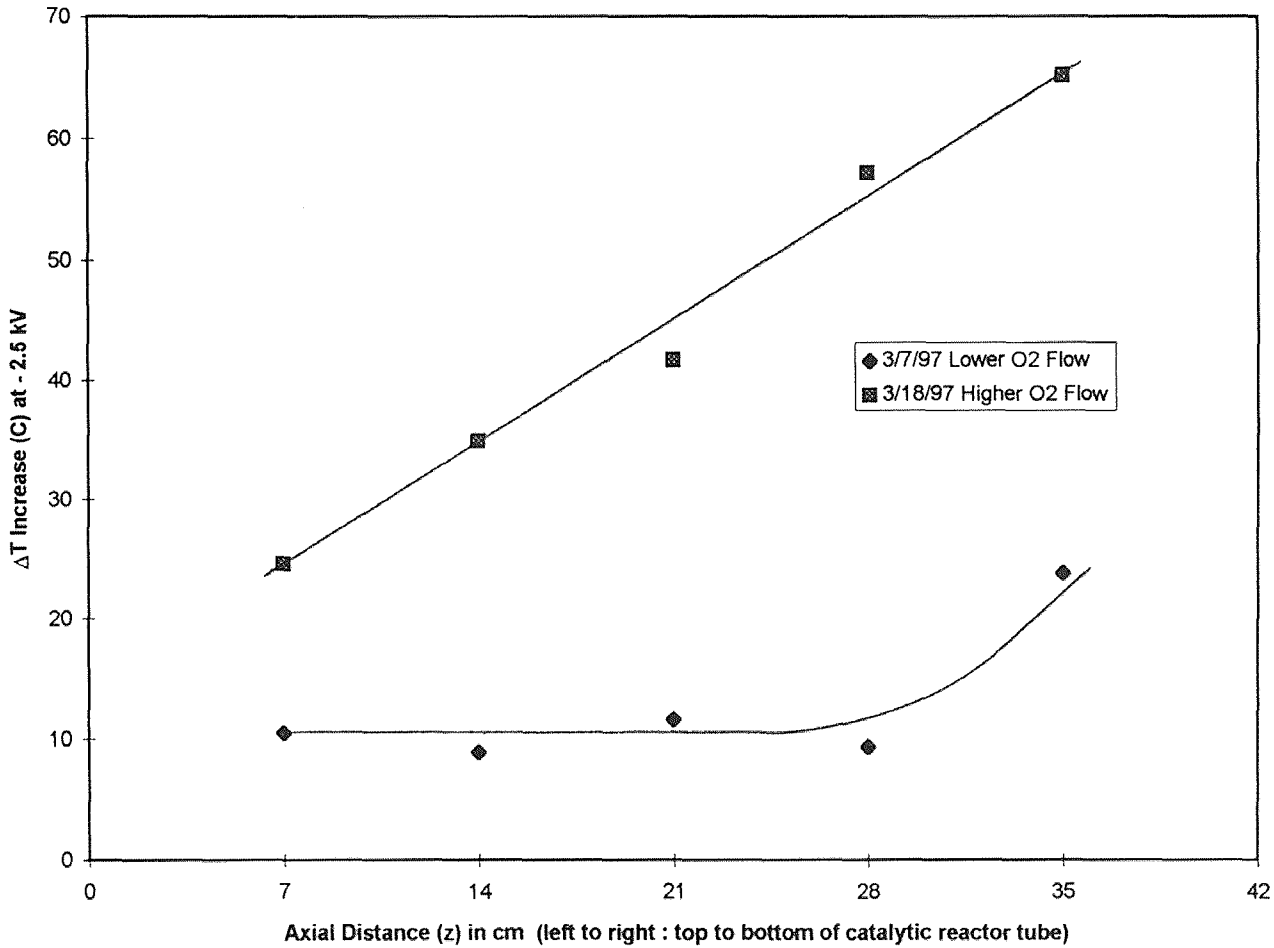

Figure 6.11 Plot of Increased Catalyst Surface Temperatures Measured from Average Temp with Nitrogen Gas and with Oxygen Gas at Applied Voltage of -2.5 kV

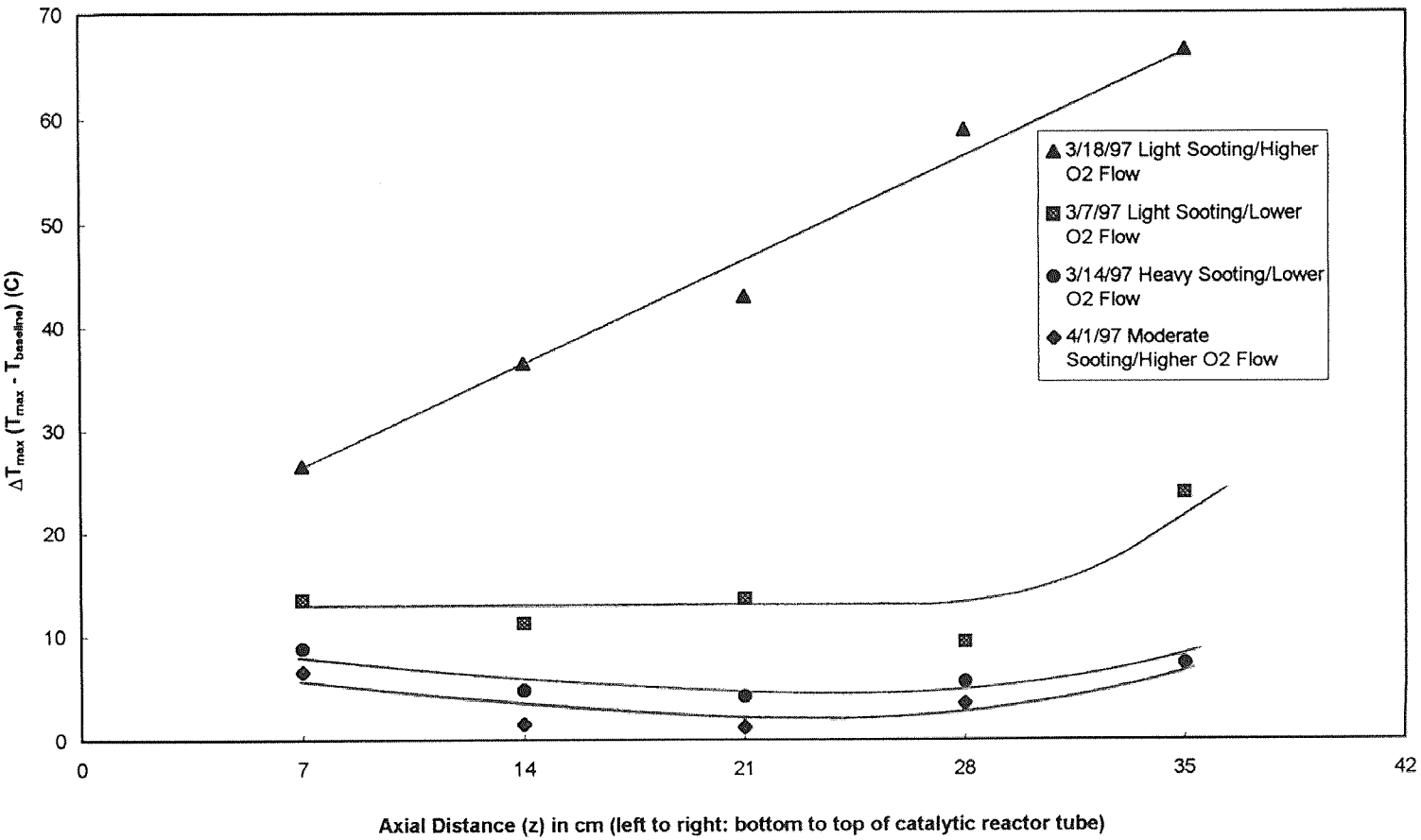

Figure 6.12 Plot of Maximum Catalyst Surface Temperature Increase vs Axial Distance of Data Taken

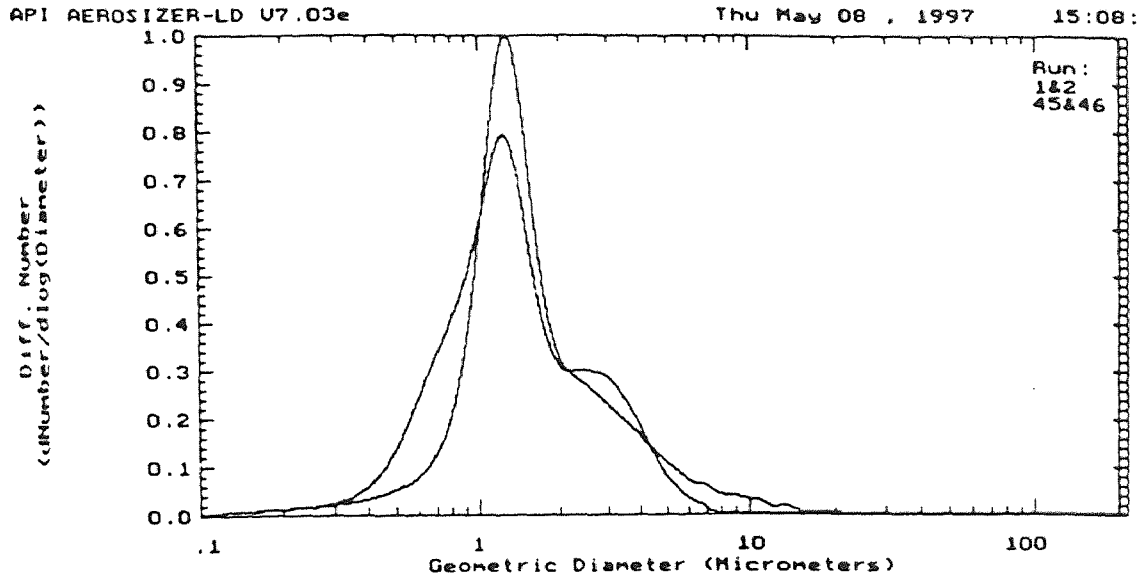

Figure 6.13 Particle Size Distribution for Exhaust Soot Taken at the Inlet of the Catalytic Reactor Tube Using the API Aerosizer

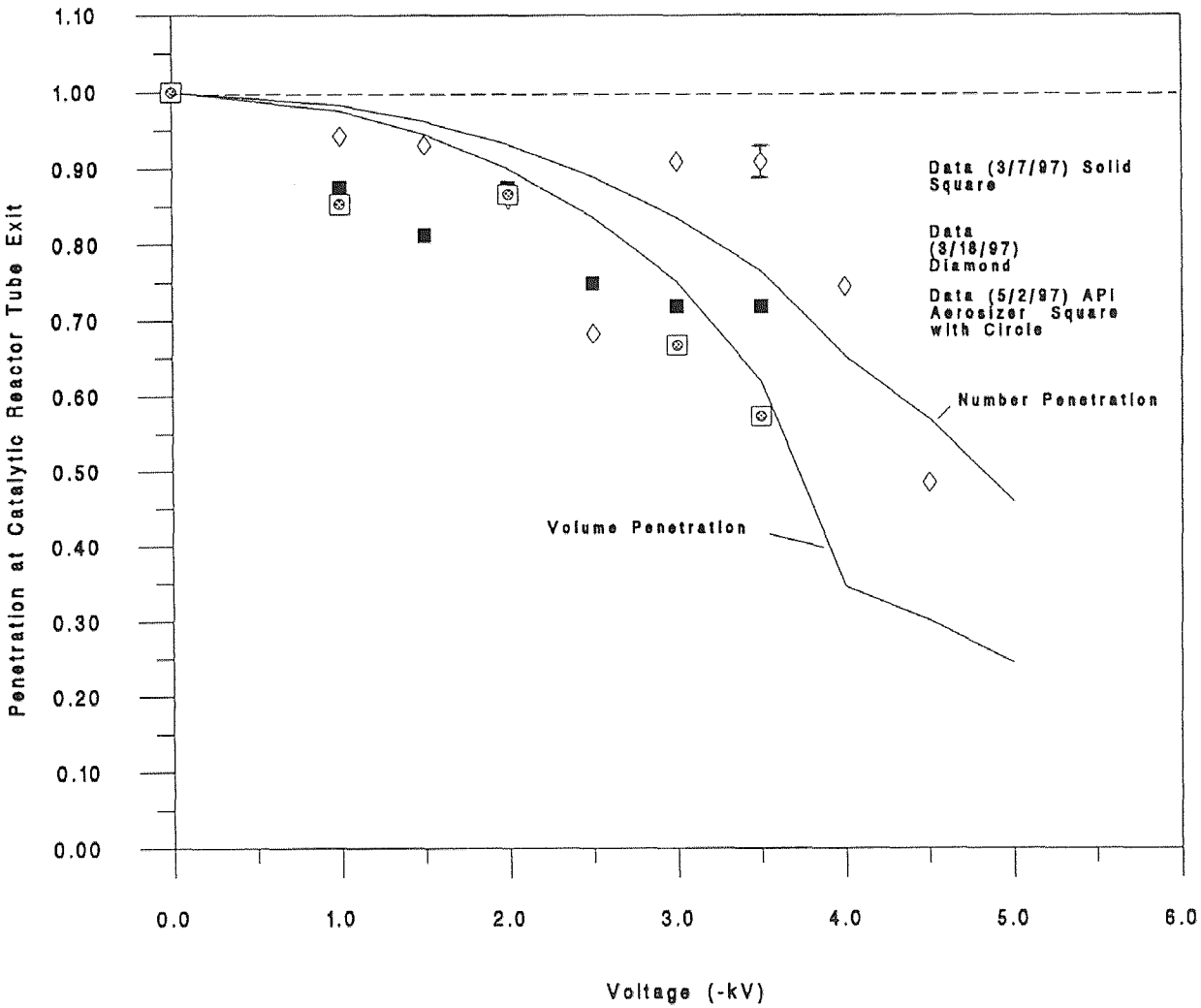

Figure 6.14 Penetration at Catalytic Reactor Tube Exit as a Function of Applied Voltage for Data Under Light Sooting Conditions and Two Fraction Model Using 35% Saturation Charge

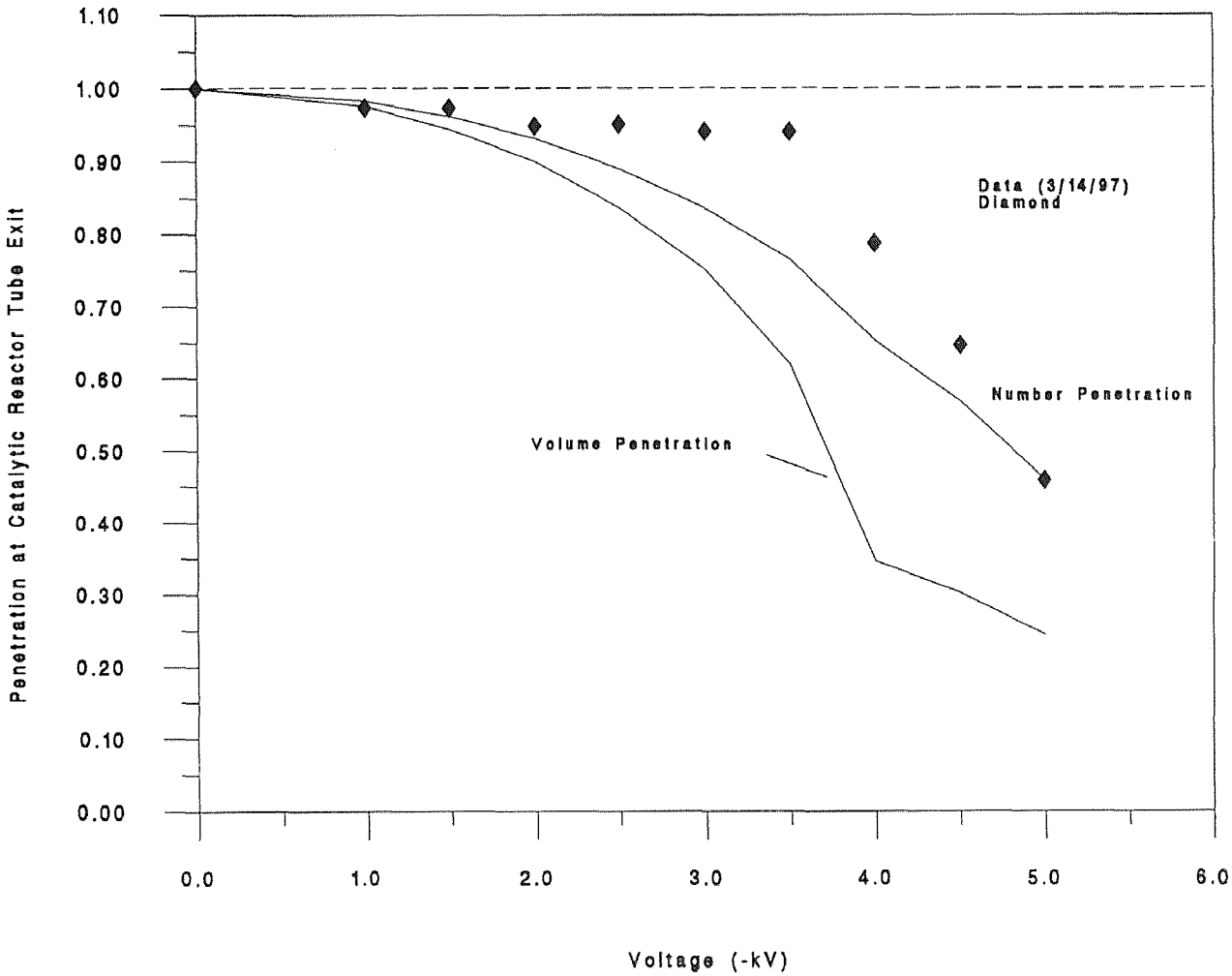

Figure 6.15 Penetration at Catalytic Reactor Tube Exit as a Function of Applied Voltage for Data Under Heavy Sooting Conditions and Two Fraction Model Using 35% Saturation Charge

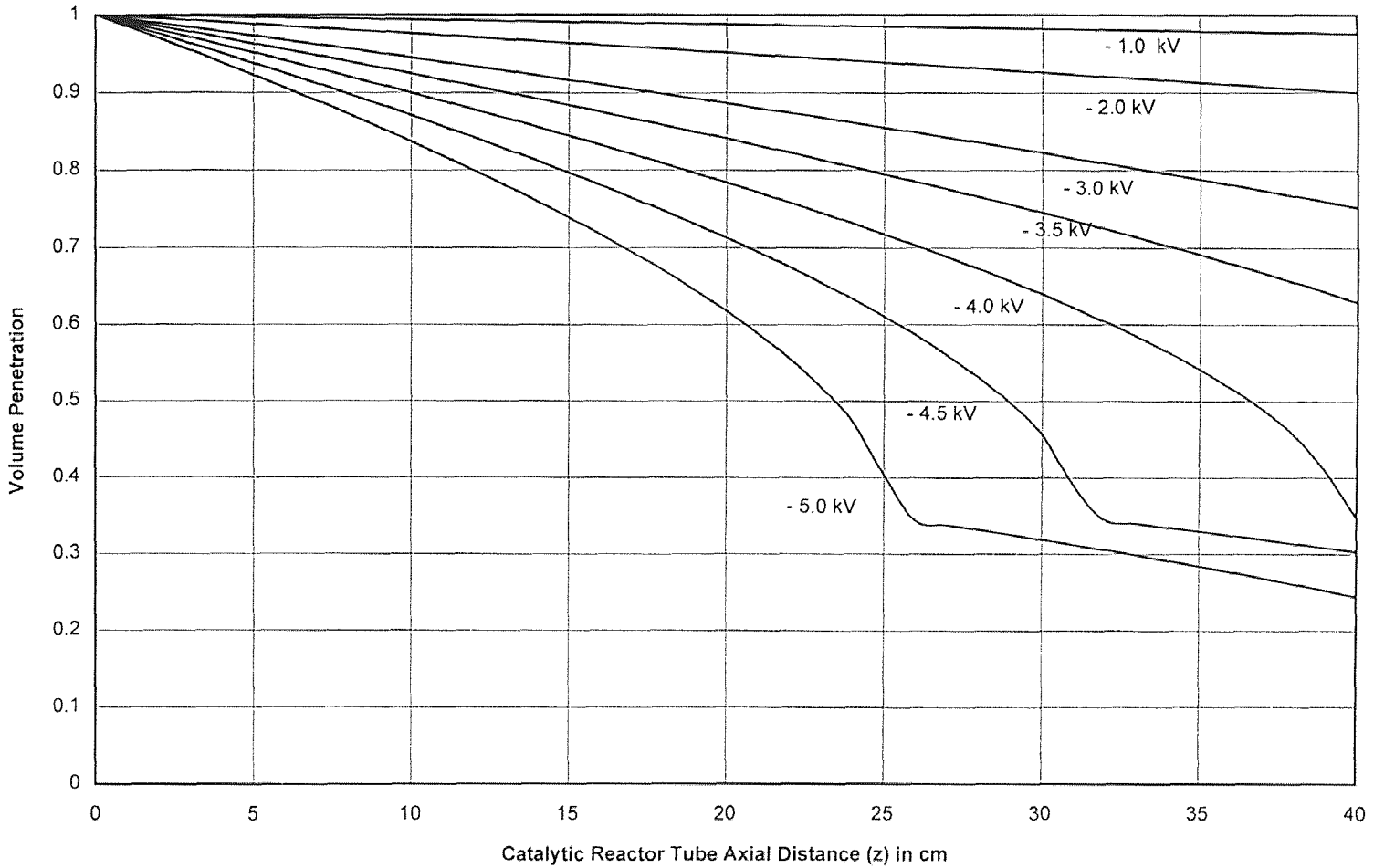

Figure 6.16 Volume Penetration Along the Reactor Tube Distance Z for Increasing Applied Voltage Using a Two Particle Size Distribution at 35% Saturation Charge

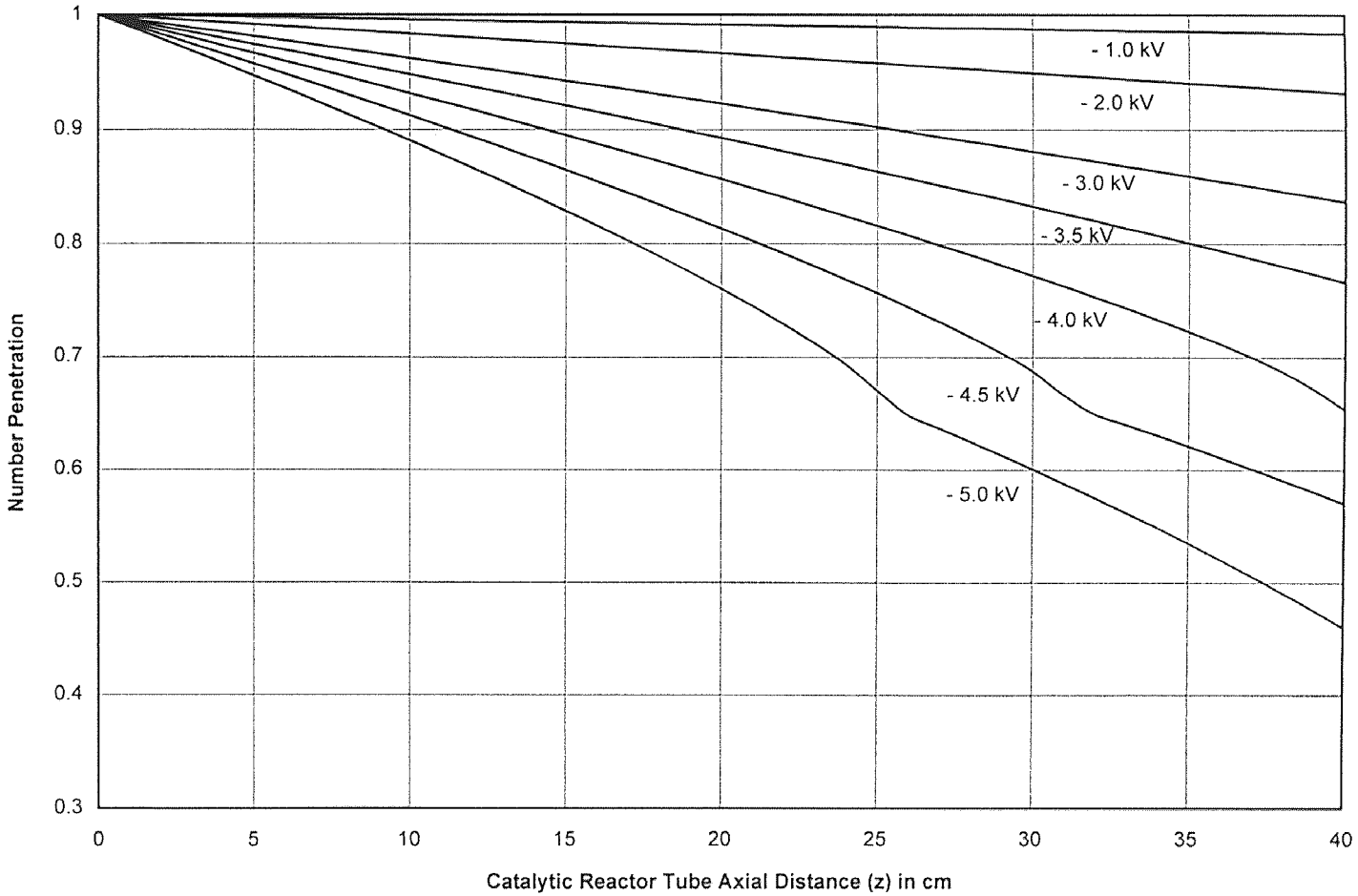

Figure 6. 17 Number Penetration Along the Reactor Tube Distance Z for Increasing Applied Voltage Using a Two Particle Size Distribution at 35% Saturation Charge

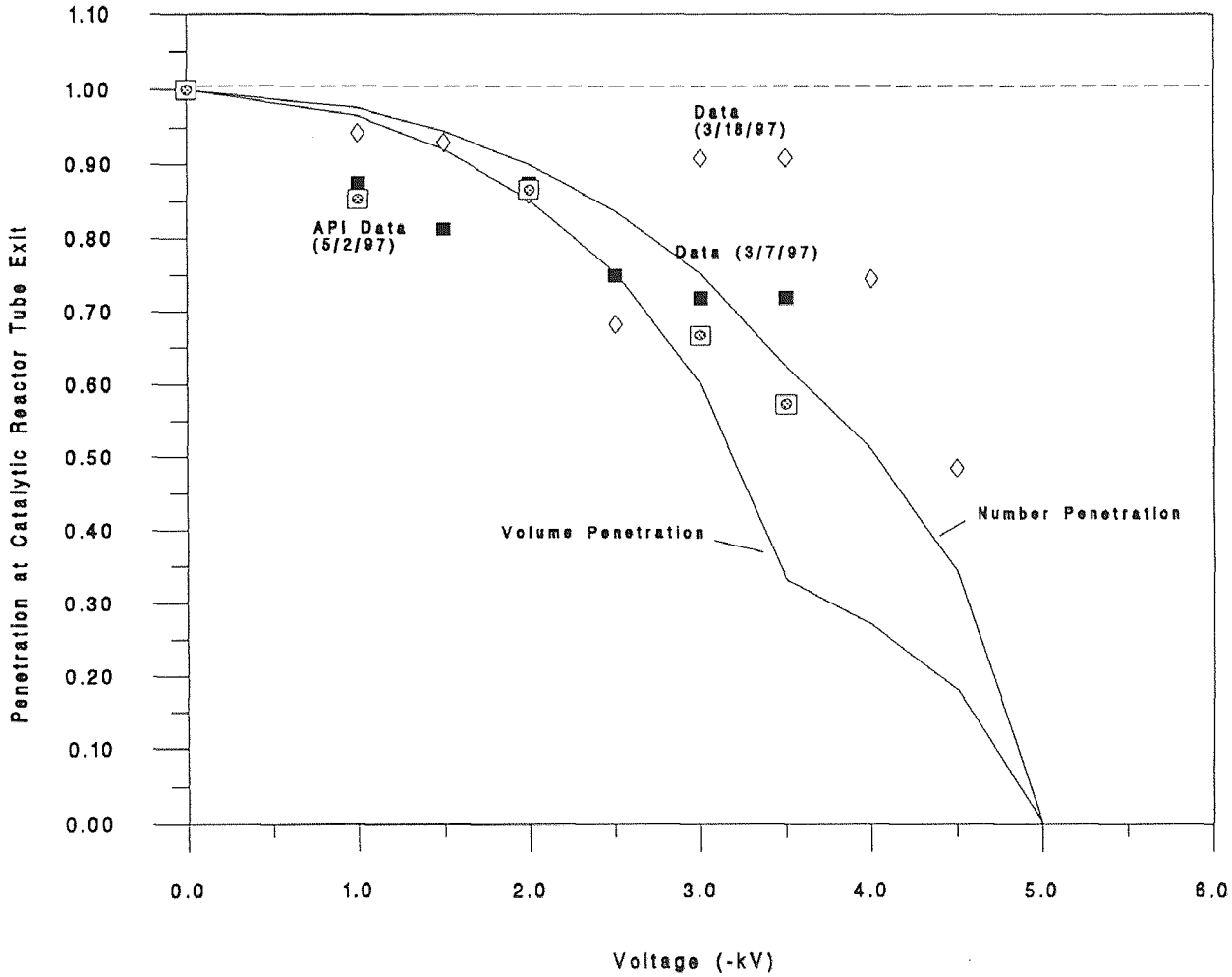

Figure 6.18 Penetration at Catalytic Reactor Tube Exit as a Function of Applied Voltage for Data Under Light Sooting Conditions and Two Fraction Model Using 50% Saturation Charge

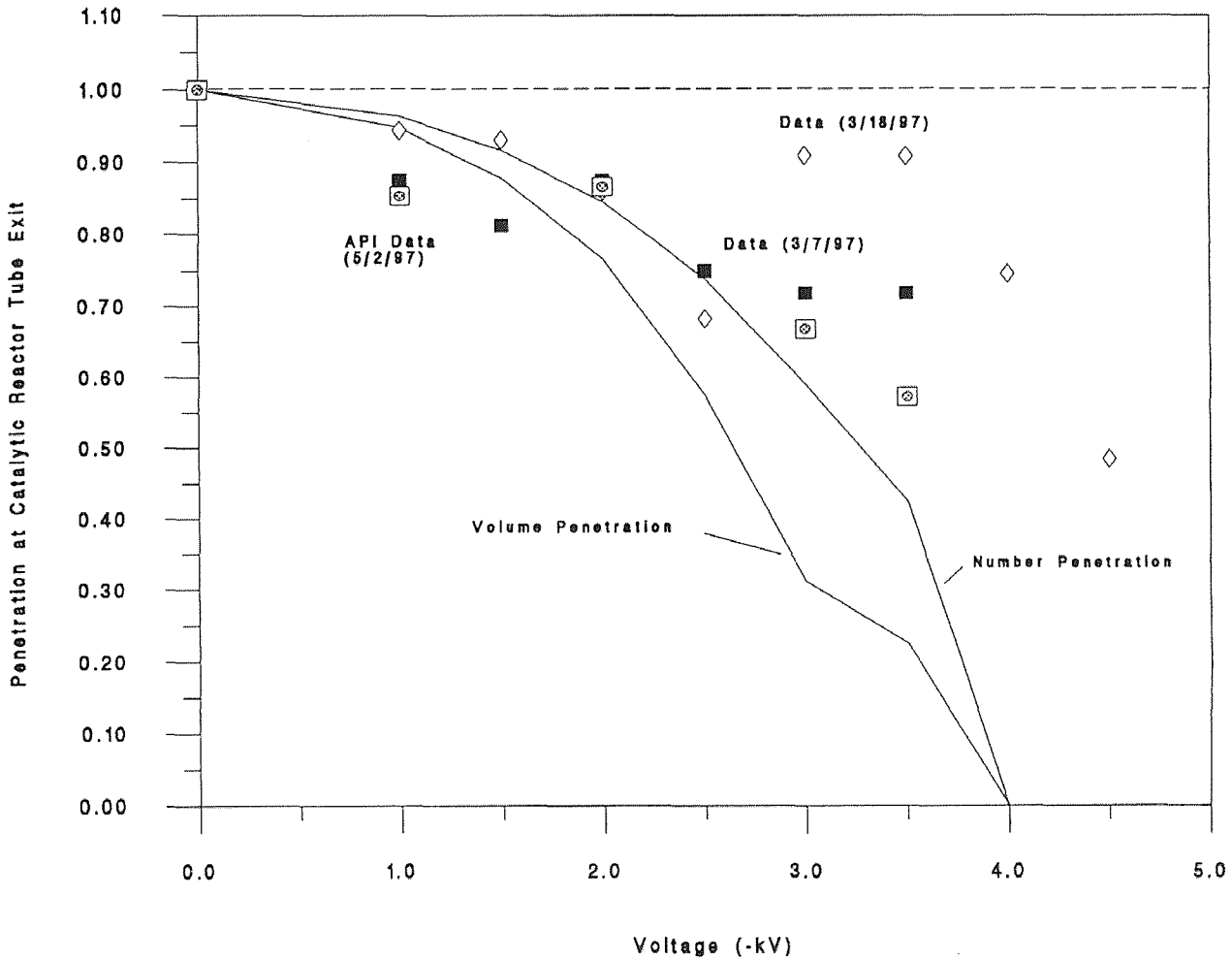

Figure 6.19 Penetration at Catalytic Reactor Tube Exit as a Function of Applied Voltage for Data Under Light Sooting Conditions and Two Fraction Model Using 75% Saturation Charge

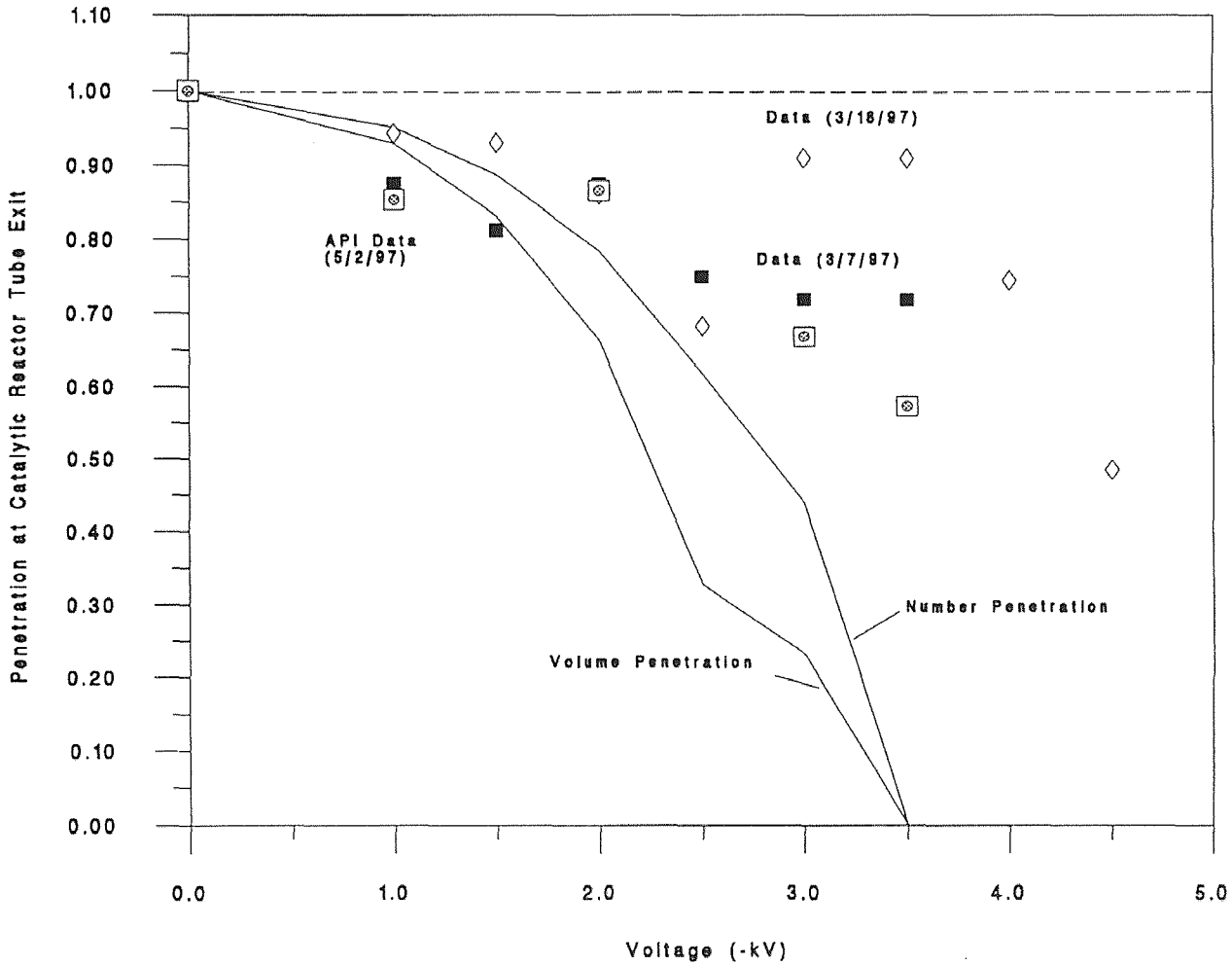

Figure 6.20 Penetration at Catalytic Reactor Tube Exit as a Function of Applied Voltage for Data Under Light Sooting Conditions and Two Fraction Model Using 100% Saturation Charge

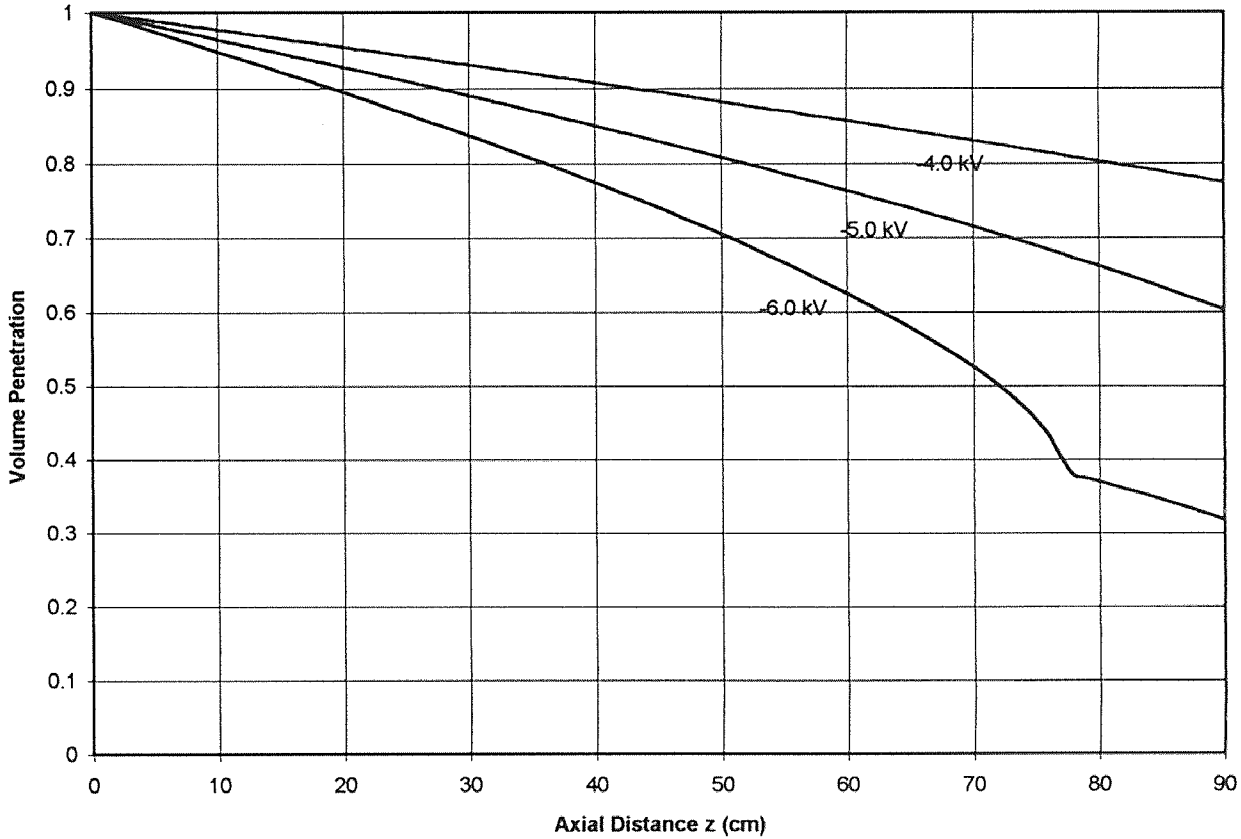

Figure 7.1 Volume Penetration as a Function of Axial Distance Using a 1.5" Diameter Tube and -4.0, -5.0 and -6.0 kV Applied Voltage

APPENDIX B

TOLUENE CONCENTRATION DERIVATION

Derivation of Toluene Concentration and Flow Rate Exiting the Gas Saturators or Bubblers

B.1 Purpose of Vaporized Toluene

Compressed air regulated to 1.4 psig and with a flow rate of about 360 cc/min acts as the carrier gas used in bubbling through liquid toluene in two partially filled enclosed flasks. The two flasks are placed in series and immersed in an isothermal (0 °C) ice bath. The purpose of using vaporized toluene is to simulate its effect as a surrogate for SOF. Toluene is the reagent gas and is carried by the air into the elbow section where it then flows into the catalyst lined reactor tube. The intended function of the toluene is to adsorb itself onto the soot particles so that it may enhance catalytic oxidation once the particles are captured on the catalyst active sites.

B.2 Derivation of Toluene Concentration and Flow Rate

To derive the equations for toluene concentration and flow rate into the reactor, several assumptions are made for conditions existing in the bubblers.

(1). Vapor/liquid equilibrium phase (VLE) conditions exist.

(2). Vapor acts as an ideal gas.

(3). Liquid toluene is a pure substance (liquid is 99.97 % pure).

(4). Total pressure is very low (near atmospheric conditions).

We begin with the isofugacity criterion which states that:

$$\hat{f}_i^{vapor} = \hat{f}_i^{liquid} \qquad \text{Smith and Van Ness (1987)} \qquad \text{(EB.1)}$$

where $\hat{f}_i^{vapor}$ is the fugacity of species i in the vapor mixture, and $\hat{f}_i^{liquid}$ is the fugacity of species i in the liquid solution.

Since the vapor is assumed to be an ideal gas, $\hat{f}_i^{vapor} = y_i P$ where y_i is the mole fraction of the gas and P is total pressure. In addition, the liquid composition is only toluene so the i^{th} species simply refers to toluene. Equation (EB.1) $\hat{f}_i^{liquid}$ is rewritten as:

$$\left(\frac{f_R^l}{f_R^{sat}}\right)\left(\frac{f_R^{sat}}{P_R^{sat}}\right)P_R^{sat} = y_R P \qquad \text{(EB.2)}$$

where P_R^{sat} is the vapor pressure of the reagant gas, R stands for the reagent gas (toluene) and l is the liquid phase of the reagent, and *sat* refers to saturated conditions. The first factor on the left hand side of (EB.2) is the Poynting Factor and is written as:

$$\left(\frac{f_R^l}{f_R^{sat}}\right) = \exp\left[\frac{V_R^l(P - P_R^{sat})}{RT}\right] \qquad \text{Smith and Van Ness (1987)} \qquad \text{(EB.3)}$$

The second term on the left hand side of (EB.2) is definition of the fugacity coefficient (ϕ) where:

$$\phi_i^{sat} = \phi_i^l \text{ (because of pure species)} = \exp\left[\int_0^{P_i^{sat}} (Z-1)\frac{dP}{P}\right] \qquad \text{(EB.4)}$$

for constant temperature and composition (Smith and Van Ness (1987)). For very low pressures, the difference P^{sat}-P (or zero pressure) is nearly zero, so the exponentials $\rightarrow 1$, and (EB.2) reduces to:

$$P_R^{sat} = y_R P \text{ or } y_R = \frac{P^{sat}}{P} \qquad \text{(EB.5)}$$

Therefore, the concentration of toluene (y_R) expressed as a mole fraction is dependent on the saturation (vapor) pressure (P^{sat}) and total pressure (P). Because the bubblers are

partially submerged in an ice bath, y_R will be slightly less because the partial pressure at the bubbler exit will be lower than P^{sat} according to Holstein (1994).

The saturation pressure is calculated by the use of Antoine's equation in the form of:

$$\log_{10} P^{sat} = A - \frac{B}{t + C} \tag{EB.6}$$

where A, B, and C are Antoine's coefficients for the reagent and t is temperature in °C. For toluene $A = 6.95805$, $B = 1346.773$, and $C = 219.693$ from Boublik, et al. (1973).

Molar flow rates exiting the bubblers are defined as:

$$F_{total} = F_{reagent} + F_{carrier\ gas} \tag{EB.7}$$

The molar flow rate of the reagent is defined in terms of total flow rate as:

$$F_{reagent} = y_R F_{tot} \tag{EB.8}$$

Rearrangement of (EB.7) and inserting (EB.5) for y_R results in:

$$F_{reagent} = F_{carrier\ gas}\left(\frac{P^{sat}}{P - P^{sat}}\right) \tag{EB.9}$$

Thus, for low flow rates the reagent gas molar flow rate is proportional to the carrier gas flow rate. The expression in (EB.9) is in agreement with Holstein (1994) and Love, et al. (1993).

APPENDIX C

SAMPLE CALCULATIONS

SAMPLE CALCULATIONS USED IN CALIBRATING TOLUENE FOR USE IN GAS CHROMATOGRAPHY

Sample calculation of toluene concentration in 160 m*l* serum bottles used in GC gas injection.

Volume of C_7H_8 in liquid syringe = 7 μl

Volume of air in serum bottle = 160 m*l* @ T = 298K and P = 1 atm

Characteristics of toluene (C_7H_8):
Specific Gravity: 0.865 Molecular Weight: 92.13 g/mole

Number moles of C_7H_8:

$(7 \times 10^{-6} l)(0.865)(1000\ kg/m^3)(m^3/1000\ l)(1000\ g/kg) = 6.066 \times 10^{-3}$ g

$(6.066 \times 10^{-3}\ g)(mole/92.13g) = 6.5722 \times 10^{-5}$ moles C_7H_8

Number moles of air in 160 m*l* serum bottle:

$PV = nRT$ or $n = PV/RT$ $R = 8.205 \times 10^{-2}\ m^3\ atm/Kmole\ K$

$$n = \frac{(1\ atm)(0.16\ \ell)\ (m^3 / 1000\ \ell)}{(8.205 \times 10^{-2} m^3 atm / Kmole\ K)(298\ K)(Kmole / 1000\ mole)}$$

$n = 0.006544$ moles air

Total moles = $n_{C7H8} + n_{air} = 6.5722 \times 10^{-5} + 0.006544 = 0.00660954$ moles

Mole fraction of toluene (X) in serum bottle:

$$X_{C7H8} = \frac{\#\ moles\ C_7H_8}{Total\ \#\ moles} = \frac{6.5722 \times 10^{-5}}{0.00660945} = 0.009444$$

The number of moles in the gas syringe is determined as follows:

$$\frac{n_1}{V_1} = \frac{n_2}{V_2} \quad or \quad n_2 = n_1 \frac{V_2}{V_1}$$

The number of moles of toluene injected using a 1 m*l* gas syringe for the 7 μl case is:

$$n_2 = 6.5722 \times 10^{-5}\ moles \times \frac{1\ ml}{160\ ml} = 4.11 \times 10^{-7}\ \text{moles of } C_7H_8 \text{ injected}$$

APPENDIX D

DERIVATION OF GOVERNING EQUATIONS USED IN THE COMPUTER SIMULATION MODELS

D.1 Derivation of the Transport Equation for Particles with Same Radius and Charge

A control volume analysis is used to derive the particle transport equation by examining the fluxes that enter and leave the control volume. The assumptions used in this derivation are as follows:

(a). Particles are of the same size with radius a.

(b). Particles have same charge q.

(c). Electrostatic force e resulting from the particles is considered in the radial direction only.

(d). Particle diffusion is considered in the radial direction only.

(e). Bulk flow gas velocity u is a specific function with only radial dependence.

The equation as presented by Chen (1978) with the above conditions is:

$$u\frac{\partial \rho}{\partial z} = D\frac{1}{r}\frac{\partial}{\partial r}\left(r\frac{\partial \rho}{\partial r}\right) - \frac{1}{r}\left(\frac{q}{6\pi\mu a}\right)\frac{\partial\left(r\rho e_r\right)}{\partial r} \qquad \text{(ED.1)}$$

The transport equation is a flux balance equation consisting of convective, diffusive, and electrostatic flux terms (left to right, respectively). A radial coordinate system with z as the axial distance, and r as the radial distance is used in a cylindrical tube.

ρ = particle density (# particles/volume of gas) = function of r, z

e_r = electric field in the r direction (V/m) where V = N·m/Coulomb

q = charge of particle = # of excess electrons times charge/electron
= (Z_{ch}) (1.602 x 10^{-19} Coulomb/electron)

r = radial distance from tube centerline

a = particle radius

D = particle diffusivity

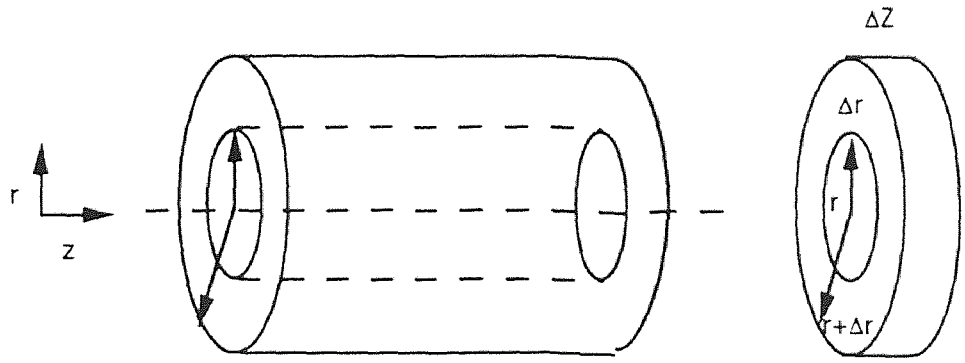

Figure D.1 Control Volume of Δz and Δr

The particle fluxes in and out of the control volume at steady state are described as follows:

$$[\text{ Bulk flow in - Bulk flow out }]_{z\,dir} + [\text{ Diffusion in - Diffusion out}]_{r\,dir} +$$

$$[\text{ Electrostatic in - Electrostatic out}]_{r\,dir} = 0$$

Bulk Flow (convective) term:

Bulk flow = $\rho(r,z)u(r)A_c\Big|_z$ where $u(r)$ = velocity profile

A_c = cross sectional area of control volume shell

$$A_c = \pi(r + \Delta r)^2 - \pi r^2$$
$$= \pi(r^2 + 2r\Delta r + \Delta r^2) - \pi r^2$$
$$= \pi r^2 + 2\pi r\Delta r + \pi\Delta r^2 - \pi r^2$$
$$= 2\pi r\Delta r \quad \text{(first order in } \Delta r)$$

$\therefore$ Bulk flow is:

$$= \rho(r^*,z)u(r^*)2\pi r^*\Delta r\Big|_z - \rho(r^*,z)u(r^*)2\pi r^*\Delta r\Big|_{z+\Delta z}$$

$$= 2\pi r^* \Delta r u(r^*)\left[\rho(r^*,z) - \rho(r^*,z+\Delta z)\right]$$

r^* = mean radius between r and $r + \Delta r$

Diffusion flux term:

[Diffusion in - Diffusion out]$_{r\,dir}$

$$= -D\,2\pi r\Delta z \frac{\partial \rho(r,z^*)}{\partial r}\bigg|_{r} - (-)\,D\,2\pi r\Delta z \frac{\partial \rho(r+\Delta r,z^*)}{\partial r}\bigg|_{r+\Delta r}$$

$$= -D\,2\pi\Delta z\left[r\frac{\partial \rho(r,z^*)}{\partial r} - (r+\Delta r)\frac{\partial \rho(r+\Delta r,z^*)}{\partial r}\right]$$

z^* = mean distance between z and $z + \Delta z$

Electrostatic flux term (due to charged particles):

$$= \rho(r,z^*)U_m(r)2\pi r\Delta z\bigg|_{r} - \rho(r,z^*)U_m(r)2\pi(r)\Delta z\bigg|_{r+\Delta r}$$

where U_m = migration velocity (radial) of particle driven by coulombic attraction to the wall

To obtain U_m we must look at the motion and forces that act on a particle. We start with Newton's Second Law:

$$\boldsymbol{ma} = \Sigma \boldsymbol{F}$$

$$\rho\frac{d\boldsymbol{v}}{dt} = \boldsymbol{F}_{drag} + \boldsymbol{F}_{buoyant} + \boldsymbol{F}_{body} + qE \qquad \text{(vector equation)}$$

For small particles (on the order of 1μm) Stokes' Law can be assumed and is applied to the drag force term.

$$\boldsymbol{F}_{drag} = 3\pi\mu D_p(\boldsymbol{u} - \boldsymbol{v})$$

$\boldsymbol{u}$ = particle velocity $\qquad$ $\boldsymbol{v}$ = radial flow velocity

μ = viscosity of flow gas $\qquad$ D_p = particle diameter

$$\Rightarrow \rho\frac{dv}{dt} = -3\pi\mu D_p(u - v) + \rho_m V - m_p g + qE$$

g = gravitation constant $\qquad$ V = particle volume

E = electrostatic field (vector) $\qquad$ ρ_m = particle mass density

m_p = particle mass

Particle relaxation time to reach terminal velocity is assumed to be very short so that $dv/dt \cong 0$. Also, buoyant and body forces are considered to be << drag forces. Thus, Newton's second law reduces to scalar form. The resulting equation in the radial direction consists of the drag force and electrostatic field component acting in opposite directions:

$$0 = -3\pi\mu D_p u + qe_r \qquad (+ \text{ direction, as } r \to r_o)$$

$$\Rightarrow u = U_m = \frac{q}{3\pi\mu D_p}e_r$$

Substituting this expression into the e field flux term assuming radial direction only:

$$\rho(r,z^*)\frac{q}{3\pi\mu D_p}2\pi r\Delta z e_r\Big|_r - \rho(r,z^*)\frac{q}{3\pi\mu D_p}2\pi r\Delta z e_r\Big|_{r+\Delta r}$$

$$= 2\pi\Delta z\left(\frac{q}{3\pi\mu D_p}\right)\left[r\rho(r,z^*)e_r - (r+\Delta r)\rho(r+\Delta r,z^*)e_r(r+\Delta r)\right]$$

Putting all terms together:

$$2\pi r^*\Delta r u(r^*)\left[\rho(r^*,z) - \rho(r^*,z+\Delta z)\right] - D\,2\pi\Delta z\left[r\frac{\partial\rho(r,z^*)}{\partial r} - (r+\Delta r)\frac{\partial\rho(r+\Delta r,z^*)}{\partial r}\right]$$

$$+ 2\pi\Delta z\left(\frac{q}{3\pi\mu D_p}\right)\left[r\rho(r,z^*)e_r - (r+\Delta r)\rho(r+\Delta r,z^*)e_r(r+\Delta r)\right] = 0$$

Dividing through by the differential volume $2\pi r\Delta r\Delta z$ and noting $2a = D_p$:

$$u(r)\left[\frac{\rho(r^*,z) - \rho(r^*,z+\Delta z)}{\Delta z}\right] - \frac{D}{r}\left[\frac{r\frac{\partial\rho(r,z^*)}{\partial r} - (r+\Delta r)\frac{\partial\rho(r+\Delta r,z^*)}{\partial r}}{\Delta r}\right]$$

$$+\left(\frac{q}{6\pi\mu a}\right)\frac{1}{r}\left[\frac{r\rho(r,z^*)e_r-(r+\Delta r)\rho(r+\Delta r,z^*)e_r(r+\Delta r)}{\Delta r}\right]=0$$

Taking the limit as Δr and $\Delta z \rightarrow 0$ the transport equation becomes:

$$-u(r)\frac{\partial\rho(r,z)}{\partial z}+D\frac{1}{r}\frac{\partial}{\partial r}\left(r\frac{\partial\rho(r,z)}{\partial r}\right)-\frac{1}{r}\left(\frac{q}{6\pi\mu a}\right)\frac{\partial\left(r\rho(r,z)e_r(r)\right)}{\partial r}=0$$

Rearrangement leads to the final result as shown in (ED.1):

$$u(r)\frac{\partial\rho(r,z)}{\partial z}=D\frac{1}{r}\frac{\partial}{\partial r}\left(r\frac{\partial\rho(r,z)}{\partial r}\right)-\frac{1}{r}\left(\frac{q}{6\pi\mu a}\right)\frac{\partial\left(r\rho(r,z)e_r(r)\right)}{\partial r}$$

The resulting equation is valid for charged particles of same radius a and charge q with electrostatic effects from the charged particles themselves in the radial direction only.

The electric field intensity in the radial direction (e_r) is governed by the Poisson equation.

$$\frac{1}{r}\frac{\partial(re_r)}{\partial r}=\frac{\rho q}{\varepsilon_o} \qquad \text{(ED.2)}$$

where ε_o = permittivity of free space = 8.85×10^{-12} $C^2/N\,m^2$

This well know equation is found in many textbooks on electricity and magnetism, so it will only be stated. This equation is coupled to (ED.1) because the electric field generated by charged particles provides the electrostatic flux contribution in (ED.1)

D.1.1 Nondimensionalizing the Governing Equations

The governing equations will now be put in dimensionless form.

Beginning with the transport equation (ED.1) in the form:

$$u\frac{\partial \rho}{\partial z} = D\frac{1}{r}\frac{\partial}{\partial r}\left(r\frac{\partial \rho}{\partial r}\right) - \frac{1}{r}\left(\frac{q}{6\pi\mu a}\right)\frac{\partial(r\rho e_r)}{\partial r}$$

Rewriting (ED.1) in terms of V by using the relation $e = -\partial V/\partial r$, the equation becomes:

$$u\frac{\partial \rho}{\partial z} = D\frac{1}{r}\frac{\partial}{\partial r}\left(r\frac{\partial \rho}{\partial r}\right) + \frac{1}{r}\left(\frac{q}{6\pi\mu a}\right)\frac{\partial}{\partial r}\left(r\rho\frac{\partial V}{\partial r}\right) \qquad \text{(ED.3)}$$

The following dimensionless terms are used:

$$\rho \equiv \frac{\rho}{\rho_o} \Rightarrow \rho \equiv \rho\rho_o \qquad V \equiv \frac{qV}{6\pi\mu aD} \Rightarrow V \equiv V\frac{6\pi\mu aD}{q}$$

$$r \equiv \frac{r}{r_o} \Rightarrow r \equiv rr_o$$

$$z \equiv \frac{zD}{r_o^2 u_o} \Rightarrow z \equiv \frac{zr_o^2 u_o}{D} \quad \text{(as used by Chen)}$$

$$u = \frac{u}{u_o} \Rightarrow u = uu_o$$

where: r_o = inside tube radius $\qquad$ ρ_o = initial particle density

Substituting these dimensionless parameters into the transport equation:

$$uu_o\frac{\partial(\rho\rho_o)}{\partial\left(\frac{zr_o^2u_o}{D}\right)} = D\frac{1}{rr_o}\frac{\partial}{\partial rr_o}\left(rr_o\frac{\partial\rho\rho_o}{\partial rr_o}\right) + \frac{1}{rr_o}\left(\frac{q}{6\pi\mu a}\right)\frac{\partial}{\partial rr_o}\left(rr_o\rho\rho_o\frac{\partial V}{\partial rr_o}\left(\frac{6\pi\mu aD}{q}\right)\right)$$

$$\Rightarrow \qquad \frac{\rho_o D}{r_o^2}u\frac{\partial\rho}{\partial r} = \frac{\rho_o D}{r_o^2}\frac{1}{r}\frac{\partial}{\partial r}\left(r\frac{\partial\rho}{\partial r}\right) + \frac{\rho_o D}{r_o^2}\frac{1}{r}\frac{\partial}{\partial r}\left(r\rho\frac{\partial V}{\partial r}\right) \qquad \text{(ED.4)}$$

Dividing through by $\frac{\rho_o D}{r_o^2}$ the resulting transport equation in dimensionless form is:

$$u\frac{\partial\rho}{\partial z} = \frac{1}{r}\frac{\partial}{\partial r}\left(r\frac{\partial\rho}{\partial r}\right) + \frac{1}{r}\frac{\partial}{\partial r}\left(r\rho\frac{\partial V}{\partial r}\right) \qquad \text{(ED.5)}$$

The Poisson equation is nondimensionalized in a similar manner. Restating the equation in dimensional form:

$$\frac{1}{r}\frac{\partial(re_r)}{\partial r} = \frac{\rho q}{\varepsilon_o} \tag{ED.2}$$

Substituting the relation $e = -\partial V/\partial r$, the Poisson equation becomes:

$$\frac{1}{r}\frac{\partial}{\partial r}\left(r\frac{\partial V}{\partial r}\right) = -\frac{\rho q}{\varepsilon_o} \tag{ED.6}$$

Using the dimensionless variables already defined:

$$\frac{1}{rr_o}\frac{\partial}{\partial r r_o}\left(rr_o\frac{\partial V}{\partial r r_o}\left(\frac{6\pi\mu aD}{q}\right)\right) = -\frac{\rho\rho_o q}{\varepsilon_o}$$

$$\frac{6\pi\mu aD}{qr_o^2}\frac{1}{r}\frac{\partial}{\partial r}\left(r\frac{\partial V}{\partial r}\right) = -\frac{\rho\rho_o q}{\varepsilon_o}$$

Dividing through by $\frac{6\pi\mu aD}{qr_o^2}$ the nondimensionalized form of the Poisson eqn is:

$$\frac{1}{r}\frac{\partial}{\partial r}\left(r\frac{\partial V}{\partial r}\right) = -\frac{\rho_o q^2 r_0^2}{6\pi\mu aD\varepsilon_o}\rho$$

Let $\alpha \equiv \frac{\rho_o q^2 r_0^2}{6\pi\mu aD\varepsilon_o}$

where α is defined as a dimensionless charge parameter. Hence,

$$\frac{1}{r}\frac{\partial}{\partial r}\left(r\frac{\partial V}{\partial r}\right) = -\alpha\rho \tag{ED.7}$$

As a result, two coupled PDEs (ED.5 and ED.7) are solved numerically for particle density ρ as function of radial and axial direction. These two coupled equations are for the case of one size particles with uniform radius, charge, and diffusivity.

The boundary conditions are:

$\left.\frac{\partial V}{\partial r}\right|_{r=0} = 0$ (symmetry at the axis)

$$\left.\frac{\partial \rho}{\partial r}\right|_{r=0} = 0 \quad \text{(for } z > 0\text{, symmetry at the axis)}$$

$$V\Big|_{r=1} = 0 \quad \text{(at the electrically grounded wall)}$$

$$\rho\Big|_{r=1} = 0 \quad \text{(particle density at the wall is zero)}$$

The assumption used in the last boundary condition is that soot particles stick to the wall. A steep radial gradient exits at the wall interface such that the particle density goes to zero

The initial conditions for the governing equations are:

$$\rho\Big|_{z=0} = 1 \quad \text{(at tube inlet, assuming an initial uniform particle density)}$$

$$V = \frac{1}{4}\alpha\left(1 - r^2\right) \quad \text{(derived initial condition for the potential at the tube inlet)}$$

The second initial condition is determined by integrating Poisson's equation assuming an initial uniform density where $\rho = 1$ at $z = 0$:

$$r\frac{\partial}{\partial r}\left(r\frac{\partial V}{\partial r}\right) = -\alpha$$

$$\frac{\partial}{\partial r}\left(r\frac{\partial V}{\partial r}\right) = -\alpha r$$

$$r\frac{\partial V}{\partial r} = -\frac{1}{2}\alpha r^2 + C_1$$

$$\frac{\partial V}{\partial r} = -\frac{1}{2}\alpha r + \frac{C_1}{r}$$

Applying the first boundary condition, C_1 must be zero. Integrating again to obtain V:

$$V = -\frac{1}{4}\alpha r^2 + C_2$$

Applying the second boundary condition and solving for C_2, the initial condition for V is:

$$V = \frac{1}{4}\alpha\left(1 - r^2\right) \qquad \text{(ED.8)}$$

D.2 Derivation of the Governing Equations with Different Size Particles, Charges, and Diffusivities with No External Field Effects

D.2.1 Transport and Poisson's Equations

The modified form of (ED.1) including different particle sizes, charges, and diffusivities for the i^{th} particles is:

$$u\frac{\partial \rho_i}{\partial z} = D_i\frac{1}{r}\frac{\partial}{\partial r}\left(r\frac{\partial \rho_i}{\partial r}\right) - \frac{1}{r}\left(\frac{q_i}{6\pi\mu a_i}\right)\frac{\partial\left(r\rho_i e_r\right)}{\partial r} \qquad \text{(ED.9)}$$

Rewriting (ED.9) in terms of V by using the relation $e = -\partial V/\partial r$, the equation becomes:

$$u\frac{\partial \rho_i}{\partial z} = D_i\frac{1}{r}\frac{\partial}{\partial r}\left(r\frac{\partial \rho_i}{\partial r}\right) + \frac{1}{r}\left(\frac{q_i}{6\pi\mu a_i}\right)\frac{\partial}{\partial r}\left(r\rho_i\frac{\partial V}{\partial r}\right) \qquad \text{(ED.10)}$$

Dividing by $\frac{1}{D_i}$, the transport equation becomes:

$$\frac{1}{D_i}u\frac{\partial \rho_i}{\partial z} = \frac{1}{r}\frac{\partial}{\partial r}\left(r\frac{\partial \rho_i}{\partial r}\right) + \frac{1}{D_i}\frac{1}{r}\left(\frac{q_i}{6\pi\mu a_i}\right)\frac{\partial}{\partial r}\left(r\rho_i\frac{\partial V}{\partial r}\right) \qquad \text{(ED.11)}$$

Nondimensionalizing the parameters similarly as shown in Appendix D.1:

$$\rho_i = \frac{\rho_i}{\rho_{tot}} \Rightarrow \rho_i = \rho_i\rho_{tot} \qquad V = \frac{q_{ref}V}{6\pi\mu a_{ref}D_{ref}} \Rightarrow V = V\frac{6\pi\mu a_{ref}D_{ref}}{q_{ref}}$$

$$r = \frac{r}{r_o} \Rightarrow r = \boldsymbol{r}\, r_o$$

$$z \equiv \frac{zD_{ref}}{r_o^2u_o} \Rightarrow z \equiv \frac{zr_o^2u_o}{D_{ref}}$$

$$u = \frac{u}{u_o} \Rightarrow u = \boldsymbol{u}\, u_o$$

where a_{ref}, q_{ref}, and D_{ref} represent reference values for particle radius, charge, and diffusivity, respectively. The symbol ρ_{tot} represents the total initial particle density (# particles/unit volume).

Plugging in the dimensionless parameters into (ED.11) and canceling out ρ_{tot} / r_o^2 from each term, the equation becomes:

$$\left(\frac{D_{ref}}{D_i}\right)\mu\frac{\partial \rho_i}{\partial z} = \frac{1}{r}\frac{\partial}{\partial r}\left(r\frac{\partial \rho_i}{\partial r}\right) + \left(\frac{D_{ref}}{D_i}\right)\left(\frac{q_i}{q_{ref}}\right)\left(\frac{a_{ref}}{a_i}\right)\frac{1}{r}\frac{\partial}{\partial r}\left(r\rho_i\frac{\partial V}{\partial r}\right) \qquad \text{(ED.12)}$$

Defining:

$$\delta_i = \frac{D_{ref}}{D_i} \qquad \eta_i = \left(\frac{q_i}{q_{ref}}\right)\left(\frac{a_{ref}}{a_i}\right) \qquad \gamma_i = \frac{q_i}{q_{ref}}$$

(ED.12) becomes the dimensionless transport equation for particle i. Thus:

$$(\delta_i)\mu\frac{\partial \rho_i}{\partial z} = \frac{1}{r}\frac{\partial}{\partial r}\left(r\frac{\partial \rho_i}{\partial r}\right) + (\delta_i)(\eta_i)\frac{1}{r}\frac{\partial}{\partial r}\left(r\rho_i\frac{\partial V}{\partial r}\right) \qquad \text{(ED.13)}$$

For a particle distribution of i = 1,2,····,n fractions, there are i = 1,2,····,n dimensionless transport equations (ED.13) that are needed.

The Poisson equation for particle i is:

$$\frac{1}{r}\frac{\partial}{\partial r}\left(r\frac{\partial V}{\partial r}\right) = -\sum_{i=1}^{n}\frac{\rho_i q_i}{\varepsilon_o} \qquad \text{(ED.14)}$$

Plugging in the nondimensional parameters defined above and rearranging the terms, the Poisson's equation becomes:

$$\frac{1}{r}\frac{\partial}{\partial r}\left(r\frac{\partial V}{\partial r}\right) = -\alpha_o\sum_{i=1}^{n}\gamma_i\rho_i \qquad \text{(ED.15)}$$

where the modified dimensionless charge parameter alpha (α_o) is a constant:

$$\alpha_o = \left(\frac{r_o^2 q_{ref}^2 \rho_{tot}}{6\pi\mu a_{ref} D_{ref}\varepsilon_o}\right)$$

Equation (ED.15) is a single equation with the fractions summed on the right hand side of the expression. Note that the electrostatic field contribution of all particles i have been combined for a total field.

D.2.2 Derivation of Penetration of a Given Particle Fraction and Total Penetration

Penetration, $P(z)$, is a ratio of the (radial) mean particle density at axial position z over the mean initial density at $z = 0$.

If $\rho(r,0) = \rho_o$ then:

$$P(z) = \frac{\int_0^R 2\pi\rho(r,z)rdr}{\int_0^R 2\pi\rho(r,0)rdr} = \frac{\int_0^R 2\pi\rho(r,z)rdr}{2\pi\rho_o\left(\frac{1}{2}R^2\right)} \qquad \text{(ED.16)}$$

Where R refers to r_o (tube radius). Note the lower limit of integration is zero. If a central wire of radius r_i is present, then lower limit would be r_i.

Using the dimensionless variables, $r = r/R$, and $\rho = \rho/\rho_o$, and substituting them into (ED.16), the penetration reduces to:

$$P(z) = 2\int_0^1 \rho r dr \qquad \text{(ED.17)}$$

For particles of different sizes with the i^{th} fraction having representative radius, a_i, the penetration of fraction i is:

$$P_i(z) = 2\int_0^1 \hat{\rho}_i r dr \quad \text{where } \hat{\rho}_i = \frac{\rho_i}{\rho_{i,o}} \quad \text{and} \qquad \text{(ED.18)}$$

$\rho_{i,o}$ = initial particle density of particle i. Previously, we defined ρ_i as:

$$\rho_i = \frac{\rho_i}{\rho_{tot}}$$

with $\hat{\rho}_i = \frac{\rho_i}{\rho_{i,o}}$

Substituting $\rho_i = \rho_i\rho_{tot}$ into $\hat{\rho}_i$, the expression for $\hat{\rho}_i$ becomes:

$$\hat{\rho}_i = \frac{\rho_{tot}}{\rho_{i,o}}\rho_i \quad \text{with } f_i \text{ defined as } f_i = \frac{\rho_{i,o}}{\rho_{tot}} \text{ (initial fraction of particle } i\text{).}$$

Thus $\hat{\rho}_i$ becomes $\hat{\rho}_i = \frac{1}{f_i}\rho_i$

Now, using equation (ED.18), the penetration of fraction i at z is:

$$P_i(z) = \frac{2}{f_i}\int_0^1 \rho_i(r,z) r dr \qquad \text{(ED.19)}$$

Deposition for particle i is easily calculated as $D_i(z) = 1 - P_i(z)$.

A volume weighted average is used to obtain an overall expression for total penetration. This approach, as opposed to a mass weighted average of fraction i, is taken because little information on mass density of the various size particles (submicron and larger) is known. Therefore, an overall efficiency based on volume for the particle density at any axial position z is used in calculating penetration or deposition. A common practice in volume calculation is assuming spherical particles. The volume of particles per axial length in fraction i at any position z is:

$$V_i(z) = \left[2\pi\int_0^R \rho_i(r,z) r dr\right]\left(\frac{4}{3}\pi a_i^3\right) \qquad \text{(ED.20)}$$

where a_i = average particle radius for particle fraction i

The fraction may not consist of discrete particle diameters, but may include a small range of particle sizes over a continum constituting a narrow particle size distribution. Therefore, an average particle radius a_i for a fractional cut is used.

Dimensionless variables in the form of $\boldsymbol{r} = r/R$, $f_i = \rho_{i,o} / \rho_{tot}$, and $\rho_i = \frac{\rho_i}{\rho_{tot}}$ are used.

Equation (ED.20) becomes:

$$V_i(z) = 2\pi\int_0^1 \rho_{tot}\rho_i(\boldsymbol{r}R)d(\boldsymbol{r}R)\left(\frac{4}{3}\pi a_i^3\right)$$

Rearranging and simplifying results in:

$$V_i(z) = \left[2\pi R^2\rho_{tot}\int_0^1 \rho_i(r,z) r dr\right]\left(\frac{4}{3}\pi a_i^3\right) \qquad \text{(ED.21)}$$

The total volume of particles is the sum of all $V_i(z)$ or $V(z) = \sum_{i=1}^{n} V_i(z)$

$$V(z) = \sum_{i=1}^{n}\left\{\left(2\pi R^2 \rho_{tot}\int_0^1 \rho_i r dr\right)\frac{4}{3}\pi a_i^3\right\} = 2\left(\frac{4}{3}\pi^2 R^2\right)\rho_{tot}\sum_{i=1}^{n} a_i^3\int_0^1 \rho_i r dr \qquad \text{(ED.22)}$$

At $z = 0$, the particle volume for particle i is:

$$V_i(0) = \left[2\pi\int_0^R \rho_i(r,0) r dr\right]\left(\frac{4}{3}\pi a_i^3\right) \qquad \text{where } \rho_i(r,o) = \rho_{i,o} \qquad \text{(ED.23)}$$

Multiplying the integral by $\frac{\rho_{tot}}{\rho_{tot}}$:

$$V_i(0) = \left[2\pi R^2\int_0^1 \frac{\rho_{i,o}}{\rho_{tot}}\rho_{tot} r dr\right]\left(\frac{4}{3}\pi a_i^3\right)$$

Noting that $f_i = \frac{\rho_{i,o}}{\rho_{tot}}$

$$V_i(0) = \left[2\pi R^2 \rho_{tot}\int_0^1 f_i r dr\right]\left(\frac{4}{3}\pi a_i^3\right) \qquad \text{(ED.24)}$$

The total particle volume at $z = 0$ is:

$$V(0) = \sum_{i=1}^{n}\left\{\left(2\pi R^2 \rho_{tot} f_i\int_0^1 r dr\right)\frac{4}{3}\pi a_i^3\right\} = \left(\frac{4}{3}\pi^2 R^2\right)\rho_{tot}\sum_{i=1}^{n} f_i a_i^3 \qquad \text{(ED.25)}$$

By taking the ratio of the total particle volume at any point z over the total particle volume at $z = 0$ (i.e. ratio of Eqns. (ED.22) and (ED.25)), the fraction is essentially a "volume penetration". The expression for total penetration after cancelling like terms becomes:

$$P_{tot} = \frac{2\sum_{i=1}^{n}\left\{a_i^3\int_0^1 \rho_i r dr\right\}}{\sum_{i=1}^{n} f_i a_i^3} = \frac{\sum_{i=1}^{n}\left\{2a_i^3\int_0^1 \rho_i r dr\right\}}{\sum_{i=1}^{n} f_i a_i^3} \qquad \text{(ED.26)}$$

Notice that if f_i / f_i is multiplied in (ED.26) we have $\frac{2}{f_i}\int_0^1 \rho_i r dr$, which is penetration for particle i, $P_i(z)$ defined in (ED.19). Therefore, P_{tot} becomes:

$$P_{tot} = \frac{\sum_{i=1}^{n}\left\{f_i \frac{2}{f_i} a_i^3 \int_0^1 \rho_i r dr\right\}}{\sum_{i=1}^{n} f_i a_i^3} = \frac{\sum_{i=1}^{n}\left\{f_i a_i^3 P_i(z)\right\}}{\sum_{i=1}^{n} f_i a_i^3} \qquad \text{(ED.27)}$$

Total deposition (D_{tot}) is just 1 - P_{tot}. If the density is the same for all particles then (ED.27) becomes an overall mass penetration by multiplying by the average density.

D.3 Applied External Electric Field in the Presence of Charged Particles

When an external electric field e is applied by use of a central wire in a cylindrical tube the form of e_r is (Bohm, 1982):

$$e_r = \frac{V_o}{\ln \frac{r_o}{r_i}} \frac{1}{r} \qquad \text{where } r_o = \text{inside tube radius, } r_i = \text{wire radius} \qquad \text{(ED.28)}$$

V_o = applied DC potential (volts)

As noted in Chapter 4 (Section 4.2.3), the space charge contribution of the particles is omitted. Therefore, substituting e_r (ED.28) into the transport equation (ED.1):

$$u\frac{\partial \rho}{\partial z} = D\frac{1}{r}\frac{\partial}{\partial r}\left(r\frac{\partial \rho}{\partial r}\right) - \frac{qV_o}{6\pi\mu a \ln \frac{r_o}{r_i}} \frac{1}{r}\frac{\partial \rho}{\partial r}$$

Inserting the dimensionless parameters with $z = z/L$ for a finite length tube, the equation becomes:

$$u\frac{\partial \rho}{\partial z} = \frac{DL}{u_o r_o^2}\frac{1}{r}\frac{\partial}{\partial r}\left(r\frac{\partial \rho}{\partial r}\right) - \frac{qV_oL}{6\pi\mu a \ln \frac{r_o}{r_i} u_o r_o^2} \frac{1}{r}\frac{\partial \rho}{\partial r}$$

Recognizing the dimensionless parameter, Peclet number = $u_o r_o/D$ and rewriting as:

$$u\frac{\partial \rho}{\partial z} = \frac{1}{Pe}\frac{L}{r_o}\frac{1}{r}\frac{\partial}{\partial r}\left(r\frac{\partial \rho}{\partial r}\right) - \frac{qV_oL}{6\pi\mu a \ln \frac{r_o}{r_i} u_o r_o^2} \frac{1}{r}\frac{\partial \rho}{\partial r} \qquad \text{(ED.29)}$$

Using physical values in the reactor tube and reasonable values for a 1 μm particle assuming 50 charges:

$r_o = 9.525 \times 10^{-3}$ m $q = 8.0 \times 10^{-18}$ C

$u_o = 3.6$ m/s $D = 3.0 \times 10^{-11}$ m^2/s

$a = 0.5 \times 10^{-6}$ m $\mu = 330.0 \times 10^{-7}$ Ns/m^2 (air at 400°C)

$r_i = 7.62 \times 10^{-4}$ m $\qquad V_o = 3000$ Volts

$L = 0.4064$ m $\qquad \nu = 6.384 \times 10^{-5}$ m^2/s (air at 400 °C)

$$\mathrm{Re} = \frac{2u_o r_o}{\nu} = \frac{2(3.6\ m/s)(0.009525\ m)}{6.384 \times 10^{-5}\ m^2/s} = 1074 \text{ (Laminar Flow)}$$

The first term on the right hand side of the dimensionless transport equation is:

$$\frac{1}{Pe} = 8.75 \times 10^{-10} \qquad \text{or} \qquad \frac{1}{Pe}\frac{L}{r_o} = 3.73 \times 10^{-8}$$

The second term on the right hand side is:

$$\frac{qV_o L}{6\pi\mu a \ln \frac{r_o}{r_i} u_o r_o^2} = 0.038$$

Clearly, the first term on the right hand side is very small compared to the second term when an applied electric field is present in a finite length tube.

$$\frac{1}{\mathrm{Pe}}\frac{\mathrm{L}}{\mathrm{r_o}} << \frac{qV_o L}{6\pi\mu a \ln \frac{r_o}{r_i} u_o r_o^2}$$

By dropping the first term on the right hand side of (ED.29) as a result of high V_o, solutions develop in which a steep radial gradient moves from r_i to r_o as z increases. However, this gradient is very localized and over most of the radial distance such that $\partial\rho/\partial r \cong 0$. Therefore, on an integrated basis, eliminating the first term on the right hand side at high applied field should have little effect.

The transport equation now reduces to:

$$u\frac{\partial \rho}{\partial z} = -\frac{qV_o L}{6\pi\mu a \ln \frac{r_o}{r_i} u_o r_o^2}\frac{1}{r}\frac{\partial \rho}{\partial r} \qquad \text{(ED.30)}$$

When the partial differential equation is rearranged and both terms are on the left hand side, the following first order PDE is obtained:

$$u\frac{\partial \rho}{\partial z} + \frac{qV_o L}{6\pi\mu a \ln \frac{r_o}{r_i} u_o r_o^2} \frac{1}{r}\frac{\partial \rho}{\partial r} = 0 \qquad \text{(ED.31)}$$

Let: $\beta = \dfrac{qV_o L}{6\pi\mu a \ln \frac{r_o}{r_i} u_o r_o^2}$

The equation is reduced to a readily solvable PDE:

$$u\frac{\partial \rho}{\partial z} + \beta \frac{1}{r}\frac{\partial \rho}{\partial r} = 0 \qquad \text{(ED.32)}$$

The dimensionless velocity u is a function of r. If we use a dimensionless parabolic expression $(1 - r^2)$ for laminar flow and rearrange the PDE, we obtain:

$$\frac{\partial \rho}{\partial z} + \beta \frac{1}{r(1-r^2)}\frac{\partial \rho}{\partial r} = 0 \qquad \text{(ED.33)}$$

This equation is solved analytically through an appropriate substitution:

$$R = \int r(1-r^2)dr = \frac{r^2}{2} - \frac{r^4}{4} + C_1 \qquad \text{(ED.34)}$$

Applying the chain rule to $\dfrac{\partial}{\partial r}$ to obtain an expression in terms of $\dfrac{\partial}{\partial R}$

$$\frac{\partial}{\partial r} = \frac{\partial R}{\partial r}\frac{\partial}{\partial R} = r(1-r^2)\frac{\partial}{\partial R}$$

Substituting back into the PDE the equation simplifies to:

$$\frac{\partial \rho}{\partial z} + \beta \frac{\partial \rho}{\partial R} = 0 \qquad \text{(ED.35)}$$

The solution to this PDE is in the form of :

$$\rho(r,z) = g(R - \beta z) = g\left(\frac{r^2}{2} - \frac{r^4}{4} - \beta z\right) \qquad \text{(ED.36)}$$

where $g(\cdot)$ is an arbitrary function. Thus, $\dfrac{r^2}{2} - \dfrac{r^4}{4} - \beta z = constant$ gives us the family of characteristic curves, such that as shown in Figure D3.1. Alternately, multiplying the equation through by 4 gives $2r^2 - r^4 - 4\beta z = const.$ Equation (ED.36) is now rewritten as:

$$\rho(r,z) = f\left(2r^2 - r^4 - 4\beta z\right) \qquad \text{(ED.37)}$$

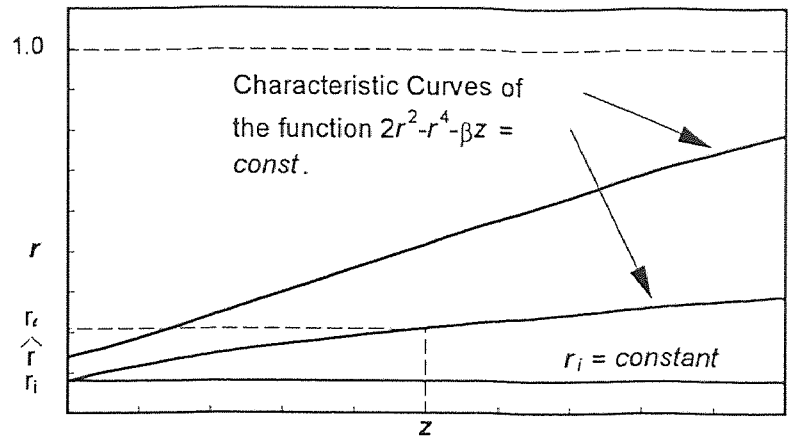

Figure D3.1 Plot of Characteristic Curves for r and z

Figure D3.1 is a plot of two characteristic curves based on the function (ED.37) using dimensionless r and z. This density function $\rho(r,z)$ is constant along the characteristic curve. The curves start at $z = 0$, but the starting point on r is different for each curve. Therefore, a family of characteristic curves is plotted. Variation of β (i.e. increased applied field or particle charge) allows faster convergence to r_o along a characteristic curve.

The dimensionless term r_ℓ refers to the lower limit point on the curve for a given r and z. The other dimensionless term r_i is equal to r_i/r_o . The radius of the central wire is defined as r_i, and the radius of the tube wall is r_o.

An arbitrary point, (r,z), lies on the characteristic curve intersecting z = 0 (tube entrance) at $(\hat{r},0)$ where:

$$2r^2 - r^4 - 4\beta z = 2\hat{r}^2 - \hat{r}^4$$

multiplying the equation through by - 1:

$$\hat{r}^4 - 2\hat{r}^2 = r^4 - 2r^2 + 4\beta z$$

completing the square of the 4th order polynomial:

$$\hat{r}^4 - 2\hat{r}^2 + 1 = r^4 - 2r^2 + 4\beta z$$

simplifying the equation:

$$\left(1 - \hat{r}^2\right)^2 = \left(1 - r^2\right)^2 + 4\beta z$$

solving for $\hat{r}$ the expression becomes:

$$\hat{r} = \left(1 - \sqrt{\left(1 - r^2\right)^2 + 4\beta z}\right)^{\frac{1}{2}} \qquad \text{(ED.38)}$$

The negative root of the equation yields a realistic solution. If $\rho_{init}(\cdot) = \rho(\cdot\ , 0)$ then

$$\rho(r,z) = \rho_{init}\left(\left[1 - \sqrt{\left(1 - r^2\right)^2 + 4\beta z}\right]^{\frac{1}{2}}\right) \qquad \text{(ED.39)}$$

if $\left(1 - r^2\right)^2 + 4\beta z \leq r_i^2$, otherwise $\rho(r,z) = 0$. Thus, for a given z, $\rho(r,z) = 0$ for $r < r_\ell$. In other words, the region below the characteristic curve beginning at $(r_i,0)$ represents a depleted inner core in which the dimensionless particle density ρ is equal to zero. Thus, the characteristic curve separates a depleted region from a particle laden outer flow existing above the curve (See Figure D3.2). The radial gradient discussed earlier occurs at the boundary interface of the characteristic curve at any given position along the axial direction $(r_\ell\ , z)$.

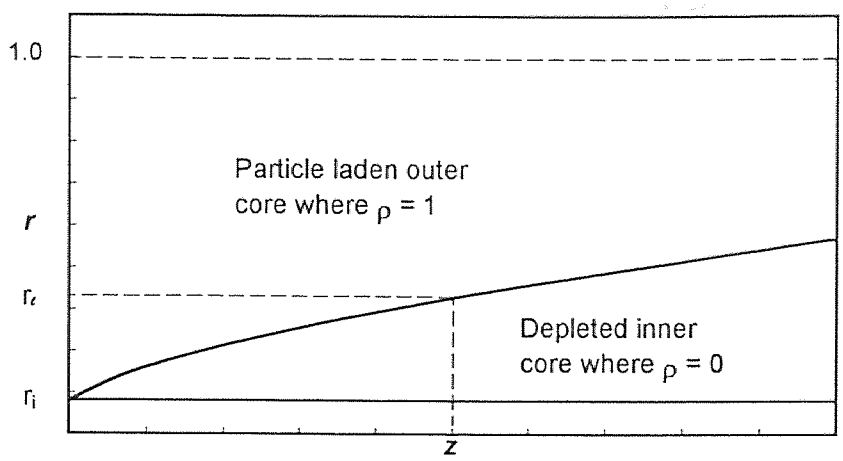

Figure D3.2 Particle Density ρ in the Regions Between the Characteristic Curve with Initial Particle Density $\rho(r,0) = 1$

This lower limit r_ℓ is obtained by using the same method as the expression of $\hat{r}$.

$$r_\ell^4 - 2r_\ell^2 + 4\beta z = r_i^4 - 2r_i^2 + 4\beta z_i$$

at $z_i = 0$ and solving for r_ℓ the expression becomes:

$$r_\ell = \left(1 - \sqrt{\left(1 - r_i^2\right)^2 - 4\beta z}\right)^{\frac{1}{2}} \tag{ED.40}$$

Consequently, penetration (P) is calculated by integrating the region between r_ℓ and r_o. Penetration is expressed as:

$$P(z) = \frac{\int_{r_\ell}^{1} 2\pi\rho(r,z)rdr}{\int_{r_i}^{1} 2\pi\rho(r,0)rdr} \tag{ED.41}$$

Substituting (ED.39) for $\rho(r,z)$, a general expression for $P(z)$ becomes:

$$P(z) = \frac{\int_{r_\ell}^{1} 2\pi\rho_{init}\left(\left[1 - \sqrt{(1 - r^2) + 4\beta z}\right]\right)rdr}{\int_{r_i}^{1} 2\pi\rho_{init}(r)rdr} \tag{ED.42}$$

If $\rho_{init} = 1$ for $r_i \le r \le 1$ in the case of a radially uniform inlet density, the expression for penetration reduces to:

$$P(z) = \frac{\sqrt{\left(1 - r_i^2\right)^2 - 4\beta z}}{1 - r_i^2} \qquad \text{(ED.43)}$$

The concept of penetration can be visualized using Figure D3.2. The integral in the denominator of (ED.41) is integrated from r_i to 1, assuming $\rho(r,0) = 1$. The numerator of (ED.41) is integrated from the point r_ℓ for a given z on the characteristic curve to $r = 1$. The ratio of the two integrals provides the amount of particle penetration at any given z in the reactor tube.

Since the center wire radius is assumed to be very small ($r_i << 1$), (ED.43) is approximated by:

$$P(z) = \sqrt{1 - 4\beta z} \qquad for\ z \le \frac{1}{4\beta} \qquad \text{(ED.44)}$$

and $P(z) = 0$ for $z > \frac{1}{4\beta}$ with deposition = 1 - $P(z)$.

Equation (ED.44) is an expression for penetration for a single particle size. The characteristic curve intersecting at $r = r_i$ at $z = 0$ was used because we were interested in the density function $\rho(r,z)$, starting at central wire radius and integrating $\rho(r,z)$ radially outward to r_o (see Figure D3.2).

(ED.44) is modified by subscripting $P(z)$ and β to include multiple particle size fractions. Penetration of the i^{th} particle is expressed as:

$$P_i(z) = f_i\sqrt{1 - 4\beta_i z} \qquad for\ z \le \frac{1}{4\beta_i} \qquad \text{(ED.45)}$$

and $P(z) = 0$ for $z > \frac{1}{4\beta_i}$.

Equation (ED.45) is the i^{th} particle penetration based on particle number density. The total number particle penetration P_{tot} is the summation of all $P_i(z)$:

$$P_{tot} = \sum_{i=1}^{n} P_i(z) = \sum_{i=1}^{n} f_i\sqrt{1-4\beta_i z} \qquad \text{(ED.46)}$$

An expression for volume penetration in a similar manner described in Section D.2.2 is as follows:

$$P_{tot} = \frac{\sum_{i=1}^{n} f_i a_i^3\sqrt{1-4\beta_i z}}{\sum^{n} f_i a_i^3} \qquad \text{(ED.47)}$$

APPENDIX E

INPUT FILES FOR SIMULATION COMPUTER CODES

INPUT FILE FOR THE MATHEMATICAL MODEL USING A MULTIPLE PARTICLE SIZE FRACTION WITH NO APPLIED FIELD

0.009525	<= ROD (radius of tube (m))
2	<= NFRACC (number of fractions)
0.7d-6 20d0 0.90	<= radius of particle i, charge(i), frac(i)
1.5d-6 80d0 0.10	
1	<= iref
2.2D+6	<= ptot (# particles/m^3)
330.0D-7	<= mu (viscosity of air @ 400 C N s/m^2)
3.6	<= velocity (m/s)
673	<= Temp (K)
1	<= rleng
10	<= nintv

The file **test1.dat** is the input file for source code program: **nfracmx.for**
The source code nfracmx.for solves the PDEs for the condition of a multiple particle size distribution with no applied voltage.

INPUT FILE FOR THE MATHEMATICAL MODEL USING A MULTIPLE PARTICLE SIZE FRATION WITH AN APPLIED FIELD

0.000762 0.009525	<= RID,ROD (radius of wire and tube (m))
2	<= number of fractions
3.0d-6 0.10	<= particle diameter, fraction
1.4d-6 0.90	
0.35	<= cfrac (percent of saturation)
330.0D-7	<= mu (viscosity of air @ 400 C N s/m^2)
3.6	<= gas velocity m/s
3000d0	<= Applied Voltage (volts)
0.4064d0	<= effective tube length (m)

The file **test3.dat** is the input file for source code program: **tstdat2.for**
The source code tstdat2.for solves the equation for penetration of the i^{th} particle as well as total penetration. Both number and volume penetration are calculated with an applied voltage.

APPENDIX F

SIMULATION COMPUTER CODE FOR NO APPLIED VOLTAGE AND APPLIED VOLTAGE MODELS

```
C     Multi-Fraction Model including Diffusion and No Applied Field
C
C     C0 COLLOCATION PARAMETERS
      implicit double precision (a-h,o-z)
      PARAMETER ( IBK   =  30, NEL  = IBK-1,NFRCMX =  10,
     A          NPDEMX = 1+NFRCMX, NV = 0,
     1          NPOLY = 2,  NPTS = NEL*NPOLY+1,  NXI = 0,
     2          NEQMX   = NPTS * NPDEMX + NV,
     3          NWKRES= (NPOLY+1) * (5*NXI + 3*NPOLY+NEL+5+7*NPDEMX) +
     4          NPDEMX * 8 + 3 + NV + NXI,
C     DDASSL TIME INTEGRATION PARAMETERS
     5          MAXORD = 5, LRW = 40 + (MAXORD+4) * NEQMX + NEQMX**2,
     6          LIW = 20 + NEQMX )
C
      INTEGER IWORK(LIW), INFO(15), IBAND, M, ITIME, I, IDID, IRESWK,
     1        IDEV, ITRACE, NP
      DOUBLE PRECISION XBK(IBK), X(NPTS), Y(NEQMX), YDOT(NEQMX),
     1    WKRES(NWKRES), RWORK(LRW), XI(1),T,TOUT,RTOL, ATOL,
     2    ENORM, GERR, VERROR, CTIME, TOL, xout(101),U(NPDEMX,NPTS),
     3    uout(2,21,2),PI,rod,charge(nfrcmx),po,Vo,e0,dist,vel,
     4    diff(nfrcmx),mu,a(nfrcmx),Temp,e,alpha,ccrule(50),
     5    DEL(NFRCMX), GAM(NFRCMX), ETA(NFRCMX), FRAC(NFRCMX),
     6    q(nfrcmx), qc(nfrcmx), qref
      parameter (e0 = 8.85d-12, akb = 1.380d-23, e =  1.60d-19)
      CHARACTER*12 FILEN
      EXTERNAL PDECHB, DGEJAC
      COMMON /SDEV2/ ITRACE, IDEV
      COMMON /DVAR/  ALPHA0
      COMMON /DVAR2/ ALPHA,DEL,ETA,GAM,FRAC,NFRACC
      common /schsz6/ ccrule
      save
      M    = 1
      T    = 0d0
      IDEV = 4
      PI = 4d0*ATAN(1d0)
*       print*,'Enter filename to be read enclosed in tick marks'
*       read*, FILEN
      open (5, file='test1.dat', status='unknown')
      open (idev, file= 'output.dat',status='unknown')
      write(idev,1)NPOLY, NEL
 1    FORMAT(' MULTI-FRAC MODEL'/' **********'/' POLY OF DEGREE =',I4,
     1        ' NO OF ELEMENTS = ',I4)
      write (idev,*)
      read (5,*) rod
      READ (5,*) nfracc
      DO 10, I = 1, nfracc
 10      READ (5,*) a(i),charge(i),frac(i)
      READ (5,*) iref
      read (5,*) po
      read (5,*) xmu
      read (5,*) vel
      read (5,*) Temp
      read (5,*) rleng
```

```
      read (5,*) nintv
C*********************************************************************C
C     Converting physical input into dimensionless parameters:  alpha0
C     Note: Fstar has units of kg/s
C*********************************************************************C
      do 8, i = 1, nfracc
      q(i) = charge(i)*e
      diff(i) = akb*Temp/(6d0*PI*xmu*a(i))
 8    continue
C*********************************************************************C
      qref = q(iref)
      difref = diff(iref)
      do 9, i = 1, nfracc
      qc(i) = q(i)/qref
 9    continue
      Fstar = 6d0*PI*xmu*a(iref)
      alpha = po*qref**2*rod**2/(4d0*e0*DIFREF*Fstar)
      sumgf = 0d0
      do 16, i = 1, nfracc
        del(i)  = difref/diff(i)
        gam(i)  = qc(i)/qc(iref)
        eta(i)  = del(i)*gam(i)*a(iref)/a(i)
        sumgf = sumgf + frac(i)*gam(i)
 16   continue
      alpha0 = alpha*sumgf
      write (idev,FMT=2) alpha
 2    format(2x,'alpha = ',D11.4)
      write (idev,*)
      ITRACE = 0
      tfin = DIFREF*rleng/(rod**2*vel)
      tinc = tfin/nintv
      h = 0.97d0/(ibk-6)
      do 1111, i = 1, (ibk-5)
1111      xbk(i) = (i-1)*h
      xbk(ibk-6) = 0.980d0
      xbk(ibk-5) = 0.985d0
      xbk(ibk-4) = 0.990d0
      xbk(ibk-3) = 0.994d0
      xbk(ibk-2) = 0.996d0
      xbk(ibk-1) = 0.999d0
      xbk(ibk)  = 1d0
C*********************************************************************C
C         INITIALISE THE P.D.E. WORKSPACE
C*********************************************************************C
      ITIME  = 1
      NPDE = 1 + NFRACC
      NEQ = NPDE*NPTS+NV
      CALL INICHB(NEQN,NPDE, NPTS, X, Y, WKRES, NWKRES, M, T, IBAND,
     1            ITIME, XBK, IBK, NEL, NPOLY, NV, NXI, XI, IDEV)
      IF(ITIME .EQ. -1)THEN
        WRITE(IDEV, 15)
 15     FORMAT(' INITCC ROUTINE RETURNED ITIME = -1 - RUN HALTED ')
        GOTO 100
      END IF
```

```
C       SETUP DASSL PARAMETERS
      RTOL = 1d-4
      ATOL = 1d-4
      DO 20 I = 1,11
 20     INFO(I) = 0
C
C       BANDED MATRIX OPTION WHEN INFO(6) = 1
      IF(INFO(6) .EQ. 1)THEN
        IWORK(1) = IBAND
        IWORK(2) = IBAND
      END IF
      tout = 0d0
 30   tout = tout + tinc
      if (tout .gt. tfin) go to 100
 35   continue
      CALL DDASSL( PDECHB, NEQ, T, Y, YDOT, TOUT, INFO, RTOL, ATOL,
     1           IDID, RWORK, LRW, IWORK, LIW, WKRES,
     2           NWKRES, DGEJAC)
      IF( IDID .LT. 0 )THEN
C       DASSL FAILED TO FINISH INTEGRATION.
        GOTO 100
      ELSE
C*********************************************************************C
C     SEND OUTPUT X,V,E,R,dR/dr TO OUTPUT.DAT FILE
C*********************************************************************C
      DO 88 I=1,NPDE
        DO 88 J=1,NPTS
 88       U(I,J) = Y((J-1)*NPDE+I)
        WRITE(IDEV,40)T,IDID
 40     FORMAT(' AT X = ',D11.3,' DASSL RETURNED IDID =',I3)
      write (idev,*)
      dist = (tout*rod**2*vel/DIFREF)*1d2
      write(idev,42) dist
 42   format(' At X Distance = ',D11.4,' cm')
      write(idev,*)
*     itype=2
*     CALL INTERC(xout,uout,np,21,y,neq,npde,
*    1           iflag,itype,wkres,nwkres)
      write (idev,FMT=81)
 81   format(7x,'r  ',10x,' V ',10x,' rho1', 10x,'rho2')
      write (idev,90) (x(i),u(1,I),u(2,I),u(3,i),i=1,npts)
 90   format(2x,D11.3,4x,D11.3,4x,d11.3,4x,D11.3)
      write(idev,*)
C*********************************************************************C
C     Calculation of particle penetration and deposition
C*********************************************************************C
      vint = 0d0
      do 91, i = 1, nel
       jst = (i-1)*npoly
       vintj = 0d0
       do 92, j = 1, npoly+1
 92       vintj = vintj + ccrule(j)*u(2,jst+j)*x(jst+j)
 91       vint = vint + vintj*(x(jst+npoly+1) - x(jst+1))
* 2 * integral = 2 * 0.5 * vint = vint
```

```
      write (idev,*) 'penetration ',vint,'   deposition',1d0-vint
      write (idev,*)
C
      go to 30
      END IF
100   CONTINUE
C***********************************************************************C
C     OUTPUT THE NUMBER OF STEPS
C***********************************************************************C
      WRITE(IDEV,110)IWORK(11),IWORK(12),IWORK(13)
110   FORMAT(' NSTEPS =',I5,' NRESID =',I5,' JAC = ',I4)
      STOP
      END
C***********************************************************************C
C     DUMMY SUBROUTINE EXACT
C***********************************************************************C
      SUBROUTINE EXACT
      RETURN
      END
C***********************************************************************C
C     INITIAL VALUES FOR THE PARTIAL DIFFERENTIAL EQUATION ARE
C     IN THE SUBROUTINE UVINIT
C***********************************************************************C
      SUBROUTINE UVINIT( NPDE, NPTS, X, U, NV, V)
      IMPLICIT DOUBLE PRECISION (A-H,O-Z)
C     ROUTINE FOR O.D.E. AND P.D.E. INITIAL VALUES.
      PARAMETER (NFRAC=10)
      DOUBLE PRECISION ALPHA, DEL(NFRAC), ETA(NFRAC), GAM(NFRAC)
      DOUBLE PRECISION FRAC(NFRAC)
      INTEGER NPDE, NPTS, NV
      COMMON /DVAR/ ALPHA0
      COMMON /DVAR2/ ALPHA,DEL,ETA,GAM,FRAC,NFRACC
      DOUBLE PRECISION X(NPTS), U(NPDE,NPTS), TIME, TOL
      do 10 i = 1,npts
        u(1,i) = alpha0*(1d0 - x(i)**2)
        DO 10, K = 1, NFRACC
 10     u(1+K,i) = FRAC(K)
      RETURN
      END
C
      SUBROUTINE SPDEFN(T, X, NPTL, NPDE, U, DUDX, UDOT, UTDX, Q, R,
     1                  NV, V, VDOT, IRES)
C     PROBLEM INTERFACE  FOR THE MOVING BOUNDARY PROBLEM.
      IMPLICIT DOUBLE PRECISION (A-H,O-Z)
      INTEGER NPTL, NPDE, NV, I, IRES
      PARAMETER (NFRAC=10)
      DOUBLE PRECISION DEL(NFRAC),ETA(NFRAC),GAM(NFRAC),FRAC(NFRAC)
      COMMON /DVAR/ ALPHA0
      COMMON /DVAR2/ ALPHA,DEL,ETA,GAM,FRAC,NFRACC
      DOUBLE PRECISION X(NPTL), U(NPDE,NPTL), DUDX(NPDE,NPTL), T,
     1     V(1), VDOT(1), Q(NPDE,NPTL) ,R(NPDE,NPTL),
     2     UDOT(NPDE,NPTL), UTDX(NPDE,NPTL), vi, alpha, ri
C***********************************************************************C
C     Use of Laminar velocity profile
```

```
C*********************************************************************C
      DO 10 I = 1,NPTL
        r(1,i) = dudx(1,i)
        SUM = 0D0
        DO 20, K = 1, NFRACC
          r(1+K,i) = dudx(1+K,i) + ETA(K)*u(1+K,i)*dudx(1,i)
          q(1+K,i) = DEL(K)*(1d0-x(i)**2)*udot(1+K,i)
C         q(1+k,i) = DEL(K)*udot(1+k,i)
 20       SUM = SUM + GAM(K)*U(1+K,I)
        Q(1,I) = -4d0*ALPHA*SUM
 10   CONTINUE
      RETURN
      END
      SUBROUTINE SBNDR( T, BETA, GAMMA, U, UX, UDOT, UTDX, NPDE,
     1                  LEFT, NV, V, VDOT, IRES)
C  THIS SUBROUTINE PROVIDES THE LEFT AND RIGHT BOUNDARY VALUES
C  here in the form
C         BETA(I) * "RI" (as used above) = GAMMA(I)
C  WHERE I = 1,NPDE AND GAMMA IS A FUNCTION OF U,X AND T
C
      IMPLICIT DOUBLE PRECISION (A-H,O-Z)
      PARAMETER (NFRAC=10)
      DOUBLE PRECISION DEL(NFRAC),ETA(NFRAC),GAM(NFRAC),FRAC(NFRAC)
      INTEGER NPDE, NV, IRES
      LOGICAL LEFT
      COMMON /DVAR/ ALPHA0
      COMMON /DVAR2/ALPHA,DEL,ETA,GAM,FRAC,NFRACC
      DOUBLE PRECISION BETA(NPDE), GAMMA(NPDE), U(NPDE), UX(NPDE),
     1                 T, V(1), VDOT(1), UDOT(NPDE), UTDX(NPDE),
     2                 alpha
      save
      IF(LEFT)THEN
        beta(1) = 1d0
        gamma(1) = 0d0
        DO 10, I=2,NFRACC+1
          beta(I) = 0d0
 10       gamma(I) = ux(I)
      ELSE
        beta(1) = 0d0
        gamma(1) = U(1)
        DO 20, I=2,NFRACC+1
          beta(I) = 0d0
 20       gamma(I) = u(I)
      END IF
      RETURN
      END
      subroutine sodefn
      return
      end
C
      SUBROUTINE DDASSL (RES,NEQ,T,Y,YPRIME,TOUT,
     *  INFO,RTOL,ATOL,IDID,
     *  RWORK,LRW,IWORK,LIW,RPAR,IPAR,
     *  JAC)
```

```
C  Multi-Fraction Model With an Applied Field
C
C  PROGRAM TO CALCULATE PENETRATION BASED ON NUMBER
C  AND VOLUME DENSITY USING A LAMINAR FLOW PROFILE
C  MAXIMUM NUMBER OF FRACTIONS = 10
      PARAMETER ( max = 11, jmax=51)
      INTEGER I, J, idev, nfrac
      double precision eo, e, PI
      double precision Pdia(max), frac(max), q(max),
     1        a(max), zbar(jmax), expres,
     2        PentN(max,jmax), PentV(max,jmax),
     3        PtotN(jmax), PtotV(jmax), tdepN(jmax),
     4        tdepV(jmax), beta(max),
     5        rid, rod, ri, mu, flow, uo, Vo, L,
     6        Eave, cfrac, vfrac, sum1,
     7        sum2, sum3, sumf, tfrac, denom1,
     8        denom2(jmax), Area, ve(max), eta(max), qdot
C*********************************************************************C
C     Permittivity of air (C2/N m2)
      parameter ( eo = 8.85d-12)
C     elementary charge (C/electronic charge)
      parameter ( e = 1.60d-19)
C*********************************************************************C
      CHARACTER*12 FILEN
      save
      PI = 4d0*ATAN(1d0)
      idev = 4
      PRINT*,'Enter filename to be read enclosed in tick marks'
      read*, FILEN
      open (5, file= FILEN, status='unknown')
      open (idev, file= 'tdepa.dat',status='unknown')
      read (5,*) rid, rod
      read (5,*) nfrac
      do 5, i=1, nfrac
5   read (5,*) Pdia(i), frac(i)
    read (5,*) cfrac
      read (5,*) mu
      read (5,*) uo
      read (5,*) Vo
      read (5,*) L
C*********************************************************************C
C     Check to be sure frac(i) sums to 1.0
C*********************************************************************C
      sumf = 0d0
      do 6, i=1, nfrac
6   sumf = sumf + frac(i)
      if (sumf .LE. 0.99d0 .or. sumf .GE. 1.01d0) then
      print*, 'Your fractions do not sum to 1.0!'
      print*
      print*
      goto 130
      endif
C*********************************************************************C
```

```
C      Calculation of gas flow rate in m3/min
C*********************************************************************C
          Flow = uo*60.0d0*PI*(rod**2-rid**2)
C*********************************************************************C
C     Calculation of average E field
C*********************************************************************C
      Eave = Vo/(rod-rid)
C*********************************************************************C
C     Calculation of particle charge q(i)
C     saturation charge multiplied by percent saturation
C     Field charging equation based on particle size > 1 micron
C*********************************************************************C
     do 10, i=1, nfrac
     q(i) = 3d0*PI*eo*Eave*Pdia(i)**2*cfrac
     a(i) = 0.5d0*Pdia(i)
 10   continue
C*********************************************************************C
          sum1 = 0d0
          sum2 = 0d0
          sum3 = 0d0
          tfrac = 0d0
          vfrac = 0d0
          ri = rid/rod
          expres = 0d0
          do 20, i=1, nfrac
 20     tfrac = tfrac + frac(i)
          denom1 = (1d0 - ri**2)*tfrac
          do 22, i=1, nfrac
          denom2(i) = frac(i)*a(i)**3
       vfrac = vfrac + denom2(i)
 22     continue
C*********************************************************************C
          write (idev,*) ' Tabulation of axial (z) particle penetration '
          write (idev,23) uo
 23       format('  Velocity Profile:  Laminar Flow   uo = ',d11.4,' m/s')
          write (idev,*)
          write (idev,25) cfrac*100d0
 25   format(2x,' % of saturation =        ',d11.4)
     write (idev,30) Vo
 30   format(2x, ' Applied voltage (Volts) = ',d11.4)
     write (idev,*)
C*********************************************************************C
     do 35, i=1, nfrac
     write (idev,38) i, Pdia(i)
 38   format(2x,' Particle size ',i2,' is       ',d11.3,' microns')
     write (idev,40) i, q(i)/e
 40   format(3x,'# charges for size ',i2,' =    ',d11.4)
     write (idev, 42) frac(i)*100d0
 42   format(2x, ' Percent of total fraction =', d11.4)
     write (idev,*)
 35   continue
C    write (idev,*) '  z (cm)     Pent1(V)     Pent2(V)     PtotV
C    1  PtotN'
     write (idev,*) '     z (cm)       pentN      pentV'
```

```
      write (idev,*)
C*********************************************************************C
C     Effective length is 40 cm.  Zbar(i) is in increments of 1 cm.
            do 50, j=1,41
            zbar(j) = (j-1d0)/40d0
            do 60, i=1, nfrac
            beta(i) = (q(i)*Vo*L)/(6d0*PI*mu*a(i)*log(rod/rid)*
     1          uo*rod**2)
            expres = 1d0 - 4d0*beta(i)*zbar(j)
            if (expres .lt. 0d0) then
            goto 65
            else
C*********************************************************************C
C       Calculation of penetration along the characteristic curve
C       Laminar Flow
C*********************************************************************C
C       Calculation based on number density
C*********************************************************************C
            PentN(i,j) = SQRT(1d0-4d0*beta(i)*zbar(j))*frac(i)
C*********************************************************************C
C       Calculation based on volume density
C*********************************************************************C
            PentV(i,j) = (a(i)**3*SQRT(1d0 - 4d0*
     1          beta(i)*zbar(j))*frac(i))/vfrac
            endif
 65     continue
      expres = 0d0
 60     continue
            do 70, i=1, nfrac
            beta(i) = 0d0
            sum1 = sum1 + PentN(i,j)
            sum2 = sum2 + PentV(i,j)
 70   continue
      PtotN(j) = sum1
      tdepN(j) = 1d0 - PtotN(j)
      PtotV(j) = sum2
      tdepV(j) = 1d0 - PtotV(j)
      write (idev,110) zbar(j)*40d0, PtotV(j), PtotN(j)
110   format(2x, d10.3,2x,d10.4,2x,d10.4)
C       write (idev,110) zbar(j)*40d0, PentV(1,j), PentV(2,j),
C     1PtotV(j), PtotN(j)
C110  format(2x,d10.3,2x,d10.4,2x,d10.4,2x,d10.4,2x,d10.4)
      sum1 = 0d0
      sum2 = 0d0
 50   continue
C*********************************************************************C
      write (idev,*)
      write (idev,120) flow
 120  format(' flow rate through reactor tube is: ',d11.4,' m3/min')
      write (idev,*)
      write (idev,125)
 125  format('  Penetration using Duetsch-Anderson Equation')
      write (idev,*)
 130    continue
```

```
      Area = 2d0*PI*rod*0.40d0
      qdot = uo*PI*(rod**2-rid**2)
      do 140, i=1, nfrac
      ve(i) = q(i)*Eave/(3d0*PI*mu*Pdia(i))
      eta(i) = DEXP(- Area*ve(i)/qdot)*frac(i)
      write (idev,150) i, eta(i)
150   format(2x,'  Penetration for particle',i2,'=',d11.4)
      sum3 = sum3 + eta(i)
140   continue
      write (idev,160) sum3
160   format(2x,'  Total penetration = ',d11.4)
            stop
            end
```

APPENDIX G

OUTPUT FILES FOR COMPUTER SIMULATION CODES FOR NO APPLIED VOLTAGE AND APPLIED VOLTAGE MODELS

Sample Output for the Mathematical Model Using a Two Particle Size Fraction with No Applied Field

MULTI-FRAC MODEL
****
POLY OF DEGREE = 2 NO OF ELEMENTS = 29

alpha = 0.6217D-02

AT X = 0.653D-08 DASSL RETURNED IDID = 3

At X Distance = 0.1000D+02 cm

r	V	rho1	rho2
0.000D+00	0.808D-02	0.900D+00	0.100D+00
0.202D-01	0.808D-02	0.900D+00	0.100D+00
0.404D-01	0.807D-02	0.900D+00	0.100D+00
0.606D-01	0.805D-02	0.900D+00	0.100D+00
0.808D-01	0.803D-02	0.900D+00	0.100D+00
0.101D+00	0.800D-02	0.900D+00	0.100D+00
0.121D+00	0.796D-02	0.900D+00	0.100D+00
0.141D+00	0.792D-02	0.900D+00	0.100D+00
0.162D+00	0.787D-02	0.900D+00	0.100D+00
0.182D+00	0.781D-02	0.900D+00	0.100D+00
0.202D+00	0.775D-02	0.900D+00	0.100D+00
0.222D+00	0.768D-02	0.900D+00	0.100D+00
0.243D+00	0.761D-02	0.900D+00	0.100D+00
0.263D+00	0.752D-02	0.900D+00	0.100D+00
0.283D+00	0.743D-02	0.900D+00	0.100D+00
0.303D+00	0.734D-02	0.900D+00	0.100D+00
0.323D+00	0.724D-02	0.900D+00	0.100D+00
0.344D+00	0.713D-02	0.900D+00	0.100D+00
0.364D+00	0.701D-02	0.900D+00	0.100D+00
0.384D+00	0.689D-02	0.900D+00	0.100D+00
0.404D+00	0.676D-02	0.900D+00	0.100D+00
0.424D+00	0.663D-02	0.900D+00	0.100D+00
0.445D+00	0.648D-02	0.900D+00	0.100D+00
0.465D+00	0.634D-02	0.900D+00	0.100D+00
0.485D+00	0.618D-02	0.900D+00	0.100D+00
0.505D+00	0.602D-02	0.900D+00	0.100D+00
0.525D+00	0.585D-02	0.900D+00	0.100D+00
0.546D+00	0.568D-02	0.900D+00	0.100D+00
0.566D+00	0.549D-02	0.900D+00	0.100D+00
0.586D+00	0.531D-02	0.900D+00	0.100D+00
0.606D+00	0.511D-02	0.900D+00	0.100D+00
0.626D+00	0.491D-02	0.900D+00	0.100D+00
0.647D+00	0.470D-02	0.900D+00	0.100D+00
0.667D+00	0.449D-02	0.900D+00	0.100D+00
0.687D+00	0.427D-02	0.900D+00	0.100D+00
0.707D+00	0.404D-02	0.900D+00	0.100D+00
0.728D+00	0.380D-02	0.900D+00	0.100D+00
0.748D+00	0.356D-02	0.900D+00	0.100D+00
0.768D+00	0.332D-02	0.900D+00	0.100D+00

0.788D+00	0.306D-02	0.900D+00	0.100D+00
0.808D+00	0.280D-02	0.900D+00	0.100D+00
0.829D+00	0.253D-02	0.900D+00	0.100D+00
0.849D+00	0.226D-02	0.900D+00	0.100D+00
0.869D+00	0.198D-02	0.900D+00	0.100D+00
0.889D+00	0.169D-02	0.900D+00	0.100D+00
0.935D+00	0.102D-02	0.900D+00	0.100D+00
0.980D+00	0.320D-03	0.900D+00	0.100D+00
0.982D+00	0.280D-03	0.900D+00	0.100D+00
0.985D+00	0.241D-03	0.900D+00	0.100D+00
0.988D+00	0.201D-03	0.900D+00	0.100D+00
0.990D+00	0.161D-03	0.900D+00	0.100D+00
0.992D+00	0.129D-03	0.900D+00	0.100D+00
0.994D+00	0.966D-04	0.900D+00	0.100D+00
0.995D+00	0.806D-04	0.899D+00	0.100D+00
0.996D+00	0.645D-04	0.882D+00	0.100D+00
0.997D+00	0.403D-04	0.728D+00	0.913D-01
0.999D+00	0.161D-04	0.319D+00	0.428D-01
0.999D+00	0.806D-05	0.160D+00	0.217D-01
0.100D+01	0.000D+00	0.000D+00	0.000D+00

penetration 0.8972194937399108 deposition 0.1027805062600892

AT X = 0.131D-07 DASSL RETURNED IDID = 3

At X Distance = 0.2000D+02 cm

r	V	rho1	rho2
0.000D+00	0.808D-02	0.900D+00	0.100D+00
0.202D-01	0.808D-02	0.900D+00	0.100D+00
0.404D-01	0.807D-02	0.900D+00	0.100D+00
0.606D-01	0.805D-02	0.900D+00	0.100D+00
0.808D-01	0.803D-02	0.900D+00	0.100D+00
0.101D+00	0.800D-02	0.900D+00	0.100D+00
0.121D+00	0.796D-02	0.900D+00	0.100D+00
0.141D+00	0.792D-02	0.900D+00	0.100D+00
0.162D+00	0.787D-02	0.900D+00	0.100D+00
0.182D+00	0.781D-02	0.900D+00	0.100D+00
0.202D+00	0.775D-02	0.900D+00	0.100D+00
0.222D+00	0.768D-02	0.900D+00	0.100D+00
0.243D+00	0.761D-02	0.900D+00	0.100D+00
0.263D+00	0.752D-02	0.900D+00	0.100D+00
0.283D+00	0.743D-02	0.900D+00	0.100D+00
0.303D+00	0.734D-02	0.900D+00	0.100D+00
0.323D+00	0.724D-02	0.900D+00	0.100D+00
0.344D+00	0.713D-02	0.900D+00	0.100D+00
0.364D+00	0.701D-02	0.900D+00	0.100D+00
0.384D+00	0.689D-02	0.900D+00	0.100D+00
0.404D+00	0.676D-02	0.900D+00	0.100D+00
0.424D+00	0.663D-02	0.900D+00	0.100D+00
0.445D+00	0.648D-02	0.900D+00	0.100D+00
0.465D+00	0.634D-02	0.900D+00	0.100D+00
0.485D+00	0.618D-02	0.900D+00	0.100D+00
0.505D+00	0.602D-02	0.900D+00	0.100D+00

0.525D+00	0.585D-02	0.900D+00	0.100D+00
0.546D+00	0.568D-02	0.900D+00	0.100D+00
0.566D+00	0.549D-02	0.900D+00	0.100D+00
0.586D+00	0.531D-02	0.900D+00	0.100D+00
0.606D+00	0.511D-02	0.900D+00	0.100D+00
0.626D+00	0.491D-02	0.900D+00	0.100D+00
0.647D+00	0.470D-02	0.900D+00	0.100D+00
0.667D+00	0.449D-02	0.900D+00	0.100D+00
0.687D+00	0.427D-02	0.900D+00	0.100D+00
0.707D+00	0.404D-02	0.900D+00	0.100D+00
0.728D+00	0.380D-02	0.900D+00	0.100D+00
0.748D+00	0.356D-02	0.900D+00	0.100D+00
0.768D+00	0.332D-02	0.900D+00	0.100D+00
0.788D+00	0.306D-02	0.900D+00	0.100D+00
0.808D+00	0.280D-02	0.900D+00	0.100D+00
0.829D+00	0.253D-02	0.900D+00	0.100D+00
0.849D+00	0.226D-02	0.900D+00	0.100D+00
0.869D+00	0.198D-02	0.900D+00	0.100D+00
0.889D+00	0.169D-02	0.900D+00	0.100D+00
0.935D+00	0.102D-02	0.900D+00	0.100D+00
0.980D+00	0.320D-03	0.900D+00	0.100D+00
0.982D+00	0.280D-03	0.900D+00	0.100D+00
0.985D+00	0.241D-03	0.900D+00	0.100D+00
0.988D+00	0.201D-03	0.900D+00	0.100D+00
0.990D+00	0.161D-03	0.900D+00	0.100D+00
0.992D+00	0.129D-03	0.900D+00	0.100D+00
0.994D+00	0.966D-04	0.898D+00	0.100D+00
0.995D+00	0.805D-04	0.880D+00	0.999D-01
0.996D+00	0.644D-04	0.823D+00	0.984D-01
0.997D+00	0.403D-04	0.615D+00	0.820D-01
0.999D+00	0.161D-04	0.262D+00	0.361D-01
0.999D+00	0.805D-05	0.131D+00	0.182D-01
0.100D+01	0.000D+00	0.000D+00	0.000D+00

penetration 0.8965034492531583 deposition 0.1034965507468417

AT X = 0.196D-07 DASSL RETURNED IDID = 3

At X Distance = 0.3000D+02 cm

r	V	rho1	rho2
0.000D+00	0.808D-02	0.900D+00	0.100D+00
0.202D-01	0.808D-02	0.900D+00	0.100D+00
0.404D-01	0.807D-02	0.900D+00	0.100D+00
0.606D-01	0.805D-02	0.900D+00	0.100D+00
0.808D-01	0.803D-02	0.900D+00	0.100D+00
0.101D+00	0.800D-02	0.900D+00	0.100D+00
0.121D+00	0.796D-02	0.900D+00	0.100D+00
0.141D+00	0.792D-02	0.900D+00	0.100D+00
0.162D+00	0.787D-02	0.900D+00	0.100D+00
0.182D+00	0.781D-02	0.900D+00	0.100D+00
0.202D+00	0.775D-02	0.900D+00	0.100D+00
0.222D+00	0.768D-02	0.900D+00	0.100D+00
0.243D+00	0.761D-02	0.900D+00	0.100D+00

0.263D+00	0.752D-02	0.900D+00	0.100D+00
0.283D+00	0.743D-02	0.900D+00	0.100D+00
0.303D+00	0.734D-02	0.900D+00	0.100D+00
0.323D+00	0.724D-02	0.900D+00	0.100D+00
0.344D+00	0.713D-02	0.900D+00	0.100D+00
0.364D+00	0.701D-02	0.900D+00	0.100D+00
0.384D+00	0.689D-02	0.900D+00	0.100D+00
0.404D+00	0.676D-02	0.900D+00	0.100D+00
0.424D+00	0.663D-02	0.900D+00	0.100D+00
0.445D+00	0.648D-02	0.900D+00	0.100D+00
0.465D+00	0.634D-02	0.900D+00	0.100D+00
0.485D+00	0.618D-02	0.900D+00	0.100D+00
0.505D+00	0.602D-02	0.900D+00	0.100D+00
0.525D+00	0.585D-02	0.900D+00	0.100D+00
0.546D+00	0.568D-02	0.900D+00	0.100D+00
0.566D+00	0.549D-02	0.900D+00	0.100D+00
0.586D+00	0.531D-02	0.900D+00	0.100D+00
0.606D+00	0.511D-02	0.900D+00	0.100D+00
0.626D+00	0.491D-02	0.900D+00	0.100D+00
0.647D+00	0.470D-02	0.900D+00	0.100D+00
0.667D+00	0.449D-02	0.900D+00	0.100D+00
0.687D+00	0.427D-02	0.900D+00	0.100D+00
0.707D+00	0.404D-02	0.900D+00	0.100D+00
0.728D+00	0.380D-02	0.900D+00	0.100D+00
0.748D+00	0.356D-02	0.900D+00	0.100D+00
0.768D+00	0.332D-02	0.900D+00	0.100D+00
0.788D+00	0.306D-02	0.900D+00	0.100D+00
0.808D+00	0.280D-02	0.900D+00	0.100D+00
0.829D+00	0.253D-02	0.900D+00	0.100D+00
0.849D+00	0.226D-02	0.900D+00	0.100D+00
0.869D+00	0.198D-02	0.900D+00	0.100D+00
0.889D+00	0.169D-02	0.900D+00	0.100D+00
0.935D+00	0.102D-02	0.900D+00	0.100D+00
0.980D+00	0.320D-03	0.900D+00	0.100D+00
0.982D+00	0.280D-03	0.900D+00	0.100D+00
0.985D+00	0.241D-03	0.900D+00	0.100D+00
0.988D+00	0.201D-03	0.900D+00	0.100D+00
0.990D+00	0.161D-03	0.900D+00	0.100D+00
0.992D+00	0.129D-03	0.899D+00	0.100D+00
0.994D+00	0.966D-04	0.889D+00	0.100D+00
0.995D+00	0.805D-04	0.852D+00	0.992D-01
0.996D+00	0.644D-04	0.770D+00	0.954D-01
0.997D+00	0.403D-04	0.547D+00	0.750D-01
0.999D+00	0.161D-04	0.229D+00	0.324D-01
0.999D+00	0.805D-05	0.115D+00	0.163D-01
0.100D+01	0.000D+00	0.000D+00	0.000D+00

penetration 0.8959797974657935 deposition 0.1040202025342065

AT X = 0.261D-07 DASSL RETURNED IDID = 3

At X Distance = 0.4000D+02 cm

r	V	rho1	rho2
0.000D+00	0.808D-02	0.900D+00	0.100D+00
0.202D-01	0.808D-02	0.900D+00	0.100D+00
0.404D-01	0.807D-02	0.900D+00	0.100D+00
0.606D-01	0.805D-02	0.900D+00	0.100D+00
0.808D-01	0.803D-02	0.900D+00	0.100D+00
0.101D+00	0.800D-02	0.900D+00	0.100D+00
0.121D+00	0.796D-02	0.900D+00	0.100D+00
0.141D+00	0.792D-02	0.900D+00	0.100D+00
0.162D+00	0.787D-02	0.900D+00	0.100D+00
0.182D+00	0.781D-02	0.900D+00	0.100D+00
0.202D+00	0.775D-02	0.900D+00	0.100D+00
0.222D+00	0.768D-02	0.900D+00	0.100D+00
0.243D+00	0.761D-02	0.900D+00	0.100D+00
0.263D+00	0.752D-02	0.900D+00	0.100D+00
0.283D+00	0.743D-02	0.900D+00	0.100D+00
0.303D+00	0.734D-02	0.900D+00	0.100D+00
0.323D+00	0.724D-02	0.900D+00	0.100D+00
0.344D+00	0.713D-02	0.900D+00	0.100D+00
0.364D+00	0.701D-02	0.900D+00	0.100D+00
0.384D+00	0.689D-02	0.900D+00	0.100D+00
0.404D+00	0.676D-02	0.900D+00	0.100D+00
0.424D+00	0.663D-02	0.900D+00	0.100D+00
0.445D+00	0.648D-02	0.900D+00	0.100D+00
0.465D+00	0.634D-02	0.900D+00	0.100D+00
0.485D+00	0.618D-02	0.900D+00	0.100D+00
0.505D+00	0.602D-02	0.900D+00	0.100D+00
0.525D+00	0.585D-02	0.900D+00	0.100D+00
0.546D+00	0.568D-02	0.900D+00	0.100D+00
0.566D+00	0.549D-02	0.900D+00	0.100D+00
0.586D+00	0.531D-02	0.900D+00	0.100D+00
0.606D+00	0.511D-02	0.900D+00	0.100D+00
0.626D+00	0.491D-02	0.900D+00	0.100D+00
0.647D+00	0.470D-02	0.900D+00	0.100D+00
0.667D+00	0.449D-02	0.900D+00	0.100D+00
0.687D+00	0.427D-02	0.900D+00	0.100D+00
0.707D+00	0.404D-02	0.900D+00	0.100D+00
0.728D+00	0.380D-02	0.900D+00	0.100D+00
0.748D+00	0.356D-02	0.900D+00	0.100D+00
0.768D+00	0.332D-02	0.900D+00	0.100D+00
0.788D+00	0.306D-02	0.900D+00	0.100D+00
0.808D+00	0.280D-02	0.900D+00	0.100D+00
0.829D+00	0.253D-02	0.900D+00	0.100D+00
0.849D+00	0.226D-02	0.900D+00	0.100D+00
0.869D+00	0.198D-02	0.900D+00	0.100D+00
0.889D+00	0.169D-02	0.900D+00	0.100D+00
0.935D+00	0.102D-02	0.900D+00	0.100D+00
0.980D+00	0.320D-03	0.900D+00	0.100D+00
0.982D+00	0.280D-03	0.900D+00	0.100D+00
0.985D+00	0.241D-03	0.900D+00	0.100D+00
0.988D+00	0.201D-03	0.900D+00	0.100D+00
0.990D+00	0.161D-03	0.900D+00	0.100D+00
0.992D+00	0.129D-03	0.898D+00	0.100D+00
0.994D+00	0.966D-04	0.874D+00	0.999D-01

0.995D+00	0.805D-04	0.822D+00	0.981D-01
0.996D+00	0.644D-04	0.726D+00	0.923D-01
0.997D+00	0.403D-04	0.500D+00	0.697D-01
0.999D+00	0.161D-04	0.207D+00	0.297D-01
0.999D+00	0.805D-05	0.104D+00	0.149D-01
0.100D+01	0.000D+00	0.000D+00	0.000D+00

penetration 0.8955621366120301 deposition 0.1044378633879699

Sample Output File for the Mathematical Model Using a Two Particle Size Fraction with an Applied Voltage = 3000 kV

Tabulation of axial (z) particle penetration
Velocity Profile: Laminar Flow uo = 0.3600D+01 m/s

% of saturation = 0.3500D+02
Applied voltage (Volts) = 0.3000D+04

Particle size 1 is 0.300D-05 microns
charges for size 1 = 0.5622D+03
Percent of total fraction = 0.1000D+02

Particle size 2 is 0.140D-05 microns
charges for size 2 = 0.1224D+03
Percent of total fraction = 0.9000D+02

z (cm)	pentN	pentV
0.000D+00	0.5223D+00	0.4777D+00
0.100D+01	0.5186D+00	0.4761D+00
0.200D+01	0.5148D+00	0.4745D+00
0.300D+01	0.5110D+00	0.4729D+00
0.400D+01	0.5072D+00	0.4713D+00
0.500D+01	0.5033D+00	0.4697D+00
0.600D+01	0.4995D+00	0.4681D+00
0.700D+01	0.4956D+00	0.4665D+00
0.800D+01	0.4916D+00	0.4648D+00
0.900D+01	0.4876D+00	0.4632D+00
0.100D+02	0.4836D+00	0.4616D+00
0.110D+02	0.4796D+00	0.4599D+00
0.120D+02	0.4755D+00	0.4583D+00
0.130D+02	0.4714D+00	0.4566D+00
0.140D+02	0.4673D+00	0.4549D+00
0.150D+02	0.4631D+00	0.4533D+00
0.160D+02	0.4589D+00	0.4516D+00
0.170D+02	0.4547D+00	0.4499D+00
0.180D+02	0.4504D+00	0.4482D+00
0.190D+02	0.4460D+00	0.4465D+00
0.200D+02	0.4416D+00	0.4448D+00
0.210D+02	0.4372D+00	0.4431D+00
0.220D+02	0.4328D+00	0.4414D+00
0.230D+02	0.4282D+00	0.4397D+00
0.240D+02	0.4237D+00	0.4379D+00
0.250D+02	0.4191D+00	0.4362D+00

0.260D+02	0.4144D+00	0.4345D+00
0.270D+02	0.4097D+00	0.4327D+00
0.280D+02	0.4049D+00	0.4310D+00
0.290D+02	0.4001D+00	0.4292D+00
0.300D+02	0.3952D+00	0.4274D+00
0.310D+02	0.3903D+00	0.4256D+00
0.320D+02	0.3852D+00	0.4239D+00
0.330D+02	0.3802D+00	0.4221D+00
0.340D+02	0.3750D+00	0.4203D+00
0.350D+02	0.3698D+00	0.4185D+00
0.360D+02	0.3645D+00	0.4166D+00
0.370D+02	0.3591D+00	0.4148D+00
0.380D+02	0.3537D+00	0.4130D+00
0.390D+02	0.3481D+00	0.4111D+00
0.400D+02	0.3425D+00	0.4093D+00

flow rate through reactor tube is: 0.6117D-01 m3/min

Penetration using Duetsch-Anderson Equation

Penetration for particle 1=	0.4607D-01
Penetration for particle 2=	0.6269D+00
Total penetration =	0.6730D+00

REFERENCES

Arai, M., "Thermal Analysis for the Evaluation of SOF." *SAE Transactions*, Special Publication SP-943, Diesel Exhaust Aftertreatment, (1993): 93-99.

Ahlstroem, A., Odenbrand, C., "Combustion of Soot Deposits from Diesel Engines on Mixed Oxides of Vanadium Pentoxide and Cupric Oxide." *Applied Catalysis*, Vol. 60 No.1 (1990): 157-172.

Barris, M.A., "Durability Studies of Trap Oxidizer Systems." *SAE Transactions*, SAE 900108 (1990).

Beckmann, R., Engler, W., Mueller, E., "A New Generation of Diesel Oxidation Catalysts." *SAE Transactions*, SAE 922330 (1992).

Berzins, M. And Dew, P., "Algorithm 690 Chebyshev Polynomial Software for Elliptic-Parabolic Systems of PDEs." *ACM Transactions on Mathematical Software*, Vol. 17, No. 2 (1991): 17-206.

Boublik, T., Fried, V., and Hala, E., *The Vapour Pressures of Pure Substances*. Amsterdam: Elsevier Scientific Publishing Co., 1973.

Bohm, Jaroslav, *Electrostatic Precipitators*. Amsterdam: Elsevier Scientific Publishing Co., 1982.

Brenan, K., Campbell, S., and Petzold, L., *Numerical Solution of Initial Value Problems in Differential-Algebraic Equations*. North Holland, Amsterdam, 1989.

Brum, R., and Samuelsen, G., "Assessment of a Dilute Swirl Combustor as a Bench Scale, Complex Flow Test Bed for Modeling, Diagnostics, and Fuels Effects Studies." *AIAA/SAE/ASME 18th Joint Propulsion Conference*, Paper AIAA-82-1263 (1982).

Cericola, R., Ciambelli, P., Corbo, P., Gambino, M., Vaccaro, S., "Soot Removal from Automotive Diesel Exhausts by a Catalytic Aftertreatment Device." *Rivista Dei Combustibili*, Vol 46, No. 5 (1992): 149-157.

Ciambelli, P., Corbo, P., Parella, P., Scialo, M., Vaccaro, S., "Catalytic Oxidation of Soot from Diesel Exhaust Gases." *Thermochimica Acta*, Vol. 162, No.1 (1990): 83-89.

Ciambelli, P., Parella, P., Vaccaro, S., "Kinetics of Soot Oxidation on Potassium-Copper-Vanadium Catalyst." *Studies in Surface Science and Catal*ysis, Vol. 71 Catalytic Automotive Pollution Control 2 (1991): 323-335.

REFERENCES
(Continued)

Ciambelli, P., Palma, V., Vacarro, S., "Carbon-Oxygen Reaction on Copper/Vanadium/Potassium Catalyst for Soot Oxidation." *Studies in Surface Science and Catal*ysis, Vol. 75 New Frontiers in Catalysis, Part C, (1993): 2660-2672.

Ciambelli, P., Corbo, P., Gambino, M., Palma, V., Vaccaro, S., "Catalytic Combustion of Carbon Particulate." *Catalysis Today*, Vol. 27 (1-2), (1996): 99-106.

Chen, R.Y., "Deposition of Charged Particles in Tubes." *Journal of Aerosol Science*, Vol. 9 (1978): 449-453.

Dettling, J., and Skomoroski, R., "Catalyzed Diesel Exhaust Particulate Filter." US Patent Appl. EP 85-302799 850422, *Chem. Abstr.*, 1985, 104:23648.

Farzaneh, M., Allaire, M., Marceau, K., and Lachance, P., "Electrostatic Capture and Agglomeration of Particles Emitted by Diesel Engines." *Conference Record: Proceedings of the 29th IAS Annual Meeting*, Part 2, Oct. 2-5, 1994, (1994): 1534-1537.

Heck, R., and Farrauto, R., *Catalytic Air Pollution Control*. New York: Van Nostrand Reinhold, 1995.

Hinds, W.C., *Aerosol Technology, Properties, Behavior, and Measurement of Airborne Particles*. New York: John Wiley and Sons, 1982.

Holstein, W., "Performance of Gas Saturators in the Presence of Exit Stream Temperatures Gradients and Implications for Chemical Vapor Deposition Saturator Design." *Chemical Engineering Science*, Vol. 49, No. 13 (1994): 2097-2105.

Horiuchi, M., Saito, K., Ichihara, S., "The Effects of Flow-Through Type Oxidation Catalysts on the Particulate Reduction of 1990's Diesel Engines." *SAE Transactions*, SAE 900600 SP-816 (1990).

Horiuchi, M., Saito, K., (Nippon Shokubai Kagaku Kogyo Co., Ltd., Japan), "Catalyst for Treatment of Diesel Exhaust Gases", US Patent Appl. EP 91-301547 910226, *Chem. Abstr.*, 1991, 116:27099.

REFERENCES
(Continued)

Kennedy, A., Dempsy, R., Lyons, P., "Studies of the Catalytic Combustion of Particulate Carbon on Ceramic Support Oxidation Catalysts." *Materials Science Monographs*, Vol.66D Ceramics Today - Tomorrow's Ceramic, Part D, (1991): 2525-2529.

Khalil, N., and Levendis, Y.A., "Development of a New Diesel Particulate Control System with Wall-Flow Filters and Reverse Cleaning Regeneration." *SAE Transactions*, SAE 920567 (1992).

Kittelson, D.B., and Pui, Y.H., "Electrostatic Collection of Diesel Particles." *SAE Transactions*, SAE 86009 (1986).

Kittelson, D.B, Reinertsen, J., and Michalski, J., "Further Studies of Electrostatic Collection and Agglomeration of Diesel Particles." *SAE Transactions*, SAE 910329 (1991).

Kraemer, G., and Pfefferle, L.D., "Fuel-Rich Catalytically Stabilized Combustion of Hexane." *Chemical Physical Processes for Combustion*, (1990): 73/1-73/4.

Lawton, J., and Weinberg, F., *Electrical Aspects of Combustion*. Oxford: Clarendon Press, 1969.

Lin, C.H., Chao, B.T., and Soo, S.L., "Corona Charging of Diesel Smoke." *Journal of Aerosol Science Proceedings*, Vienna, Austria, Sep 18-23, 1989, Vol. 20, No. 8 (1989): 1389-1392.

Love, A., Middleman, S., and Hochberg, A., "The Dynamics of Bubblers as Vapor Delivery Systems." *Journal of Crystal Growth*, Vol. 129 (1993): 119-133.

Masuda, S., and Moon, J., "Electrostatic Precipitation of Carbon Soot from Diesel Engine Exhaust." *IEEE Transactions on Industry Applications*, Vol. 1A-19, No. 6 (1983): 1104-1111.

National Institute of Occupational Safety and Health (NIOSH), *Current Intelligence Bulletin 50*, Carcinogenic Effects of Exposure to Diesel Exhaust (1988).

Oh, Se H., Mitchell, P.J., and Siewert, R.M., "Methane Oxidation Over Alumina-Supported Noble-Metal Catalysts With and Without Cerium Additives." *Journal of Catalysts*, Vol. 132 (1991): 287-301.

Shinozaki, O., Shinoyama, E., and Saito, K., "Trapping Performance of Diesel Particulate Filters." *SAE Transactions*, SAE 900107 (1990).

REFERENCES
(Continued)

Smith J., and Van Ness, H., *Introduction to Chemical Engineering Thermodynamics*. New York: McGraw-Hill, 4th ed., 1987.

Thimsen, D.P, Kirb, J.B., Kotz, T.J., and Kittelson, D.B., "The Performance of an Electrostatic Agglomerator as a Diesel Soot Emission Control Device." *SAE Transactions*, SAE 900330 (1990).

Voss, K., Rice, G., Yavuz, B., Hirt, C., and Farrauto, R.J., " Performance Characteristics of a Novel Diesel Oxidation Catalyst." *SAE Transactions*, SAE 940239 (1994).

White, H.J., "Particle Charging in Electrostatic Precipitation." *Transactions American Institute of Electrical Engineers*, Vol. 70 (1951): 1186-1191.

Wyatt, M., Manning, W., Roth, S., D'Aniello, M., Andersonn, E., Fredholm, S. "The Design of Flow-Through Diesel Oxidation Catalysts." *SAE Transactions*, SAE 930130 (1993).

Yoshimoto, M., Nakatsuji, T., Nagano, K., Yoshida, K., "Particle-Removing Catalytic Filter and its Use in Removing Soot from Diesel Exhaust." European Patent Appl. EP 369163 A1 900523, *Chem. Abstr.* 1989, 113:102641.

Zelenka, P., Ostgathe, K., Lox, E., "Reduction of Diesel Engine Emissions by Using Oxidation Catalysts." *SAE Transactions*, SAE 902111 SP-839 (1990).